THE DYNAMICS OF CENOZOIC AND MESOZOIC PLATE MOTIONS

Carolina Lithgow-Bertelloni[1]
Department of Terrestrial Magnetism
Carnegie Institution of Washington
Washington, D. C.

Mark A. Richards
Department of Geology and Geophysics
University of California, Berkeley

Abstract. Our understanding of the dynamics of plate motions is based almost entirely upon modeling of present-day plate motions. A fuller understanding, however, can be derived from consideration of the history of plate motions. Here we investigate the kinematics of the last 120 Myr of plate motions and the dynamics of Cenozoic motions, paying special attention to changes in the character of plate motions and plate-driving forces. We analyze the partitioning of the observed surface velocity field into toroidal (transform/spin) and poloidal (spreading/subduction) motions. The present-day field is not equipartitioned in poloidal and toroidal components; toroidal motions account for only one third of the total. The toroidal/poloidal ratio has changed substantially in the last 120 Myr with poloidal motion decreasing significantly after 43 Ma while toroidal motion remains essentially constant; this result is not explained by changes in plate geometry alone. We develop a self-consistent model of plate motions by (1) constructing a straightforward model of mantle density heterogeneity based largely upon subduction history and then (2) calculating the induced plate motions for each stage of the Cenozoic. The "slab" heterogeneity model compares rather well with seismic heterogeneity models, especially away from the thermochemical boundary layers near the surface and core-mantle boundary. The slab model predicts the observed geoid extremely well, although comparison between predicted and observed dynamic topography is ambiguous. The midmantle heterogeneities that explain much of the observed seismic heterogeneity and geoid are derived largely from late Mesozoic and early Cenozoic subduction, when subduction rates were much higher than they are at present. The plate motion model itself successfully predicts Cenozoic plate motions (global correlations of 0.7–0.9) for mantle viscosity structures that are consistent with a variety of geophysical studies. We conclude that the main plate-driving forces come from subducted slabs (>90%), with forces due to lithospheric effects (e.g., oceanic plate thickening) providing a very minor component (<10%). For whole mantle convection, most of the slab buoyancy forces are derived from lower mantle slabs. Unfortunately, we cannot reproduce the toroidal/poloidal partitioning ratios observed for the Cenozoic, nor do our models explain apparently sudden plate motion changes that define stage boundaries. The most conspicuous failure is our inability to reproduce the westward jerk of the Pacific plate at 43 Ma implied by the great bend in the Hawaiian-Emperor seamount chain. Our model permits an interesting test of the hypothesis that the collision of India with Asia may have caused the Hawaiian-Emperor bend. However, we find that this collision has no effect on the motion of the Pacific plate, implying that important plate boundary effects are missing in our models. Future progress in understanding global plate motions requires (1) more complete plate reconstruction information, including, especially, uncertainty estimates for past plate boundaries, (2) better treatment of plate boundary fault mechanics in plate motion models, (3) application of numerical convection models, constrained by global plate motion histories, to replace ad hoc mantle heterogeneity models, (4) better calibration of these heterogeneity models with seismic heterogeneity constraints, and (5) more comprehensive comparison of global plate/mantle dynamics models with geologic data, especially indicators of intraplate stress and strain, and constraints on dynamic topography derived from the stratigraphic record of sea level change.

1. INTRODUCTION

Since the development of the theory of plate tectonics the principal problem of geodynamics has been to explain global plate motions. In a superficial way, the solution to this problem was apparent from the very nature of plate tectonics itself: plates are "pulled" toward subduction zones by cold, dense lithosphere as it sinks into the warmer mantle, and plates are "pushed" by thickening of the oceanic lithosphere as it moves away from ridges. In a classic paper, *Turcotte and Oxburgh* [1967] showed, using simple boundary layer analysis, that buoyancy forces arising from subducted lithosphere were sufficient to explain global plate motions, given a

---

[1] Now at Department of Geological Sciences, University of Michigan, Ann Arbor.

Reviews of Geophysics, 36, 1 / *February 1998*
pages 27–78
Paper number 97RG02282

8755-1209/98/97RG-02282*$15.00*

mantle viscosity consistent with postglacial rebound [*Haskell*, 1935]. These results were expanded and largely confirmed by subsequent analyses of the forces acting on plates at present [e.g., *Forsyth and Uyeda*, 1975; *Chapple and Tullis*, 1977; *Gordon et al.*, 1978; *Richardson et al.*, 1979] and throughout the Cenozoic [*Jurdy and Stefanick*, 1988, 1991], in which "slab pull," "ridge push," "trench resistance," etc., were treated empirically as parameterized line forces acting along plate boundaries and in which viscous tractions were distributed ad hoc along the bases of plates.

Since these early studies, our understanding of the forces that drive and resist plate motions has not advanced fundamentally. Despite an ever increasing knowledge of the history of past plate motions and the ever increasing sophistication and power of model simulations of mantle convection, geodynamicists cannot give quantitative answers to most questions of interest to geologists: What resisting forces act along plate boundary faults? Are plate boundary forces comparable in magnitude to the buoyancy forces driving plate motions, or are plate motions primarily resisted by viscous drag? Why do plate motions change suddenly? To what extent are plates "self-driven" by thermal thickening and subduction of oceanic plates, as opposed to other modes of mantle convection such as deep mantle plumes arising from interior boundary layers [*Morgan*, 1981], or a secondary, sub-plate-scale mode of convection "beneath" the plates [*McKenzie et al.*, 1980]? What is the state of stress in plates arising from mantle convection and plate tectonics? What is the amplitude and history of dynamic surface topography associated with the mantle buoyancy forces that drive plate motions? Does continental lithosphere respond differently to plate driving forces, for example, through the presence of deep "tectospheric" roots [*Jordan*, 1975; *Alvarez*, 1982]?

Our inability to answer these questions, and many other such questions, can only be described as a disappointment after almost 3 decades of work following the plate tectonics revolution. What then are the main reasons for this lack of progress, and what avenues exist to advance our understanding of the dynamics of plate motions? Progress in modeling has been held up by (1) a lack of raw computational power to execute complicated global models of mantle convection coupled to plate motions and (2) our lack of knowledge of important physical properties of rocks under both lithospheric and deep mantle conditions. Recent dramatic increases in computing power [e.g., *Baumgardner*, 1985; *Bercovici et al.*, 1992; *Tackley et al.*, 1993; *Bunge et al.*, 1996] and development of efficient algorithms to model plates [*Gable et al.*, 1991; *Bercovici*, 1993; *Zhong and Gurnis*, 1995] promise to largely eliminate computational limitations on geodynamic modeling of the mantle-lithosphere system in the near future [*Bunge and Baumgardner*, 1995].

By contrast, there is little prospect that experimental or theoretical mineral physics will soon allow a priori specification of rock properties of the Earth's deep interior, especially viscosity or creep strength (see *Karato and Wu* [1993] for a current summary of upper mantle rheological studies). For example, the primary constraint on mantle viscosity remains observations of Fennoscandian and Laurentide postglacial rebound [*Haskell*, 1935; *Nakada and Lambeck*, 1989; *Mitrovica and Peltier*, 1995], and although some controversy remains concerning the gross radial viscosity structure of the mantle [e.g., *Nakada and Lambeck*, 1989; *Tushingham and Peltier*, 1992], all lines of evidence seem to point toward a highly viscous lower mantle [*Mitrovica and Forte*, 1997]. In fact, *Mitrovica* [1996] has shown that the disagreements within the community may be traced to a misinterpretation of the *Haskell* [1935] constraint and that rebound data are indeed consistent with a highly viscous lower mantle. Other properties, such as the viscous or brittle strength of subducted slabs, remain even farther out of reach, and there is still fundamental debate regarding the possibility of mantle compositional stratification [*Jeanloz and Knittle*, 1985; *Bina and Silver*, 1990; *Bukowinski and Wolf*, 1990; *Stixrude et al.*, 1992]. Similarly, the strength profile of the lithosphere and crust along plate boundaries is very poorly understood, as is its dependence upon timescale (e.g., seismic or plate tectonic). It is therefore necessary to couple geodynamic models of mantle convection and plate tectonics directly to observations in order to constrain the system's physical properties and in order to understand its dynamic behavior.

The history of plate motions, as mapped by plate tectonicists, is the primary constraint that must be applied to mantle convection models. If the power of this constraint is not fully obvious, it should be considered that the plates cover approximately four fifths of the surface of the mantle, the other one fifth being the core-mantle boundary (CMB). Thermal convection is driven by buoyancy forces developed at boundary layers, and the cooling of oceanic plates accounts for approximately 80% of the convective heat transfer from the deep mantle [*O'Connell and Hager*, 1980]. Only about 10% of the mantle heat flux can be attributed to mantle plumes (hotspots) [*Davies*, 1988; *Sleep*, 1990], and there is no clear evidence for other highly significant modes of mantle convection. Thus mapping plate motions is arguably equivalent to mapping the main thermal flux of the mantle. It is our firm conviction that our present level of understanding of mantle convection and plate tectonics can be fundamentally advanced by modeling observed plate motions during recent Earth history.

Strangely, the explicit incorporation of observed global plate motions in published mantle convection models has been minimal and has been restricted mainly to the present-day snapshot of plate motions. A fundamentally important advance was made by *Hager and O'Connell* [1981], who developed a straightforward analytical method for modeling instantaneous three-dimensional (3-D) mantle flow and surface plate motions induced by mantle density contrasts. As in previous studies, these authors concluded that present-day plate motions were driven mainly by subducted slabs and to a lesser extent by oceanic plate thickening. They also found that significant resistance (up to 200 bars shear stress) to plate motions may exist along subduction zone thrust faults. Hager and O'Connell based their mantle density model on present-day oceanic plate ages and locations of deep earthquakes (slabs), and they did not extend their model to past plate motions. *Ricard and Vigny* [1991] used an equivalent method to model plate motions induced by buoyancy forces inferred from seismic tomography and upper mantle slabs, achieving a fairly good match to present-day plate motions. Recently, this method has been extended to past plate motions by using subduction zone reconstructions to infer mantle density heterogeneity [*Lithgow-Bertelloni and Richards*, 1995; *Deparis et al.*, 1995]. These models explain Cenozoic and Mesozoic plate motions fairly well, and they are also remarkably successful in modeling the present-day mantle density heterogeneity structure inferred from studies of seismic tomography and the geoid [*Richards and Engebretson*, 1992; *Ricard et al.*, 1993] as well as dynamic topography and continental flooding [*Gurnis*, 1993].

In this paper we present a geodynamic analysis of global plate motions during the past 120 million years of Earth history. Although parts of this work have been published in previous, shorter papers [*Richards and Engebretson*, 1992; *Lithgow-Bertelloni et al.*, 1993; *Ricard et al.*, 1993; *Lithgow-Bertelloni and Richards*, 1995; *Richards and Lithgow-Bertelloni*, 1996], we desire to present a comprehensive view of the problems and promise of analyzing and modeling the history of plate tectonics. This view involves not only the details of modeling trade-offs and limitations, but also the complete set of observational constraints (plate motions, boundaries, and ages) we have used. The latter is particularly important because plate motion reconstructions are, in fact, models themselves, often highly controversial and subject to errors that are difficult to evaluate. In fact, the main problems we have encountered in our work have been in "translating" data and observations from the plate tectonics literature into a form useful for quantitative analysis: these problems often far outweighed the difficulties of dynamic modeling!

In this paper we present a rather complete accounting of a particular approach to these problems, rather than a comprehensive review of previous work on the subject. We begin with a general discussion of our physical modeling approach, along with its limitations. We then describe in detail the plate tectonic observations we have used, along with a kinematic analysis of these plate motions in terms of their poloidal and toroidal signatures, and an attempt at error analysis. Next we develop mantle heterogeneity models based mainly on the history of subduction, and we compare these models to present-day observations of mantle heterogeneity. We then use our mantle heterogeneity models to explore the dynamics of Cenozoic plate motions. Finally, we address some failures of our approach in order to indicate where significant progress can be made in modeling the history of plate motions and mantle convection.

2. MODELING APPROACH

2.1. Previous Approaches

Much of what we know about the dynamics of plate motions derives from early work in the 1970s which concluded that plates are driven mainly by a combination of the pull of the slabs on subducting plates and the push from the ridges, opposed by basal drag and collisional resistance at plate boundaries. This conclusion was reached by several independent studies, all using similar approaches. Most of these studies were based on either a process of trial and error or an inversion of plate velocities and the intraplate stress field to estimate the relative magnitude of driving and resisting torques, where in most cases the ridge push and slab pull forces were applied as line forces at the plate boundaries [*Solomon et al.*, 1975; *Forsyth and Uyeda*, 1975; *Chapple and Tullis*, 1977; *Gordon et al.*, 1978; *Richardson et al.*, 1979; *Richardson*, 1992]. However, the so-called ridge push force is not a line force acting at the ridge itself but instead is a buoyancy force distributed over the entire area of oceanic plates and the direct result of the thermal thickening of dense oceanic lithosphere [*Lister*, 1975; *Hager and O'Connell*, 1981]. Similarly, slab pull is also a buoyancy force due to the dense, downgoing slab, which is coupled to the lithosphere by some combination of elastic and viscous forces in the slab and surrounding mantle. The elastic part has been modeled as a pull on the surface plate, assuming that the slab acts as an efficient stress guide. The other component of slab pull is transmitted to plates via viscous coupling with the underlying mantle in response to sinking of the negatively buoyant slabs (Figure 1a).

In this study we model viscous coupling between plates and mantle flow induced by internal density contrasts, following the method pioneered by *Hager and O'Connell* [1981]. Our starting point is a physical model of plate-driving forces, with plates driven by a continuously evolving model of density heterogeneity in the Earth's mantle and lithosphere derived primarily from the large horizontal density contrasts that arise from the cooling of the oceanic lithosphere and its subsequent subduction.

2.2. Plate-Driving Forces

Near the surface, plate-driving forces include the thermal thickening of the oceanic lithosphere (ridge push) and possibly the hydrodynamic effect of the density difference between continents and oceans. In the deep mantle it is likely that subducted slabs (slab pull) contribute the largest buoyancy forces [e.g., *Richards and Engebretson*, 1992]. This statement is supported by the success of modeling the density distribution in the deep mantle and its dynamical consequences using the history of subduction [*Ricard et al.*, 1993; *Gurnis*, 1993; *Deparis et al.*, 1995; *Lithgow-Bertelloni and Richards*, 1995; *Richards and Lithgow-Bertelloni*, 1996].

In our model, the density heterogeneities near the surface and in the deep mantle induce mantle flow and viscous tractions that act on the plates. These density heterogeneities can be combined into a model for the density distribution inside the Earth's mantle. The resisting forces in our model arise from viscous dissipation, and we ignore local interplate forces such as collisional resistance at plate boundaries, except for one special case described later. The resisting forces act at the base of all plates. We also ignore the elastic forces. Provided with the appropriate plate reconstructions as piecewise-continuous velocity boundary conditions, we can solve self-consistently for the instantaneous 3-D flow and viscous stresses induced by internal density contrasts using the analytical torque balance method of *Hager and O'Connell* [1981], as described in the next section.

2.3. Analytical Methods

For a prescribed internal density field, ignoring self-gravitation, the flow in an incompressible Newtonian fluid is governed by the equations for conservation of mass (continuity equation)

$$\nabla \cdot \mathbf{v} = 0 \tag{1}$$

and momentum,

$$0 = \nabla \cdot \boldsymbol{\tau} + \mathbf{f} \tag{2}$$

together with the constitutive relation for Newtonian creep,

$$\boldsymbol{\tau} = -p\mathbf{I} + 2\eta\dot{\boldsymbol{\varepsilon}} \tag{3}$$

where $\mathbf{v}$ is the velocity, p is the non-hydrostatic pressure, $\mathbf{I}$ the identity matrix, η the viscosity, and $\dot{\boldsymbol{\varepsilon}}$ the strain rate tensor. The body forces $\mathbf{f} = \delta\rho\mathbf{g}$, where $\delta\rho$ is the lateral density contrast and $\mathbf{g}$ is the gravitational acceleration, are balanced by viscous stress gradients, $\boldsymbol{\tau}$ being the stress tensor. For our model, in which we do not take into account the effects of phase transitions in the mantle, the incompressibility assumption (1) is not severe. The effect of the compressibility of the fluid mantle on plate motions can be shown to be of the order 10% or less [*Ricard et al.*, 1984]. The surface plates, on the other hand, are treated as rigid, infinitely thin shells, as we discuss later.

We obtain the Navier-Stokes equation by substituting the constitutive relation (3) into the conservation of momentum equation (2). Neglecting all terms containing the gradient of the viscosity we have

$$\nabla p - 2\eta\nabla \cdot \dot{\boldsymbol{\varepsilon}} = \mathbf{f}. \tag{4a}$$

Making use of the incompressibility condition, the Navier-Stokes equation is further simplified as:

$$\nabla p - \eta\nabla^2\mathbf{v} = \mathbf{f}. \tag{4b}$$

The incompressibility condition (1) allows us to represent the velocity field $\mathbf{v}$ as the curl of a vector field $\mathbf{A}$, $\mathbf{v} = \nabla \times \mathbf{A}$. The velocity field $\mathbf{v}$ then is purely solenoidal (its divergence is zero) and the vector potential $\mathbf{A}$ can be further decomposed such that the velocity is expressed as the sum of toroidal and poloidal vector fields [*Chandrasekhar*, 1961]

$$\mathbf{T} = \nabla \times \left(\frac{\Psi}{r}\mathbf{r}\right) \tag{5a}$$

and

$$\mathbf{S} = \nabla \times \left[\nabla \times \left(\frac{\Phi}{r}\mathbf{r}\right)\right] \tag{5b}$$

respectively, where both $\mathbf{T}$ and $\mathbf{S}$ are solenoidal with defining scalar potentials Ψ and Φ. The poloidal velocities are associated with the upwellings and downwellings at ridges and subduction zones, and the toroidal velocities are associated with the shear motion at transform faults and plate spin.

In the absence of lateral viscosity variations or plates, the toroidal field is zero. To illustrate this, we separate toroidal and poloidal solutions by substituting for the velocity vector in (4b) by the sum of its toroidal (equation (5a)) and poloidal (equation (5b)) components. Taking the curl of the Navier-Stokes equation (4b) and projecting it onto the radial unit vector, $\hat{\mathbf{r}}$, we can separate the toroidal part of the velocity field. Remembering that $(\nabla \times \mathbf{S}) \cdot \hat{\mathbf{r}} = 0$, we obtain

$$\nabla^2(-\nabla_H^2\Psi) = 0 \tag{6a}$$

where ∇_H^2 is the horizontal component of the Laplacian. To separate the poloidal part, we project the Navier-Stokes equation (4c) onto the radial unit vector, $\hat{\mathbf{r}}$, yielding

$$\nabla^2\nabla_H^2\Phi = \frac{\delta\rho g}{\eta} \tag{6b}$$

The quantity $\zeta = -\nabla_H^2\Psi$ in (6a) is the radial vorticity of the flow ($\zeta = (\nabla \times \mathbf{v}) \cdot \hat{\mathbf{r}}$). No-slip boundary conditions require $\zeta = 0$ at the Earth's surface, while free slip requires $\partial\zeta/\partial r = 0$ on the surface [see, e.g., *Chandrasekhar*, 1961]. Because Laplace's equation does not permit a nonzero solution that vanishes, or whose normal derivative vanishes, on a closed boundary, equation (6a) rewritten in terms of the radial vorticity,

$$\nabla^2\zeta = 0 \tag{6c}$$

implies that the radial vorticity ζ must identically vanish everywhere for both no-slip and free slip surface boundary conditions.

Equations (6) show that in the absence of lateral viscosity variations the only motion excited is poloidal in nature [see also *Chandrasekhar*, 1961; *Kaula*, 1980; *Ricard and Vigny*, 1989]. This solution is in gross violation of the observations, which show that although the toroidal and poloidal fields are not equally partitioned, transform motions make up a substantial amount (30%) of the plate velocity power spectrum [*Lithgow-Bertelloni et al.*, 1993].

As was shown by *Kaula* [1980] and *Ricard and Vigny* [1989], allowing for lateral variations in viscosity generates a term involving the cross product of the viscosity and the pressure gradients, which gives rise to a nonzero toroidal field. (For a more extensive discussion see *Chandrasekhar* [1961], *Kaula* [1980], *Ricard and Vigny* [1989], and *Forte and Peltier* [1994].) On the Earth the largest effective lateral variations in viscosity occur at plate boundaries. In our solutions to equations (1)–(3) we excite toroidal power by imposing piecewise-rigid tectonic plates on the surface [*Hager and O'Connell*, 1979; *Ricard and Vigny*, 1989], so that plate boundaries have essentially no strength.

We represent the velocity and stresses with a spherical harmonic expansion, which allows us to separate the vertical and horizontal components of the flow [*Takeuchi and Hasegawa*, 1965; *Kaula*, 1975; *Hager and O'Connell*, 1979]. In spherical coordinates the radial (v_r), southerly (v_θ), and easterly (v_φ) components of the velocity can be written as

$$v_r = a_l^m(r) Y_l^m \tag{7a}$$

$$v_\theta = b_l^m(r) Y_{l,\theta}^m + c_l^m(r) Y_{l,\varphi}^m \tag{7b}$$

$$v_\varphi = b_l^m(r) Y_{l,\varphi}^m - c_l^m(r) Y_{l,\theta}^m \tag{7c}$$

where

$$Y_{l,\varphi}^m = \frac{1}{\sin\theta}\frac{\partial Y_l^m}{\partial\varphi} \qquad Y_{l,\theta}^m = \frac{\partial Y_l^m}{\partial\theta}$$

are the azimuthal and colatitudinal derivatives of the spherical harmonic function defined as

$$Y_l^m(\theta, \varphi) = P_l^m\left[\begin{smallmatrix}\cos(m\varphi)\\ \sin(m\varphi)\end{smallmatrix}\right]$$

where the P_l^m are the associated Legendre polynomials. Sums over repeated indices are implied so that, for example, the radial component of the velocity (equation (7a)) becomes

$$v_r = \sum_{l=0}^{\infty} \sum_{m=-l}^{l} a_l^m(r) Y_l^m(\theta, \varphi)$$

The coefficients in the spherical harmonic expansions are functions of radius only. The coefficients in the horizontal terms, b_l^m and c_l^m, are the spherical harmonic coefficients of the poloidal and toroidal components of the velocity, respectively. Similarly, the nonhydrostatic components of the stress tensor (τ_{rr}, $\tau_{r\theta}$, $\tau_{r\varphi}$) are expressed as

$$\tau_{rr} = d_l^m(r) Y_l^m \tag{7d}$$

$$\tau_{r\theta} = e_l^m(r) Y_{l,\theta}^m + f_l^m(r) Y_{l,\varphi}^m \tag{7e}$$

$$\tau_{r\varphi} = e_l^m(r) Y_{l,\varphi}^m - f_l^m(r) Y_{l,\theta}^m \tag{7f}$$

where the coefficients e_l^m and f_l^m are the spherical harmonic coefficients of the poloidal and toroidal components, respectively, of the shear stress, and τ_{rr} is the nonhydrostatic normal stress in the radial direction.

Substituting the expansions for velocity and stress together with those for pressure and density reduces (1)–(3) to a set of six coupled, first-order ordinary differential equations, or ODEs (four poloidal and two toroidal) [*Kaula*, 1975; *Hager and O'Connell*, 1979]. For instance, denoting the radial derivative of a_l^m by $\dot{a}_l^m$, the continuity equation (1) reduces to

$$\dot{a}_l^m = \frac{-2a_l^m}{r} + \frac{l(l+1)b_l^m}{r} \tag{8}$$

which depends only on the poloidal components of the velocity field.

By specifying six boundary values, the six coupled ODEs are solved for the three components of the velocity and the three components of the stress as a function of radius. The boundary conditions are taken to be no-slip at the surface (v_r, v_θ, v_φ specified everywhere) and free slip at the core-mantle boundary (v_{rr}, $\tau_{r\theta}$, $\tau_{r\varphi} = 0$). The equations are solved analytically via propagator matrices [*Hager and O'Connell*, 1979]. For radially varying viscosity the propagator matrices for the various layers are multiplied together, yielding the solution for the entire mantle. The expressions for all equations and the propagator matrices are derived and described in detail by *Hager and O'Connell* [1979, 1981].

Given that plate motions remain constant during plate stages (i.e., nonaccelerating), we assume that the net torque acting on each plate is zero, that is, the plates are in dynamic equilibrium [*Lliboutry*, 1972; *Solomon and Sleep*, 1974; *Forsyth and Uyeda*, 1975; *Solomon et al.*, 1975; *Chapple and Tullis*, 1977]. The continuity in time of plate velocities (away from plate boundaries) is supported by recent satellite geodetic data: very long baseline interferometry (VLBI) and Global Positioning System (GPS) experiments have shown that the present-day plate speeds and direction do not vary over short periods of time [*Ward*, 1990]. Moreover, the plate motions determined using VLBI and GPS are consistent with those calculated by averaging over the last several million years [*De Mets et al.*, 1990; *Ward*, 1990].

We predict plate motions by first computing the driving torques and then finding plate rotation poles such that the resisting torques and driving torques exactly balance. What allows us to predict any plate rotation vector, $\boldsymbol{\omega}_P$, is the fact that the resisting torques are linearly dependent on $\boldsymbol{\omega}_P$ while the driving torques are completely independent of $\boldsymbol{\omega}_P$. In this sense the problem of predicting plate motions is analogous to that of determining the terminal velocity $v_t = G^{-1}F_D$ of a piston moving through a viscous fluid and subject to a known applied force F_D, where G is the coefficient of the

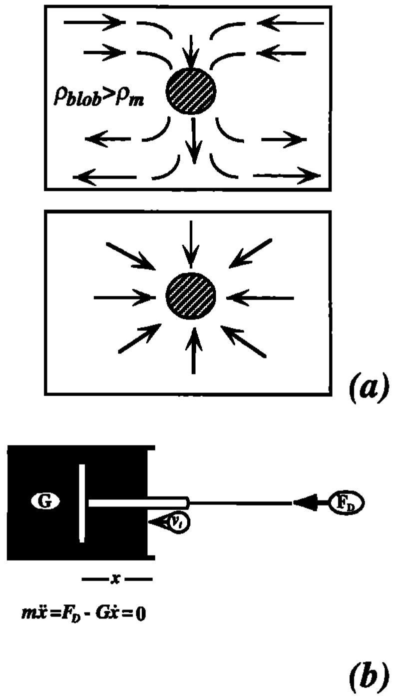

Figure 1. Schematic illustration of the way the mantle acts to drive plate motions. (a) Higher-density blob (slablet) sinking through a viscous fluid (mantle). A slab subducting in the mantle will induce flow to affect all plates, so that a plate not attached to slabs will move toward the loci of past subduction. (top) Vertical section. (bottom) Surface projection. (b) Dash pot model for a Maxwell viscous solid. In response to an applied force F_d, the plunger moves with a terminal velocity v_t determined by the viscosity of the fluid G. For times much longer than Maxwell relaxation times $\tau \sim G/K$, where K is the spring constant (such as those for the Earth), the dynamics of the system are completely determined by the viscosity. The terminal velocity is then given by $v_t = G^{-1}F_D$.

dissipative term, and depends on the viscosity of the fluid and the dimensions of the piston (Figure 1b).

In the case of plate tectonics the force balance is replaced by a torque balance expressed as

$$\boldsymbol{\omega} = \mathbf{M}^{-1}\mathbf{Q}_{\rm int}. \qquad (9a)$$

where $\boldsymbol{\omega}$ is a $3N$-dimensional vector (N is the number of plates) containing the respective three-component Euler rotation vectors of the plates. $\mathbf{Q}_{\rm int}$ contains the known applied torques due to internal density heterogeneities, while $\mathbf{M}$ depends on the viscosity structure and contains all the information on plate geometry (that is, $\mathbf{M}$ represents the resisting forces in the system).

The solution to (9a) is divided into two parts, whose solutions can be superposed because they are both subject to the same type of boundary condition and because the governing equations (e.g., (6)) are linear. First, for each plate P, we obtain $\mathbf{Q}_{{\rm int}_P}$ from

$$\mathbf{Q}_{{\rm int}_P} = \int_{A_p} \mathbf{r} \times \boldsymbol{\tau}_{\rm int}\, dA \qquad (9b)$$

where $\boldsymbol{\tau}_{\rm int}$ is the basal shear stress on each plate excited by internal density heterogeneities, $\mathbf{r}$ is the position vector and A_p is the area of the plate. The basal shear stress $\boldsymbol{\tau}_{\rm int}$ is obtained using the propagator matrix solution referred to above, subject to the surface boundary condition $v_r = v_\theta = v_\varphi = 0$. Second, the components of the $3N \times 3N$ matrix $\mathbf{M}$, analogous to G in the Maxwell model and given by

$$Q_{i_{\rm res}} = M_{ij}\omega_j \qquad i, j = 1 - 3N \qquad (9c)$$

are determined as follows: A propagator matrix solution to the basal shear stresses, $\boldsymbol{\tau}_j$, is determined subject to a surface boundary condition consisting of a unit rotation in one direction of a single plate, ω_j, in the absence of internal loads. This solution determines individual contributions to the resisting torques, $\mathbf{Q}_{\rm res}$, given by

$$q_{ij_p} = \int_{A_p} \mathbf{r} \times \boldsymbol{\tau}_j\, dA \qquad (9d)$$

such that $Q_{i_{\rm res}} = \Sigma_j\, q_{ij}$. The components of $\mathbf{M}$ are then given by $M_{ij} = q_{ij}/\omega_j$. The off-diagonal elements are nonzero because movement of any one plate will generate viscous stresses at the base of all the others through the induced internal circulation. (For a detailed discussion, see *Ricard and Vigny* [1989].)

The prescribed internal density field is described via a spherical harmonic expansion to degree and order 25 of the 180 Myr of subduction history preceding each stage and the corresponding lithospheric contribution (the inherent density difference between continents and oceans plus lithospheric thickening). Similarly, the unit rotations about the three Cartesian axes are applied through their corresponding poloidal and toroidal coefficients expanded to the same degree and order.

The induced shear stresses are summed to degree and order 20. The integration for the torques on each plate is carried out on a one by one degree grid. Finally, the matrix $\mathbf{M}$ is inverted using singular value decomposition to obtain the rotation vector of each plate. Dynamical solutions can be found only up to an arbitrary net rotation vector. By properly conditioning the matrix, setting the smallest eigenvalues to zero, and using singular value decomposition, we automatically find the unique no-net rotation solution for a given prescribed density field.

2.4. Problems and Limitations

A number of limitations are inherent in our approach. Perhaps the most important is due to the singularity in the viscous stresses at plate boundaries. In trying to model piecewise continuous plate velocities with "fluid" plate boundaries, we incur a technical problem. At plate boundaries, where the velocity field is discontinuous, the viscous resistance increases unphysically as the logarithm of the highest harmonic degree retained in the flow field. We truncate our series at degree 20, but truncations at much higher degrees (50) do not significantly affect our results. (Correlation coefficients change by less than 0.01, and the best fitting absolute viscosity changes by less than 15%, as will be shown later.)

For the sake of simplicity we have made several assumptions. First, as we stated before, we have neglected the elastic forces at subduction zones; that is, when evaluating the balance of driving forces, we consider only the viscous forces due to the sinking slabs and not the elastic pull of the slab on the plate. Given the good agreement between our results and the observed plate motions, this does not seem to be a critical assumption. A second, more important, assumption is that of Newtonian rheology, which is chosen for mathematical convenience rather than physical relevance. Non-Newtonian rheology requires elaborate numerical procedures that are not warranted, at least yet, by the data available. Our model also does not allow the treatment of lateral viscosity variations.

Finally, we perform instantaneous flow calculations given a prescribed density field at a given time; in other words, this is not a full convection calculation. Moreover, our prescribed density field is constructed assuming that cold buoyancy dominates the density heterogeneity field, and neglecting active upwellings. If this is true, our model may be a good representation of the density distribution inside the Earth. However, a full convection calculation, although beyond the scope of this paper, will ultimately be necessary to determine the eventual fate and shape of slabs and how they are affected by the background flow in the mantle.

3. ANALYSIS OF GLOBAL PLATE MOTIONS

3.1. Data Sets and Error Estimates

The plate tectonic information required for modeling plate motions consists of the following elements: (1) global plate reconstructions for a given plate stage (a plate stage is defined as a period of time during which plate motions are relatively constant and whose time boundaries correspond to periods of large changes in plate motions, i.e., plate rearrangements), including not only the reconstructed positions of the continents and their margins for a given time, but also the complete plate boundaries for all the major plates in existence; (2) Euler rotation vectors for every plate and corresponding error ellipses; and (3) maps of reconstructed isochrons for the oceanic parts of the plates. The latter, combined with the knowledge of continental margin positions, are required to map the oceanic crust and its age, and thus the contribution to the density field and buoyancy forces that arises from the thickening of the oceanic lithosphere as it ages.

The task of gathering this information is not simple, and a variety of problems are presented to the nontectonicist. The first and foremost problem is the lack of complete plate boundary information in the published tectonics literature. For example, the tectonics literature may have several reconstructions for parts of the plate boundaries of the Phoenix plate, but seldom is there a complete reconstruction that includes all boundaries and the poles of rotations for the times of interest. Even less common is a global plate reconstruction that includes all plates such as that of *Gordon and Jurdy* [1986]. This lack of information reflects the daunting difficulties involved in inferring the positions of plate boundaries in the past (trenches leave only fuzzy records on continents and almost no record on the oceanic plates; oceanic plates are consumed on average every 100–200 Myr).

Assembling the poles of rotation for a given plate configuration in time is also difficult, particularly in an absolute reference frame, not only because rotation poles are model dependent but also because they are not always published along with the plate reconstructions, leading us to use plate boundaries and poles of rotations from different sources that may not be internally consistent. A complete global set of isochrons reconstructed back in time is unavailable in the published literature and must be obtained from various sources. Even a digital map for the present-day isochrons has only recently become publicly available [*Müller et al.*, 1994]. There are several available reconstructions for the positions of the continents in the Phanerozoic [e.g., *Smith et al.*, 1981; *Scotese*, 1990; *Royer et al.*, 1992], but they are not always consistent with the available plate boundaries, poles of rotations, and isochrons, nor are they always available at the times of interest or for time intervals of relatively short duration.

Inherent in these difficulties is the fact that assembling reconstructions, boundaries, poles, isochrons, etc., from different sources leads to inconsistencies in the database, for example, (1) in the location of the plate boundaries (different authors generally use different reference magnetic anomalies to reconstruct) and (2) in the poles of rotation used to reconstruct the positions of the continents back in time, such that the 0 age isochron might not match the position of the ridge from the plate boundary information. These inconsistencies often manifest themselves only after all the information necessary for dynamic modeling has been gathered. Finally, a minor problem arises from the continuous adjustments to the geological timescale (both in age revisions and magnetic anomalies), and the different timescale standards (e.g., *Harland et al.* [1982] or the Decade of North American Geology (DNAG) timescale).

Keeping in mind the limitations presented above regarding the state of the available information, we have compiled a set of global plate reconstructions, plate rotation vectors, continental margin locations, and isochron maps from different published and unpublished sources in the form detailed below.

3.1.1. Plate boundaries and poles of rotation. For the calculations presented in this paper (the poloidal to toroidal partitioning of the plate velocity field, the construction of a density heterogeneity model based on subduction history, and the modeling of plate motions in the Cenozoic) we used tectonic information back to 180 Ma. For 11 plate stages, 6 in the Cenozoic (0–10, 10–25, 25–43, 43–48, 48–56, and 56–64 Ma) and 5 in the Mesozoic (64–74, 74–84, 84–94, 94–100 and 100–119 Ma) we compiled complete plate boundary sets and rotation vectors.

For the Cenozoic stages we used the global plate boundaries and poles of rotation in the hotspot reference frame, with a few minor modifications, of *Gordon and Jurdy* [1986]. For the Mesozoic we compiled global plate reconstructions and poles of rotations chosen, to the best of our knowledge, to match significant periods of plate rearrangements or equal time intervals. Most of the plate boundary information was digitized from the published paleogeographic atlas of *Scotese* [1990]. The details of the Farallon, Kula, and Izanagi plates for these reconstructions were extracted from the work of *Engebretson et al.* [1985]. The reconstructions of the Phoenix plate were compiled from the work of *Larson and Chase* [1972] and *Larson and Pitman* [1972]. Any missing plate boundaries were penned in as straight lines to close a circuit, with subduction zones always at the edges of continental margins.

For all these stages, the stage rotation poles (Table 1) in the hotspot reference frame were obtained from the data set of *Engebretson et al.* [1992], with the exception of the rotation poles for the Phoenix and Farallon plates, for which we used the poles from *Engebretson et al.* [1985]. For the period of time between 120 and 180 Ma, we used two plate stages 120–150, 150–180; the poles of rotations and the positions of subduction zones for these time periods are those inferred by *Engebretson et al.* [1992]. Maps of plate boundaries and plate velocities for the Cenozoic and Mesozoic reconstructions are shown in Figure 2.

In studying the present-day nature of plate kinematics (see section 3.2) we used three different absolute motion models, those of *Minster and Jordan* [1978] (AM1-2), *Gordon and Jurdy* [1986], and *Gripp and Gordon* [1990] (HS2-NUVEL1). These provide a good comparison of the differences between different plate motion models in the hotspot reference frame.

3.1.2. Continental margins and oceanic plate ages. The cooling and subsiding of the oceanic lithosphere as it ages, is the source of the ridge push force, i.e., thermal lithospheric thickening. First we use the past positions of the continental margins to determine the extent of the continental part of the plate. Then we assign a plate age to each oceanic block, defined as the area occupied by a box with dimension 1° × 1°, using the reconstructed isochron data set of the PLATES project [*Royer et al.*, 1992]. For each stage we use an isochron map corresponding to the reconstructed age of the plate boundary configuration of *Gordon and Jurdy* [1986], respectively, 0, 17, 34, 48, 48, and 64 Ma. These times are the ages (in the *Harland et al.* [1982] timescale) corresponding to the magnetic anomalies used by *Gordon and Jurdy* [1986] to

TABLE 1. Stage Poles for the Five Mesozoic Stages

Plate Name	*Code*	*Latitude*	*Longitude*	w, *deg Myr*$^{-1}$
		64–74 Ma		
Africa	AF	21.3	288.0	0.310
Antarctica	AN	65.2	247.7	0.170
Australia	AU	62.9	342.2	0.039
Caribbean	CA	−19.7	252.9	0.321
Eurasia	EU	7.7	269.7	0.273
Farallon	FA	24.4	111.0	0.906
India	IN	18.4	347.6	1.044
Kula	KU	2.5	135.2	1.362
North America	NA	−47.9	250.8	0.377
Pacific	PA	−21.9	88.9	0.632
Phoenix	PH	−16.9	296.9	1.201
South America	SA	−50.7	234.9	0.331
		74–84 Ma		
Africa	AF	21.3	288.0	0.310
Antarctica	AN	65.7	167.6	0.388
Australia	AU	57.3	131.1	0.276
Eurasia	EU	−8.3	223.8	0.286
Farallon	FA	−8.8	137.2	1.023
India	IN	8.8	359.5	1.169
Kula	KU	−28.6	100.1	1.295
North America	NA	−45.2	208.3	0.479
Pacific	PA	−47.5	118.6	0.922
Phoenix	PH	−16.7	296.6	1.201
South America	SA	−50.8	209.7	0.408
		84–94 Ma		
Africa	AF	2.4	329.1	0.335
Antarctica	AN	18.0	138.6	0.344
Australia	AU	−9.8	112.6	0.356
Eurasia	EU	−50.0	219.0	0.385
Farallon	FA	−1.9	143.9	1.050
India	IN	5.1	9.8	0.298
Izanagi	IZA	−27.8	67.2	1.922
North America	NA	−58.8	207.1	0.544
Pacific	PA	−47.5	118.6	0.922
Phoenix	PH	−51.1	282.4	0.528
South America	SA	−26.1	164.4	0.325
		94–100 Ma		
Africa	AF	2.4	329.1	0.335
Antarctica	AN	18.0	138.6	0.344
Eurasia	EU	−44.4	212.3	0.401
Farallon	FA	−1.2	144.3	1.055
India	IN	5.1	9.8	0.298
Izanagi	IZA	−27.8	67.2	1.962
North America	NA	−53.8	201.8	0.572
Pacific	PA	−47.5	118.6	0.922
Phoenix	PH	−41.3	285.4	0.577
South America	SA	−26.1	164.4	0.325
		100–119 Ma		
Africa	AF	2.4	328.5	0.322
Antarctica	AN	17.3	139.5	0.355
Eurasia	EU	−51.7	205.2	0.508
Farallon	FA	11.7	190.7	0.615
India	IN	5.0	11.0	0.286
Izanagi	IZA	−25.2	54.1	1.637
North America	NA	−53.5	202.5	0.556
Pacific	PA	−78.2	295.0	0.574
Phoenix	PH	−8.8	308.6	1.183
South America	SA	−25.2	165.1	0.319

The stage poles for each plate were calculated from the poles of Engebretson et al.

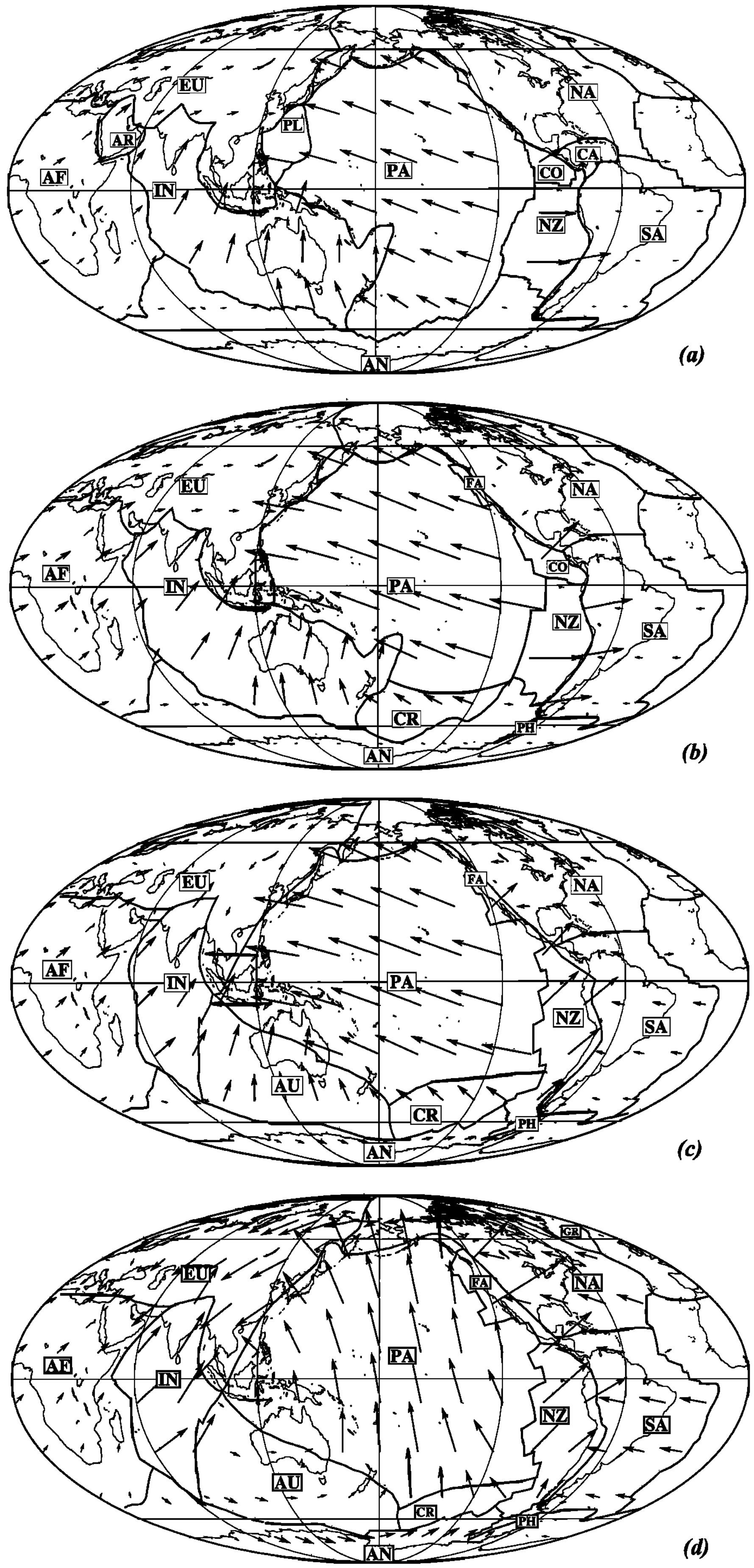

Figure 2. Observed velocities in the hotspot reference frame for (a) 0–10, (b) 10–25, (c) 25–43, (d) 43–48, (e) 48–56, and (f) 56–64 Ma [*Gordon and Jurdy*, 1986] and (g) 64–74, (h) 74–84, (i) 84–94, (j) 94–100, and (k) 100–119 Ma (poles of rotation shown in Table 1). The plate boundaries are indicated by the solid black lines. The names of the plates are indicated by the two- or three-letter codes defined in Table 1. The arrows indicate the direction of motion of each plate, and the size of the arrow is proportional to the magnitude of the plate velocity. For reference, the continents are shown in their present position.

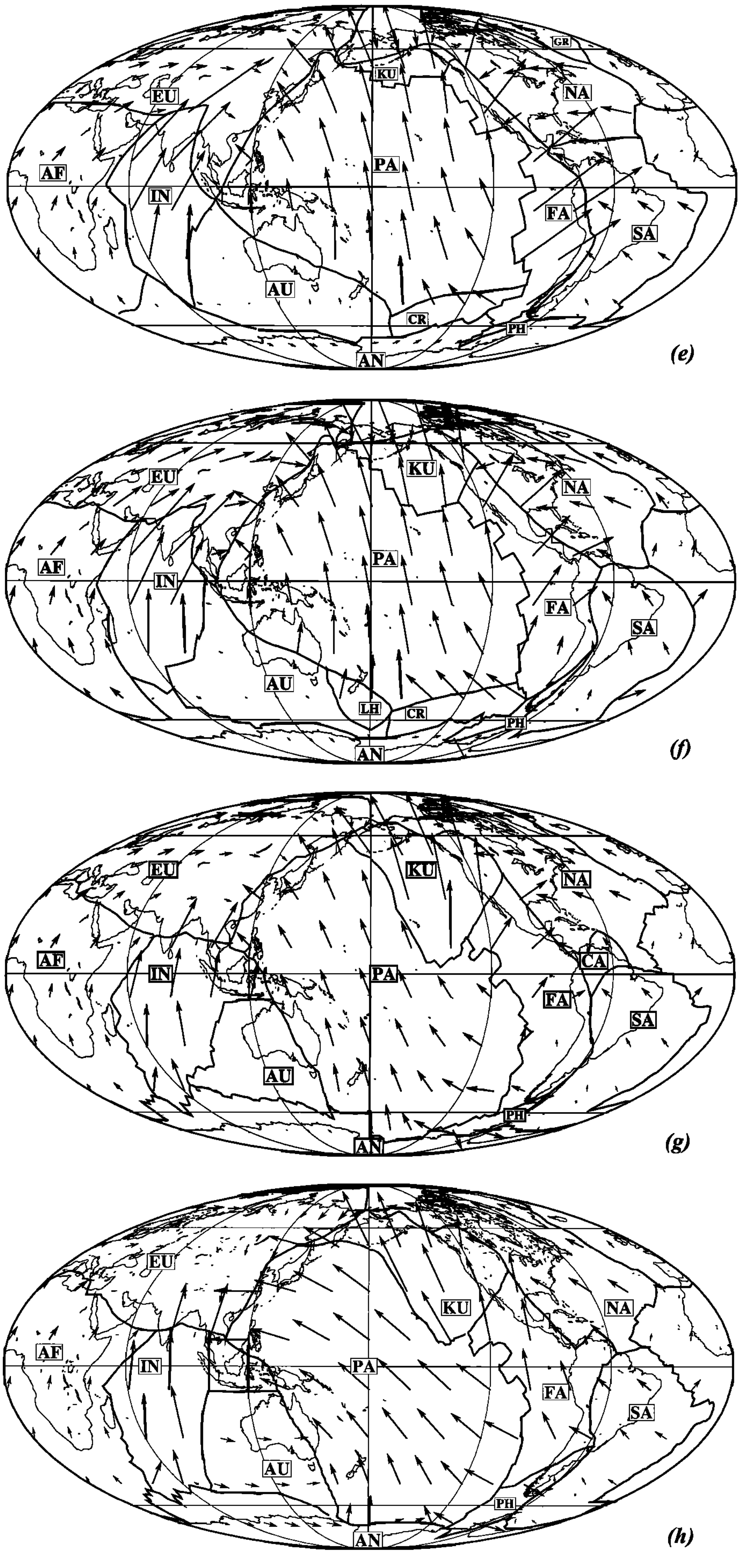

Figure 2. (continued)

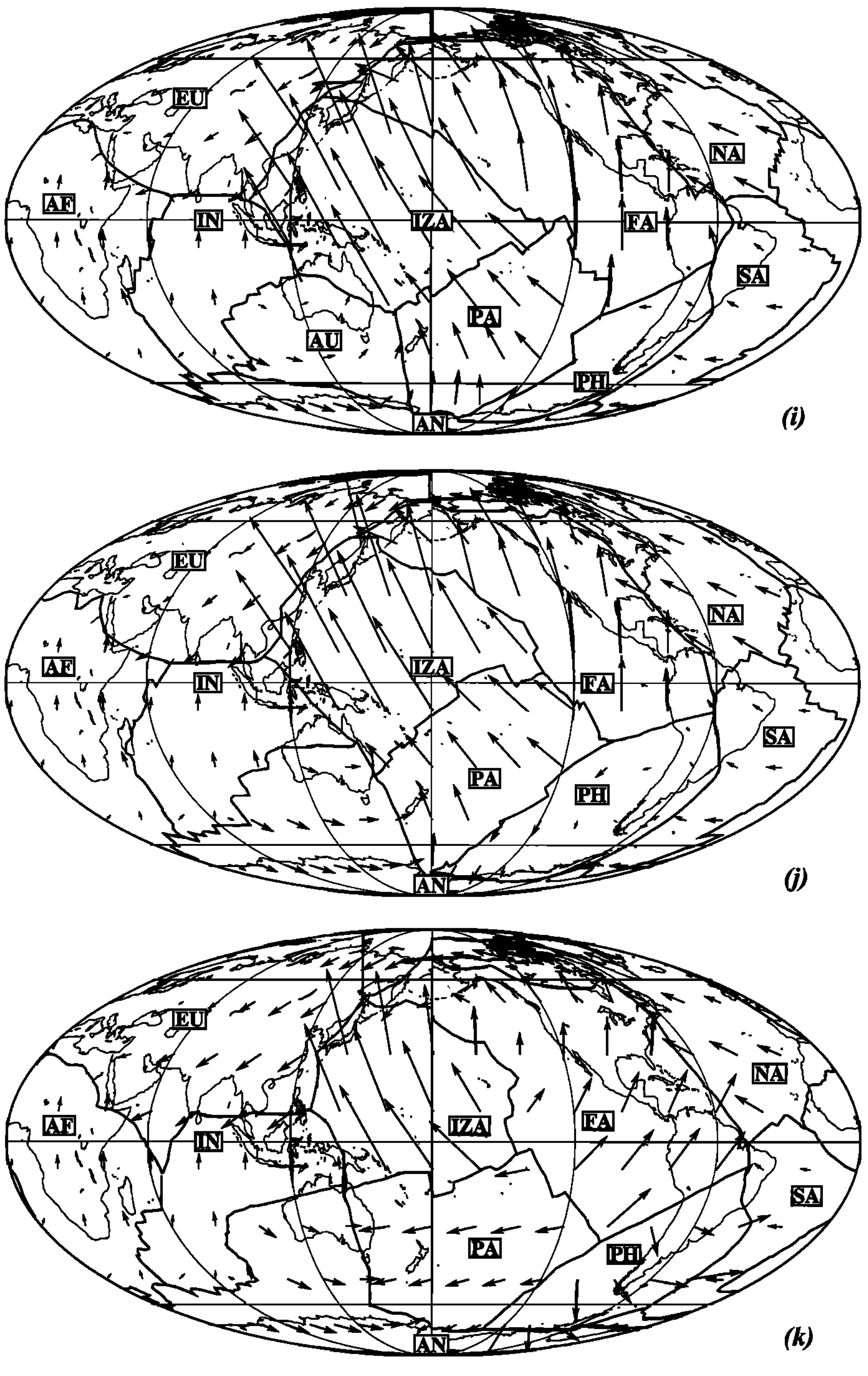

Figure 2. (continued)

draw the plate boundaries for each stage, that is, anomalies 0, 5, 13, 21, and 27.

Each block defined to be noncontinental is assigned the age of the nearest isochron and is shown for the present and 64 Ma in Plates 1a and b. (To complete the age map, we added the data on marginal basins manually from the present-day age map of *Sclater et al.* [1981]). To account for the paucity of isochron data as we go back in time, we have chosen a maximum age of 80 Ma for the oceanic lithosphere at all stages except for the present day. A younger cutoff age does not significantly affect our results.

3.1.3. Error estimates for rotation vectors. Given the limitations of the record in the past, any meaningful analysis of plate tectonic history must include an estimate of the uncertainties in the computed quantities. For both the kinematic analysis (in the following section) and the modeling of driving forces we include estimated error bounds for all quantities. However, calculating error bounds for finite rotations on a sphere (or worse yet for multiple ones) is complex and time-consuming [*Jurdy and Stefanick*, 1987; *Chang et al.*, 1990]. Here we use a simple approximate method to estimate maximum possible uncertainties.

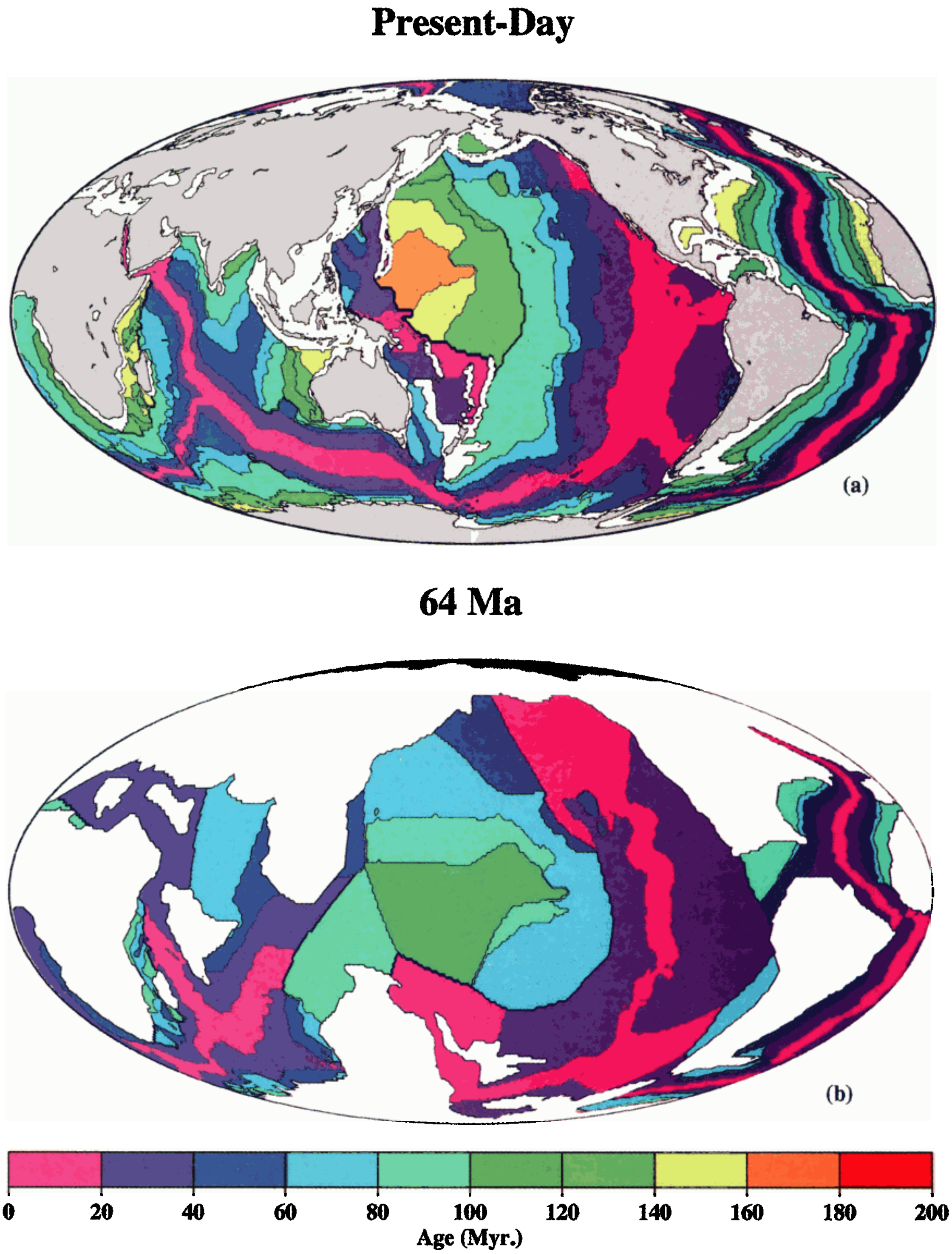

Plate 1. Ages of the present-day oceanic lithosphere, in millions of years, inferred from the isochron data of *Royer et al.* [1992]. The continental margins are shown in white. The information on marginal basins is from the age map of *Sclater et al.* [1981]. (b) Ages at 64 Ma used for the 56–64 Ma stage.

In the kinematic analysis of toroidal-poloidal partitioning (see section 3.2) for the stages since 84 Ma we compute 2σ confidence intervals for the poloidal and toroidal velocities, the ratio of toroidal to poloidal power, and the net rotation of the lithosphere with respect to the mantle. Unfortunately, uncertainties in the positions of the plate boundaries are difficult to quantify and therefore are not included in our error analysis. We do however, restrict ourselves to relatively long wavelengths (spherical harmonic degree 20, which corresponds to ~2000 km) so that errors in plate boundary locations of 1000 km or less will not affect our conclusions.

For the present day we have used the error ellipses on the poles of rotation of each plate from the work of

Minster and Jordan [1978] and *Gripp and Gordon* [1990] and their estimates of formal uncertainties in the angular velocities of each plate. For all previous stages back to 84 Ma, we estimated a maximum error ellipse from formal uncertainties in the relative motion of plate pairs, to which we added the error associated with the plate-hotspot rotation vectors from *Molnar and Stock* [1987]. To take into account the paucity of error information on past poles of rotation, we have used the largest estimated error ellipse at any given stage for all plates in that stage. The magnitude of the error ellipse is forced to increase for every stage and to be the maximum possible error (±180° in latitude and ±360° in longitude) for the last stage (74–84 Ma). Further, we have assumed for simplicity, given the lack of information on their orientation, that the error ellipses are aligned with the N-S axis.

The errors in the poles of rotation and in the angular velocities are propagated to all calculated quantities through a Monte Carlo sampling of the estimated error ellipses. We are confident that this leads to an overestimation of errors for all values. For example, the magnitude of the poloidal and toroidal velocities and their uncertainties, shown in Figure 3a, is dominated by the Pacific plate, for which we have chosen error bounds as described above for all times, while in reality the error ellipse for the Pacific plate is much smaller than the maximum error ellipse chosen. The effect is to overestimate the magnitude of the 2σ bands by a factor between 2 and 4, and results in error bounds of comparable magnitude for all times prior to 10 Ma, while in fact those after 64 Ma should get progressively smaller than those for the Mesozoic. For the earlier Mesozoic, formal uncertainties are unavailable, so we show the range of results obtained with two alternative sets of poles [*Engebretson et al.*, 1985, 1992].

3.2. Kinematic Analysis

We have previously analyzed in detail the nature of plate motions in the last 120 Myr [*Lithgow-Bertelloni et al.*, 1993] in terms of the partitioning into poloidal and toroidal components of the surface velocity field, our goals being to search for changes in the nature of plate motions and the possible elucidation of their dynamical causes. Many authors had previously shown that when surface plate motions are decomposed into their trench-ridge (surface divergence or poloidal field) and transform components (radial vorticity or toroidal field), the toroidal component is comparable in magnitude to the poloidal component [*Hager and O'Connell*, 1978; *Forte and Peltier*, 1987; *O'Connell et al.*, 1991; *Olson and Bercovici*, 1991; *Čadek and Ricard*, 1992]. This large toroidal component is the direct result of the presence of Earth's rigid plates [*Ricard and Vigny*, 1989; *Gable et al.*, 1991; *O'Connell et al.*, 1991; *Vigny et al.*, 1991], since toroidal motion is not generated in a homogeneous convecting fluid. The toroidal to poloidal ratio should be 0 for an Earth without plates and ~1 for plates with uncorrelated or random motions [*Olson and Bercovici*, 1991].

The ratio of toroidal to poloidal power is a function of the degree of correlation among plate motions and the geometry of the plate boundaries. For example, for the same set of plate velocities a change in the orientation of a subduction zone from normal to the velocity vector to oblique will signify a marked increase in toroidal power and a corresponding decrease in the poloidal part. Any temporal change in the toroidal-poloidal partitioning ratio that is not the direct result of modification in the plate boundaries alone may thus indicate changes in the coupling between plates and mantle driving forces or perhaps changes in the driving forces themselves. In the context of this work on plate-driving forces it is interesting to reexamine the kinematic nature of Cenozoic and Mesozoic plate motions and use both this analysis and comparisons between predicted and observed toroidal to poloidal ratios to guide our understanding of the failure of our models and to discover the dynamical processes that might spur or enable plate rearrangements.

3.2.1. Poloidal and toroidal representation of plate velocities. We have calculated the toroidal and poloidal components of plate motions and the toroidal to poloidal ratio since 120 Ma using the global plate reconstructions already described. For each stage we calculated by direct expansion the spherical harmonic coefficients, to degree and order 50, of the surface divergence and radial vorticity, given respectively by

$$\nabla_h \cdot \mathbf{v}(\theta, \varphi) = \sum_{l=0}^{50} \sum_{m=0}^{l} D_l^{m\left[\substack{\cos \\ \sin}\right]} Y_l^m(\theta, \varphi) \qquad (10a)$$

$$(\nabla \times \mathbf{v}(\theta, \varphi)) \cdot \hat{r} = \sum_{l=0}^{50} \sum_{m=0}^{l} V_l^{m\left[\substack{\cos \\ \sin}\right]} Y_l^m(\theta, \varphi) \qquad (10b)$$

where $\mathbf{v}$ is the surface velocity, a function of colatitude θ, and longitude φ, and $\hat{r}$ is the radial unit normal. The coefficients of the divergence and vorticity expansions are easily converted to a poloidal-toroidal representation of the velocity field. The poloidal and toroidal coefficients are given respectively by

$$S_l^{m\left[\substack{\cos \\ \sin}\right]} = \frac{D_l^{m\left[\substack{\cos \\ \sin}\right]} a}{l(l+1)} \qquad (11a)$$

$$T_l^{m\left[\substack{\cos \\ \sin}\right]} = \frac{V_l^{m\left[\substack{\cos \\ \sin}\right]} a}{l(l+1)} \qquad (11b)$$

where a is the radius of the Earth and l is the harmonic degree. The velocity spectra for both components decay approximately as l^{-2}. The amplitude of each harmonic degree l, that is, the total power at each wavelength, is given by the degree variance, defined as

$$\sigma_\iota^2(l) = \sum_{m=0}^{l} (A_{l_\iota}^{m[\cos]})^2 + (A_{l_\iota}^{m[\sin]})^2 \qquad (12)$$

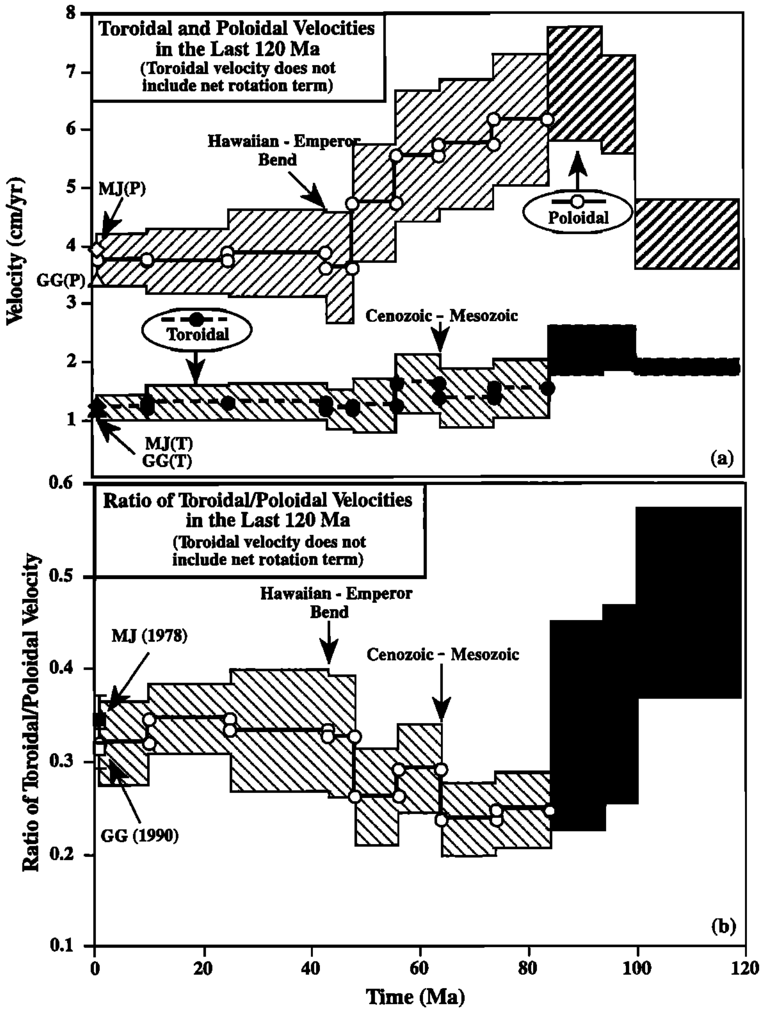

Figure 3. (a) Toroidal (solid circles and dashed line) and poloidal (open circles and solid line) velocities for the last 120 Myr, net rotation not included. The Cenozoic is based on *Gordon and Jurdy* [1986], and the Mesozoic is based on *Engebretson et al.* [1985, 1992]. The circles mark the beginning and end of each stage. The light hatched areas (slanted upward to the right for poloidal and to the left for toroidal) around the solid and dashed lines represent the 2σ confidence interval on the velocities. The dark hatched areas represent the range (not formal uncertainties) of velocities from 84 to 119 Ma, given two sets of rotation poles [*Engebretson et al.*, 1985, 1992]. The open and solid rhombohedra labeled MJ are the poloidal and toroidal velocity, respectively, for AM1-2 [*Minster and Jordan*, 1978]; the open and solid triangles labeled GG are the corresponding values for HS2-NUVEL1 [*Gripp and Gordon*, 1991]. The 2σ error bars are smaller than the symbols. (b) Ratio of toroidal to poloidal velocities; net rotation not included. Hatching is as in Figure 3a. Solid and open squares are the ratios for AM1-2 and HS2-NUVEL1, respectively.

where the index i designates the poloidal or toroidal field and the $A_l^{m\left[\begin{smallmatrix}\cos\\ \sin\end{smallmatrix}\right]}$ represent the poloidal $(S_l^{m\left[\begin{smallmatrix}\cos\\ \sin\end{smallmatrix}\right]})$ or toroidal $(T_l^{m\left[\begin{smallmatrix}\cos\\ \sin\end{smallmatrix}\right]})$ spherical harmonic coefficient. The magnitude of the poloidal and toroidal fields, v_i, can be defined as a sum over all harmonic degrees, given by

$$v_i = \sqrt{\sum_{l=0}^{20} \sigma_i^2(l)}$$

The magnitude of these fields is shown as a function of time in Figure 3a. We have excluded toroidal degree 1 from the calculations in Figure 3 to obtain results less dependent upon the particular plate motion model chosen. This term corresponds to the net rotation of the lithosphere with respect to the mantle in the hotspot reference frame. Its value is therefore dependent on the reference frame.

3.2.2. Discussion of kinematic results. Figure 3a shows a significant overall decrease in plate velocities from 84 Ma to 48 Ma (late Mesozoic to early Cenozoic). The ratio of toroidal to poloidal power (Figure 3b) has increased by nearly 30% from ~0.25 at 84 Ma to ~0.35 at present. Given the estimated errors in plate velocities, this increase is most likely significant and corresponds well with an overall decrease in the rate of plate motions. The Mesozoic results appear to indicate that there is also a considerable increase in the partitioning ratio with the overall decrease in plate motion at this time. However, it is hard to evaluate the exact meaning of these values because these older reconstructions are more uncertain. The most striking result is the fact that these changes in partitioning (and overall plate motion) are due almost entirely to changes in the poloidal component, while the toroidal component (excluding the changes in net rotation [*Lithgow-Bertelloni et al.*, 1993]) has remained relatively constant.

Do these changes result from varying plate geometry alone, or do they indicate more fundamental variations in the dynamics of plate motions? One way to resolve this issue is to test the hypothesis that observed partitioning ratios are the result of random, or uncorrelated, plate motions [*Olson and Bercovici*, 1991], which would imply that statistically significant changes in the partitioning ratio are merely the result of evolving plate boundary configurations. We have shown [*Lithgow-Bertelloni et al.*, 1993] that observed plate motions (1) are

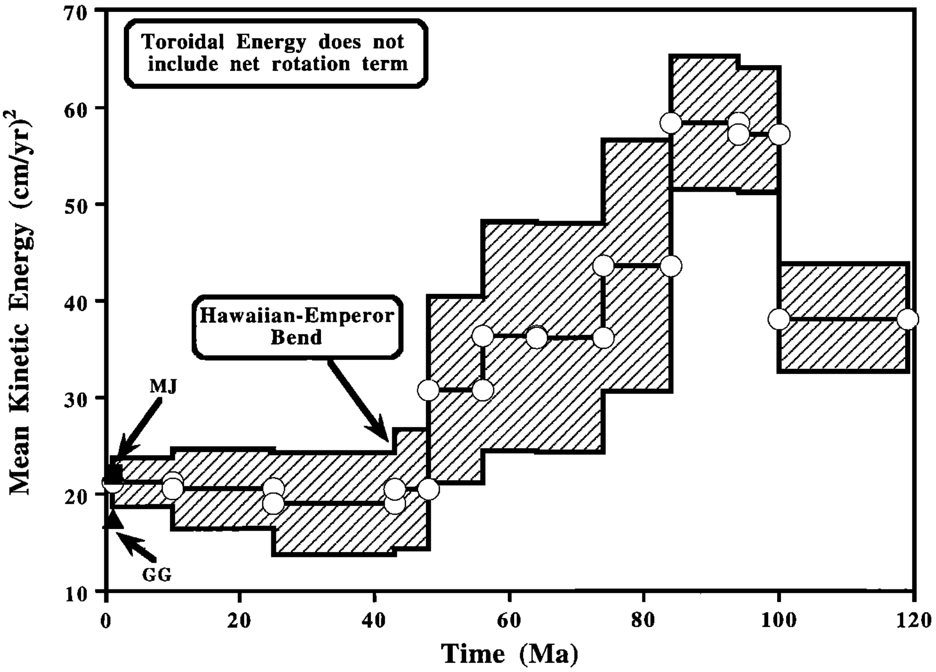

Figure 4. Kinetic energy, per unit mass, of plate motions (open circles and solid line) for the last 120 Myr. The Cenozoic is based on *Gordon and Jurdy* [1986], and the Mesozoic is based on *Engebretson et al.* [1985, 1992]. The circles mark the beginning and end of each stage. The light hatched areas around the solid line represent the 2σ confidence interval. The hatched areas from 84 to 119 Ma represent the range (not formal uncertainties) of values of kinetic energy obtained given two sets of rotation poles as in Figure 3. The solid square labeled MJ is the value for AM1-2 [*Minster and Jordan*, 1978], and the solid triangle labeled GG is the value for HS2-NUVEL1 [*Gripp and Gordon*, 1991]. The 2σ error bars are smaller than the symbols. Note that the kinetic energy is at a minimum for the stage immediately postdating (25–43 Ma) the bend in the Hawaiian-Emperor bend (43 Ma).

not equipartitioned and (2) do not appear to be random for any of the plate motion models considered.

Our most important result is the notable difference between plate motions in the periods 0–48 Ma and 48–84 Ma: During periods of high spreading and subduction rates (early Cenozoic and late Mesozoic), poloidal motions are more dominant, and the toroidal to poloidal ratio is more nearly minimized with respect to the existing plate geometries [*Lithgow-Bertelloni et al.*, 1993]. Although it is difficult to assess the cause of these temporal changes, we note that the changes we observe are preceded by an apparently intense period of mantle plume activity [*Larson*, 1991; *Richards et al.*, 1991] and that the overall kinetic energy of plate motions was much higher (Figure 4), reaching a minimum at 43 Ma and remaining almost constant until the present day.

Mantle plumes may provide an explanation for the observed changes in the poloidal component. Plumes will cause more dominantly divergent (poloidal) plate motions, since they tend to create new spreading centers and triple junctions and in so doing, to create new plates. (In the limit as we go from relatively few plates to infinitely many plates, the toroidal component of plate motion must vanish.) If we look at the reconstructed positions of the largest oceanic plateaus (such as Ontong-Java and Kerguelen) and the shift in the locus of the maximum average poloidal field prior to 48 Ma and its present position, shown in Plates 2a and 2b, we observe a strong visual correlation, supporting our speculation.

4. MANTLE HETEROGENEITY AND SUBDUCTION HISTORY

4.1. Assumptions

Our model differs from other forward models based on density heterogeneity fields in two respects. First, we assume that density heterogeneity below the lithosphere is subducted material, so that our models are based on geologically constrained past subduction histories and lithospheric heterogeneity rather than being inferred from seismic tomography [e.g., *Ricard and Vigny*, 1989; *Woodward et al.*, 1993]. The second difference is that our approach allows us to predict past plate velocities. We have constructed a model for the density heterogeneity of the mantle derived from the last 180 Myr of subduction history. Our goal is not to discern the exact details of the lateral density structure of the mantle but rather to construct the most straightforward model possible of plate motions that is consistent with a broad range of

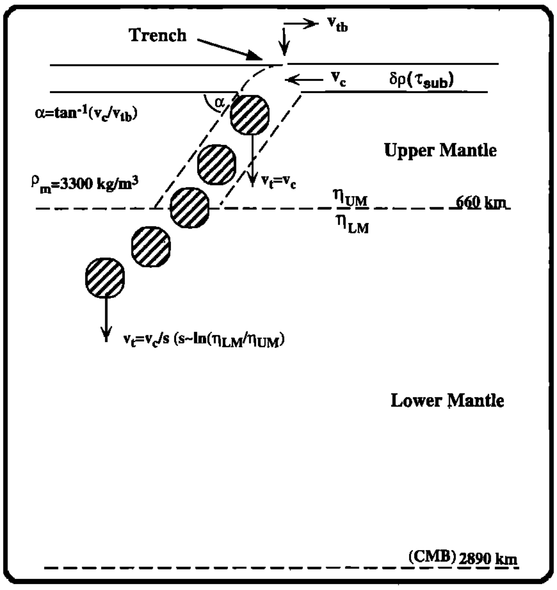

Figure 5. Cartoon representing the construction of a density heterogeneity model for the Earth based on subduction history. Slabs are introduced into the mantle directly below the trench and are assumed to sink through the upper mantle with a terminal velocity equal to the plate convergence rate. The terminal velocity decreases in the lower mantle by a factor s proportional to the viscosity contrast between upper and lower mantle.

geological and geophysical constraints on global plate motions and mantle density structure.

The main assumption underlying our model is that cold, subducted slabs are the main source of thermal buoyancy in the mantle. We have further assumed that thermal diffusion does not alter the signature of the slab in a period of ~200 Myr. This is justified because we are mainly interested in mantle structure and flow on length scales of the order of 1000 km, which yield characteristic thermal equilibration timescales of order 10^9 years. We have also assumed that slabs sink vertically in the mantle, following the implication of slow relative motion among hotspots that there is little horizontal advection of deep mantle material on timescales of order 100 Myr or less. Finally, we have allowed the slabs to freely penetrate the 670-km discontinuity so that there is uninhibited mass exchange between the upper and lower mantle. In other words, we have implicitly assumed whole mantle convection. However, our results are not pertinent to a discussion of single versus layered mantle convection due to a chemically heterogeneous mantle and/or to the effects of a strongly endothermic phase transition on the flow. To address the issue of layered convection, we would need to know what happens to the slabs as they reach the 670-km discontinuity (all slabs older than ~30 Ma). The behavior of slabs as they approach the 670-km discontinuity remains unresolved. Seismic observations show that most slabs penetrate the discontinuity, while some may be deflected by it [*Creager and Jordan*, 1986; *Van der Hilst et al.*, 1991, and references therein]. Given these uncertainties and the lack of sophisticated numerical procedures that can incorporate plates along with phase transitions and chemical layering, we limit our models to a whole mantle scheme.

4.2. Subduction History

The history of subduction is computed with a kinematic model schematically illustrated in Figure 5, rather than with a full convection calculation. The density anomalies due to subducted slabs are introduced into the mantle via the following simple model. For each Cenozoic stage we compute a subduction history due to the previous 180 Myr of subduction using the plate motions and boundaries described above.

For every time increment dt (5 Myr), unit trench length, and plate thickness, a mass anomaly ("slablet") $dm = \Delta\rho v_c dt$, where $\Delta\rho$ is the density contrast between the slab and the ambient mantle and v_c is the convergent velocity in the hotspot reference frame, is introduced at a depth $dz = v_T dt$ directly below the trench, where v_T is the terminal velocity of the slablet. The resulting slab geometry is therefore vertical for all slabs, which is in disagreement with seismic observations of Wadati-Benioff zones. However, since in the plate stage reconstructions the position of subduction zones changes from stage to stage, an effective dip angle is introduced similar to the numerical procedure of *Mitrovica et al.* [1989]. This effective dip angle α can be defined as $\alpha = \tan^{-1}(v_c/v_{tb})$, where v_{tb} is the trench rollback velocity. The migration of the trench in the plate reconstructions is based on geological observations of the change in the position of the volcanic arcs as a function of time. For each stage the subduction history is allowed to run to the end of the stage, letting the upper mantle slabs corresponding to that stage develop in full.

We take the density contrast $\Delta\rho$ to be 0.080 g cm^{-3} [*Ricard et al.*, 1993] and assign a surface density contrast equal to

$$\Delta\sigma = \Delta\rho\sqrt{\frac{\text{age}}{90}} \qquad (13)$$

where the age is in million years, yielding a lithosphere approximately 100 km thick at 90 Ma. The age of the slabs at the time of subduction was estimated for the Cenozoic from the oceanic plate age map of *Sclater et al.* [1981]. For the Mesozoic the age of all slabs is assumed to be 90 Ma, an appropriate average value in lieu of better information.

For the Cenozoic density heterogeneity models, we assume that the plate boundary configuration and velocity prior to 180 Ma were the same as those for the stage 150–180 Ma. This assumption is not very severe, as most of the slabs associated with that period of time have sunk well into the lower mantle even by 64 Ma. Using less time for subduction or different configurations prior to 180 Ma does not significantly affect our results.

The slabs are allowed to penetrate the 670-km discontinuity, and they are assumed, reasonably, to become dynamically inert when they reach the core-mantle boundary. (Mass anomalies located near a chemical interface such as the CMB are locally compensated, thus giving no contribution to the geoid or to driving fluid motions [*Ricard et al.*, 1993]; they could, however, affect the topography of the CMB or its seismic structure.) For each slablet the terminal velocity v_T is assumed to be equal to the plate convergence rate v_c in the upper mantle, and we set $v_T = (1/s)v_c$ in the lower mantle. The slowing factor s is proportional to ln (η^*_{LM}), where η^*_{LM} is the viscosity contrast between the lower and upper mantle [*Ricard et al.*, 1993; see also *Gurnis and Davies*, 1986; *Richards*, 1991]. The location of the slabs in the mantle due to the last 180 Myr of subduction history using a slowing parameter of 4 is shown at seven different depths in the mantle in Figure 6 for the present day and 56 Ma.

4.3. Oceanic Lithosphere

To better account for the buoyancy forces that drive plate motions, we add the contribution due to the thermal thickening of the oceanic lithosphere to our slab model. Given the age distribution at each plate stage, for each oceanic block there is a mass anomaly defined as

$$\Delta m = \Delta\rho_{oc} h_{oc} + \Delta\rho_{om} h_{age} \qquad (14)$$

where $\Delta\rho_{oc} h_{oc}$ is the mass anomaly due to the oceanic crust, assigned a density of 2.900 g cm^{-3} (Table 2 shows the density structure assumed for the continental and oceanic columns), and $\Delta\rho_{om} h_{age}$ is the mass anomaly due to the underlying mantle. The thickness h_{age} has the usual $\sqrt{age}$ dependence, $h_{age} = S\tau^{1/2}$. We use the empirically determined value $S = \sqrt{\pi} \times 10^{-3}$ of *Phipps Morgan and Smith* [1992]. This relation yields a 100-km-thick lithosphere at an age of 100 Ma. The density contrasts, $\Delta m/(h_c + h_m)$, of both oceanic and continental blocks are converted to distributed surface density contrasts [*Hager and O'Connell*, 1981]

$$\sigma = \Delta\rho z^2/2d \qquad (15)$$

where $\Delta\rho$ is the inherent volumetric density contrast, z is the total thickness of the block, and d is the depth at which the density contrast is imposed, in this case the bottom of the layer.

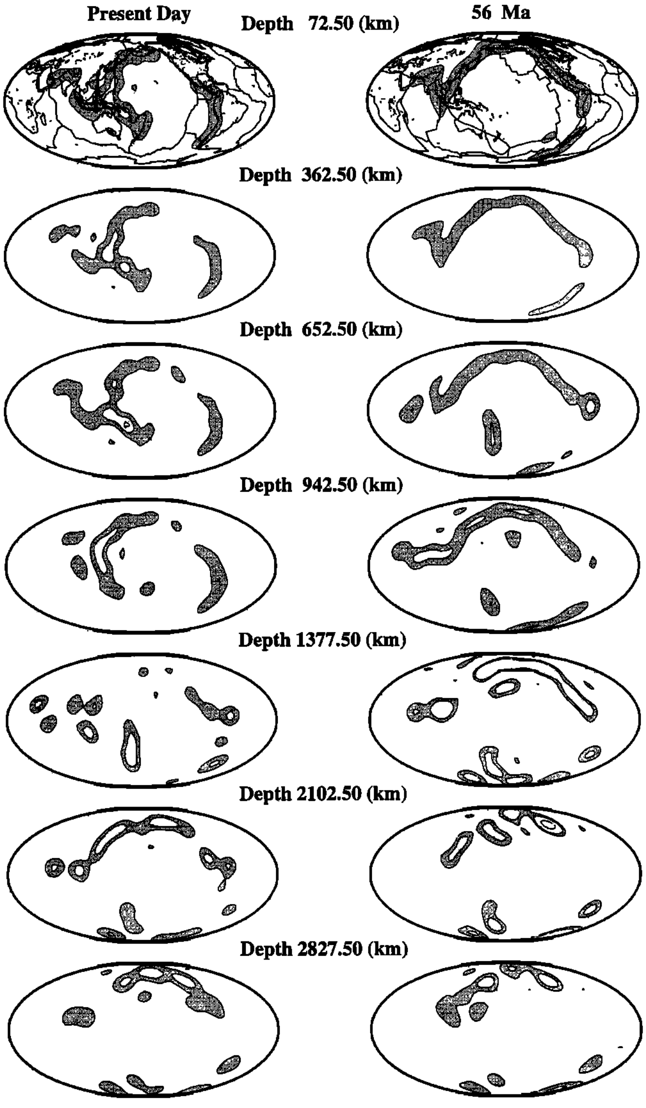

Figure 6. (a) Mantle density heterogeneity model for (a) the present-day Earth, resulting from 200 Myr of subduction, and (b) 56 Ma. The surface densities associated with seven layers at different depths (three for the upper mantle and four for the lower mantle) are shown from the top of the mantle to the core-mantle boundary. Contoured regions represent areas of high density with respect to the surrounding mantle, in other words, the location of the subducted slabs at that depth. The spatial and temporal changes in the location of subduction (from mostly the northern Pacific to the western Pacific) are well illustrated by the high densities in the northern regions at the bottom of the mantle and the high density regions in the western Pacific for the upper mantle. The subduction of the oceanic part of the Indian plate under Eurasia is also well illustrated. In the top panel the plate boundaries and the continental outlines in their present position have been superposed for reference.

4.4. Continental Lithosphere

A contribution to plate forces might arise from the inherent density difference between continents and oceans. Unfortunately, this effect is difficult to assess. If continents are rigid, then there is no contribution to the driving torques. If, on the other hand, we consider the tendency toward gravitational spreading, then continents contribute a large negative mass anomaly, which will tend to oppose the effect of thickening of the oceanic lithosphere [*Frank*, 1972; *Hager and O'Connell*, 1981]. In the latter case the difference between oceanic and continental density structure contributes a somewhat larger torque on the plates than does lithospheric thickening. The latter can be taken into account, to first order, by using the same density model for all continental regions, shown in Table 2. The continents consist of

TABLE 2. Density Structure Assumed for the Oceanic and Continental Lithosphere

Depth	*Density, kg m^{-3}*
Oceanic	
0–8 km	2900
8 km to Z_{age}	3380
Z_{age} to 2890 km	3300
Continental	
0–33 km	2800
33–100 km	3380
100–2890 km	3300

The depth Z_{age} of the bottom of the lithosphere varies as the square root of age.

33-km-thick crust with a density of 2.800 g cm^{-3} and an underlying mantle, 100 km in thickness, which we have assumed has the same density as the suboceanic mantle, 3.380 g cm^{-3}. The surrounding mantle is assumed to have a density of 3.300 g cm^{-3}. Each continental block then contributes a mass anomaly per unit cross-sectional area given by

$$\Delta m = \Delta\rho_{\mathrm{cc}} h_{\mathrm{cc}} + \Delta\rho_{\mathrm{cm}} h_{\mathrm{cm}} \tag{16}$$

where $\Delta\rho_{\mathrm{cc}} h_{\mathrm{cc}}$ is the mass anomaly due to the continental crust and $\Delta\rho_{\mathrm{cm}} h_{\mathrm{cm}}$ is the anomaly due to the mantle underlying the continents. Here we have included the latter effect, but the final results are hardly affected by its presence.

4.5. Model Calibration With Geophysical Observables

4.5.1. Seismic heterogeneity. As a first test of the ability of our model to represent the density heterogeneity of the mantle, we compare our subduction history model with two recent global seismic tomography inversions, S12WM13 [*Su et al.*, 1994], and SAW12D [*Li and Romanowicz*, 1996]. The lateral variations in seismic velocities imaged by seismic tomography can be related to variations in the density structure of the mantle. Generally, seismic velocities are converted to density anomalies using a simplified relation between velocity and density (Birch's law), which assumes that all density changes are thermal in origin. That may not necessarily be true, as density and velocity changes may reflect compositional changes or the presence of partial melt, especially for shear velocity models, since the shear modulus decreases dramatically in the presence of partial melt and is more sensitive to changes in chemistry than is the bulk modulus. Therefore we do not expect perfect quantitative agreement between our simplified density heterogeneity model of the mantle and those inferred from seismic tomography.

We compute global correlation coefficients between our preferred slab model (with a velocity reduction factor $s = 4$ in the lower mantle) and both S12WM13 and SAW12D as shown in Figure 7a. Global correlations between the slab model and seismic tomography are defined as by *Ricard et al.* [1993]. The global correlation between our preferred slab model at all depths and seismic tomography is significantly lower than the correlation between the two tomographic models in most of the upper mantle and parts of the middle mantle for SAW12D, and at the very bottom of the mantle for S12WM13. It is similar, although lower, for most depths between 700 and 2300 km. However, correlation coefficients between 0.2 and 0.3 are extremely high, above the 95% confidence level, for all the spherical harmonic degrees we are considering. The statistical significance of the differences is difficult to assess because the number of degrees of freedom cannot be easily assessed. For each depth the total number of harmonic degrees and orders is at least 168. This value cannot be equated with the total number of degrees of freedom because (1) the depth resolution of the seismic models is less than that of the slab model and (2) the spectra of both fields are not flat [*Ricard et al.*, 1993]. The lowest correlations between our slab model and the seismic model are for depths above 400–500 km. This is easily understood, since the seismic models at these depths are sensitive to the structure of the oceanic and continental lithosphere, such as low-velocity zones near ridges and the high velocities under shields, which we have not included in our slab model. Low correlations at midmantle depths may reflect the poor resolution of tomographic models at those depths. A degree by degree correlation over the depth of the entire mantle for the first three harmonic degrees (Figure 7b) also reveals high correlations between the slab model and the seismic models for all depths except for the upper 400 km of the mantle. In general, our model is better correlated with SAW12D than with S12WM13.

We also compare the sensitivity of the correlation to the slowing factor s, defined in section 4.2. We find that in a global correlation over the entire lower mantle (Figure 8a), the highest correlation between our slab model and SAW12D occurs for a slowing factor of 4 and of 3.5 for model S12WM13. A degree by degree correlation over the entire lower mantle (Figure 8b) as a function of the slowing factor confirms that the highest correlations for the first three degrees are also for values of the slowing factor close to 4. The lower correlations for higher harmonic degrees may reflect a variety of problems, for example, the aliasing of high-frequency structure into low harmonic degrees in the tomographic models, subtleties in the position of the slabs in the mantle that reflect both the lack of horizontal advection in our model and uncertainties in the tectonic reconstructions, and the existence of a compositional contribution to the velocity anomalies.

We find that the radial variations in spectral amplitude of our field is comparable to that of the seismic models except in the upper mantle (Figure 9), where it is considerably lower. This we attribute to the lack of a deep lithospheric structure ("tectosphere") in both the

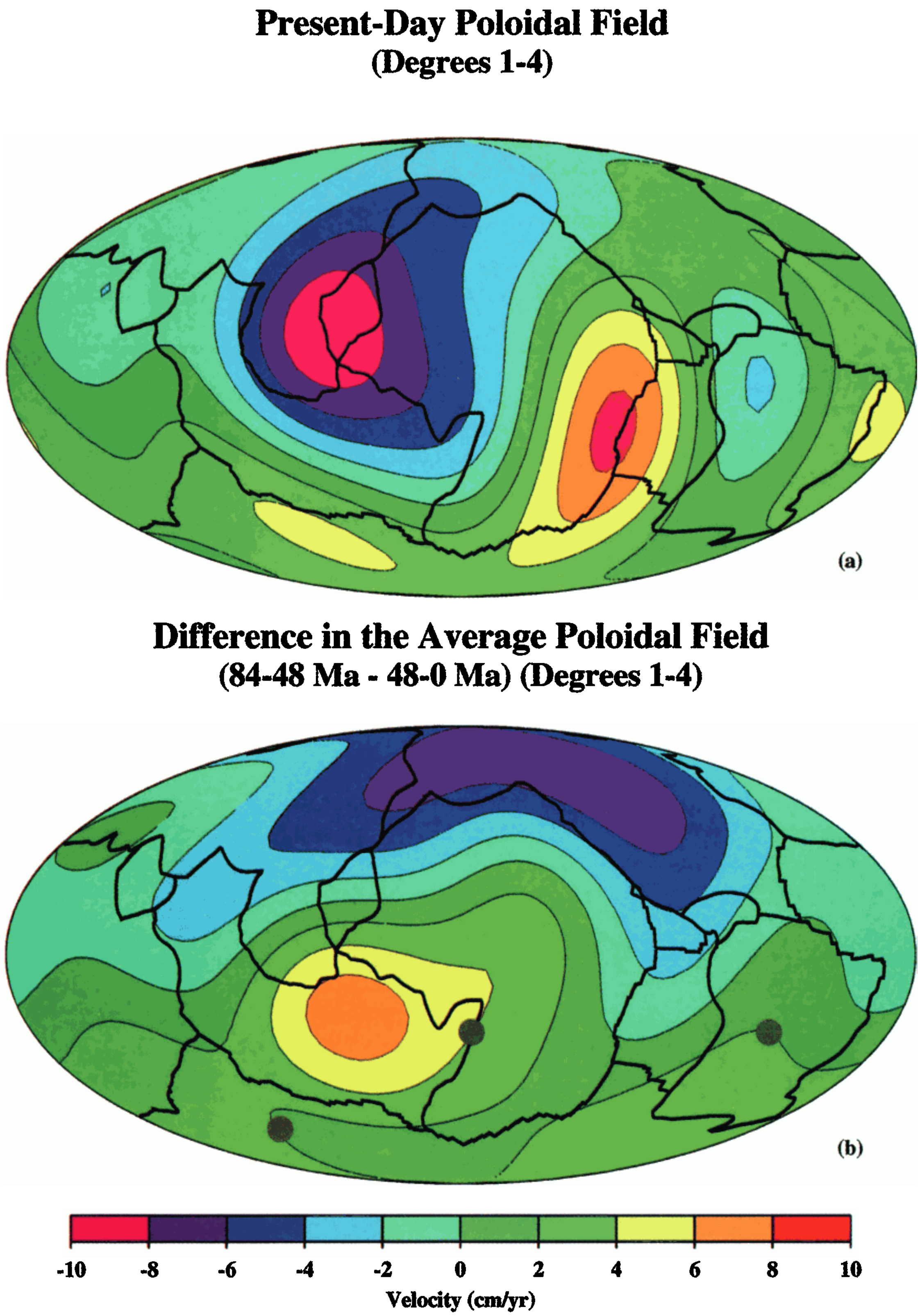

Plate 2. (a) Present-day long-wavelength (degrees 1–4) poloidal field in centimeters per year. Note that the positive poloidal field is concentrated in the southeastern Pacific and the negative field is concentrated in the northwestern Pacific in accord with present-day plate motions. (b) Spatial distribution of the long-wavelength (degrees 1–4) difference poloidal field obtained by subtracting the average field for 0–48 Ma from the average field for 48–84 Ma. Note that the strongest positive poloidal field is now concentrated over Australia, the southern Indian Ocean and the South Atlantic, coinciding with the reconstructed positions of the Ontong-Java and Kerguelen plateaus and the Paraná flood basalts. The approximate centers of the reconstructed positions of the plateaus are indicated by the gray circles.

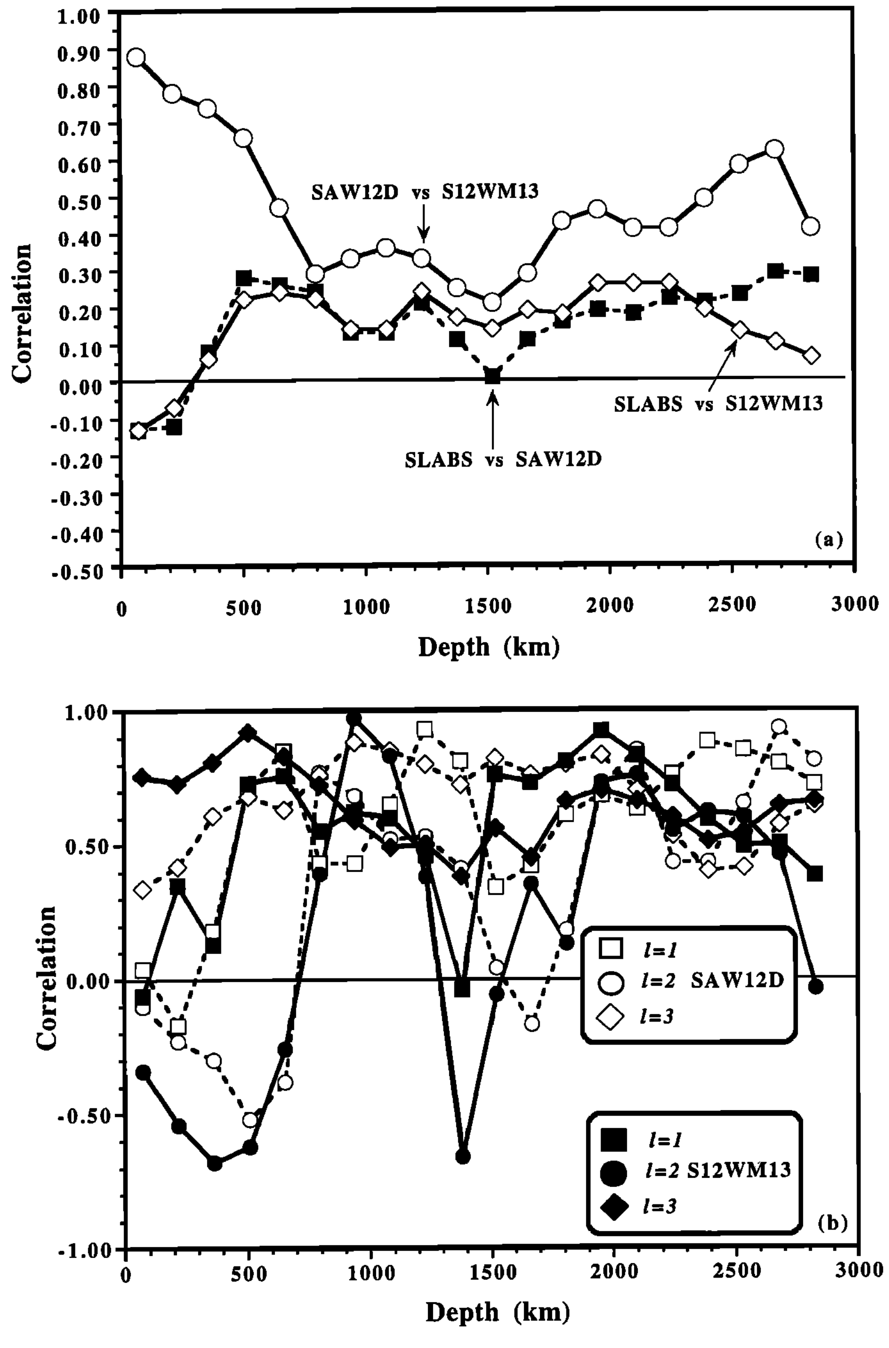

Figure 7. (a) Global correlation between the slab model and two seismic tomography inversions, SAW12D (solid squares and dashed line) [*Li and Romanowicz*, 1996] and S12WM13 (open rhombohedra and solid line) [*Su et al.*, 1994] as a function of depth. The slowing factor *s* is 4, and the correlation includes all 12 harmonic degrees. Also shown (open circles and solid line) is the global correlation between the two seismic models. (b) Degree by degree correlation, as a function of depth between the slab model and the two seismic models SAW12D (open symbols, dashed line) and S12WM13 (solid symbols, solid line), for degrees 1–3.

continents and oceans in the slab model used for this comparison. To convert the seismic velocities to density, we have used a velocity to density conversion factor of 0.2 g cm^{-3} km^{-1} s for the entire mantle.

Overall, our slab model based on the last 180 Myr of subduction compares well with seismic model SAW12D and not as favorably with S12WM13. Of the two seismic models, SAW12D yields larger variance reductions for the geoid (~78%) than S12WM13 (~50%), as well as for the divergence (~85%) and vorticity fields (~40%), almost a factor of 2 larger than for S12WM13 and much closer to the variance reduction obtained with the slab model. Despite the modest overall correlations, qualitatively there is agreement between the geodynamical significance of the slab model and the tomographic models. In general (Plate 3), areas of high seismic velocities in both models correspond to areas of past subduction, particularly under the Americas and Eurasia. Comparisons with higher-resolution tomographic models, such as those of *Grand* [1987, 1994] and more recently *Grand et al.* [1997] and *Van der Hilst et al.* [1997] reveal a qualitative agreement between the presence of slabs at depth and velocity anomalies in the lower mantle. A more quantitative comparison remains to be done, but some of the differences might be explained by using more realistic dip angles for subducted slabs.

4.5.2. The geoid. Using our mantle density heterogeneity model, we can use the method of *Richards and*

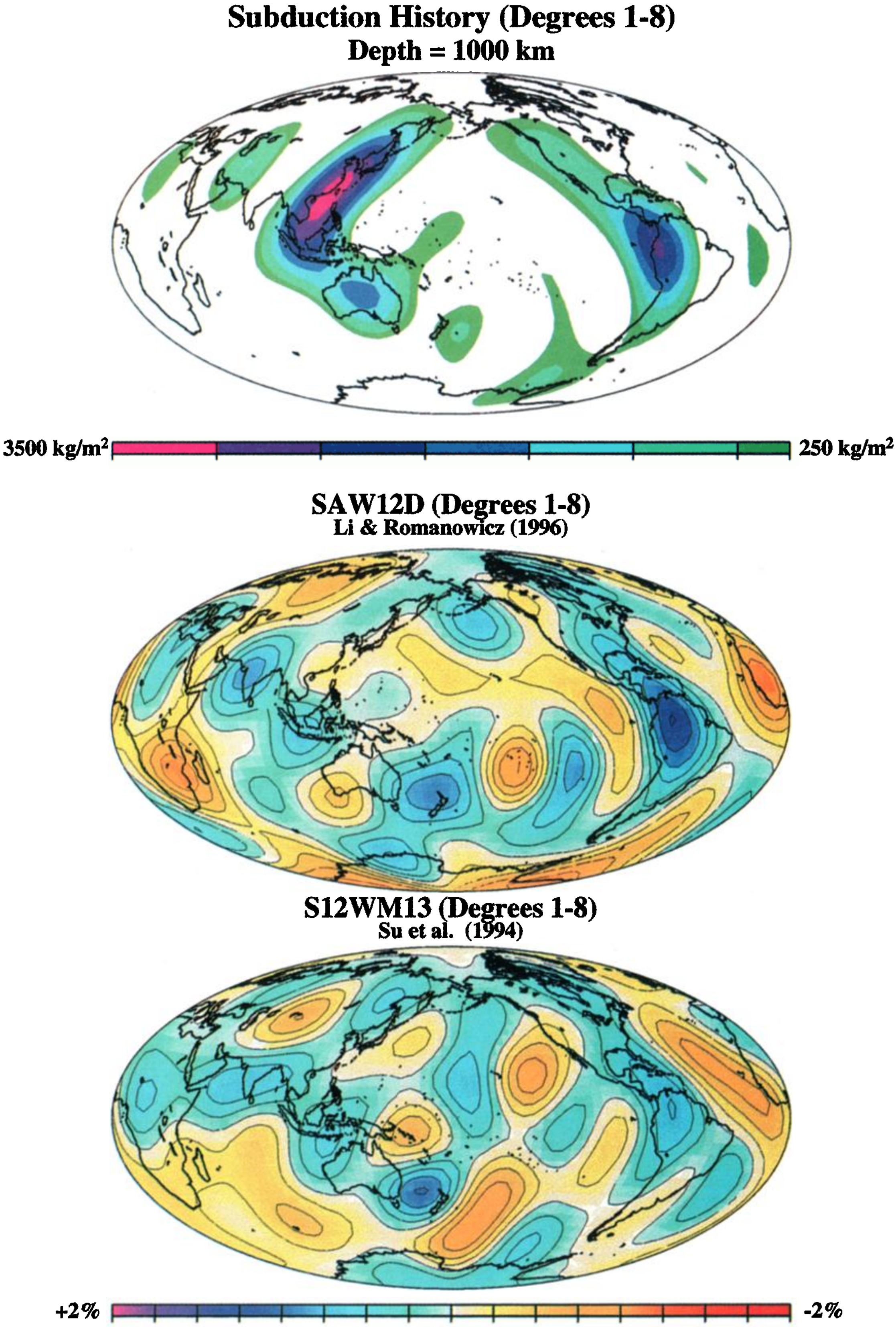

Plate 3. (top) Slab model reconstructed to degree 8 for a layer between 870 and 1015 km. (middle) Seismic tomography model SAW12D at 1000 km. (bottom) Model S12WM13 at the same depth and same spherical harmonic expansion.

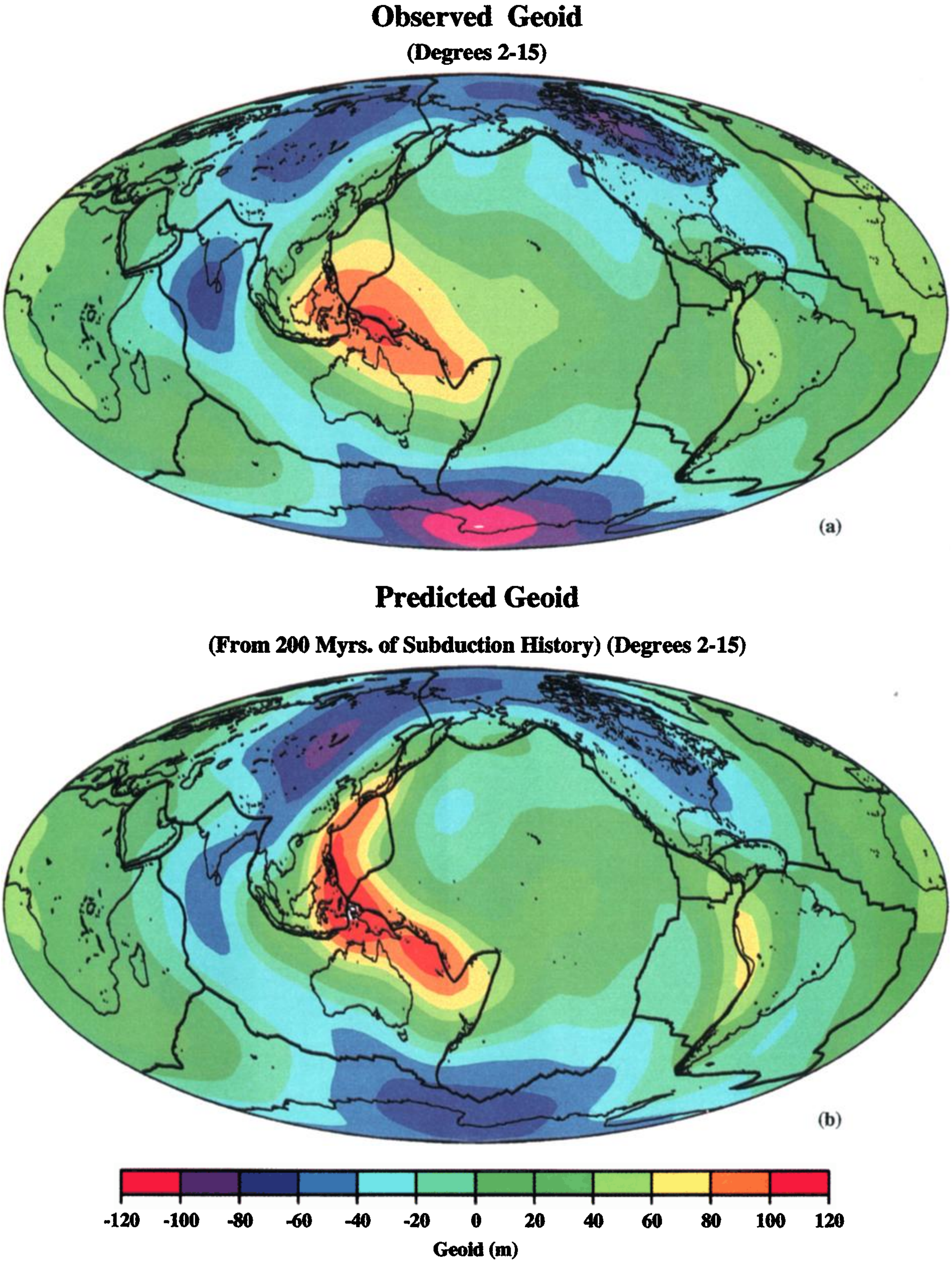

Plate 4. (a) Observed nonhydrostatic geoid and (b) synthetic geoid from 200 Myr of subduction history, using a slowing factor of 4 and the best fit viscosity structure described in Table 3. Degrees 2–15 are included.

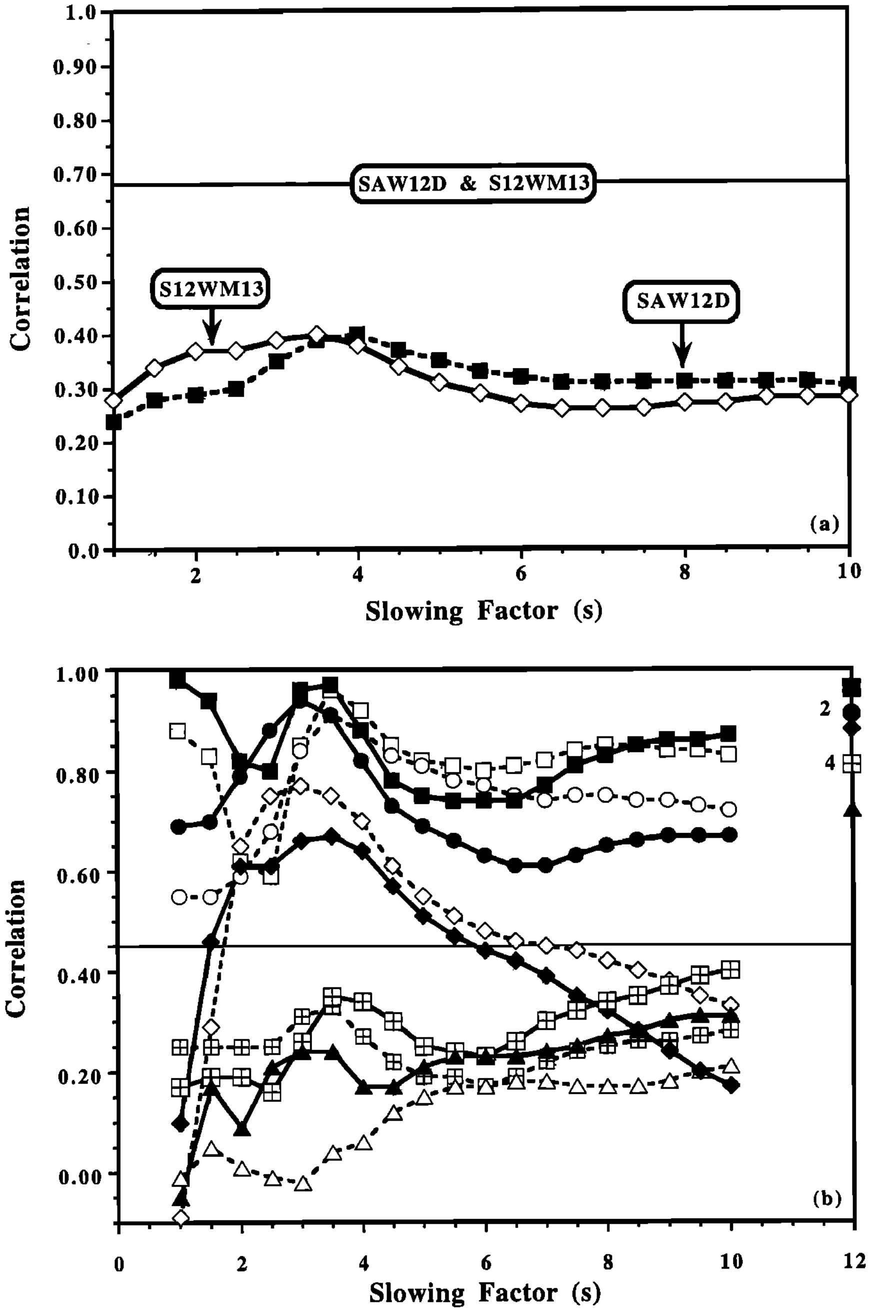

Figure 8. (a) Global correlation over the entire lower mantle between the slab model and SAW12D (solid squares, dashed line) and S12WM13 (open rhombohedra, solid line), as a function of the slowing factor s. The best correlations are obtained for a slowing factor of 3.5–4. The horizontal line marks the correlations between the two seismic models over the lower mantle. (b) Degree by degree correlations between the slab model and the seismic models SAW12D (open symbols and dashed lines) and S12WM13 (solid symbols and solid lines) for degrees 1–5, as a function of s. The correlation between the two seismic models is marked on the right-hand axis.

Hager [1984] to predict the geoid. The geoid is insensitive to the absolute viscosity of the mantle but very sensitive to relative changes in viscosity. The viscosity structure found to give the best fit to the geoid was determined by varying one of three free parameters (the viscosity contrast η^*_{Lit} between lithosphere and upper mantle, the viscosity contrast η^*_{LM} between lower and upper mantle, and the slab-slowing factor s) at a time. The results are shown in Figure 10 and tabulated in Table 3 with respect to an upper mantle reference viscosity of 10^{21} Pa s. We find that a lithosphere that is 10 times more viscous than the upper mantle, a lower mantle that is 50 times more viscous than the upper mantle, and a slowing factor of 4 yield the highest variance reduction. At first it may seem surprising that the lithosphere is less rigid than the lower mantle, but what this low lithospheric viscosity represents is an average over all plates and plate boundaries and thus, effectively, the fact that the lithosphere is mobile. The model does not distinguish between a ridge (a region of low viscosity) and the interior of a plate and therefore averages over areas with very different viscosities. It is also noteworthy that this viscosity structure is consistent with the slab-slowing factor s, since the logarithm of the lower to upper mantle viscosity ratio is ln (50) = 3.9; i.e., we expect that a viscosity contrast of about 50 will slow the sinking of slabs into the lower mantle by about a factor of 4 [*Gurnis and Davies*, 1986; *Richards*, 1991]. Finally, given that the geoid is the most sensitive measure of mantle viscosity structure, we define the viscosity

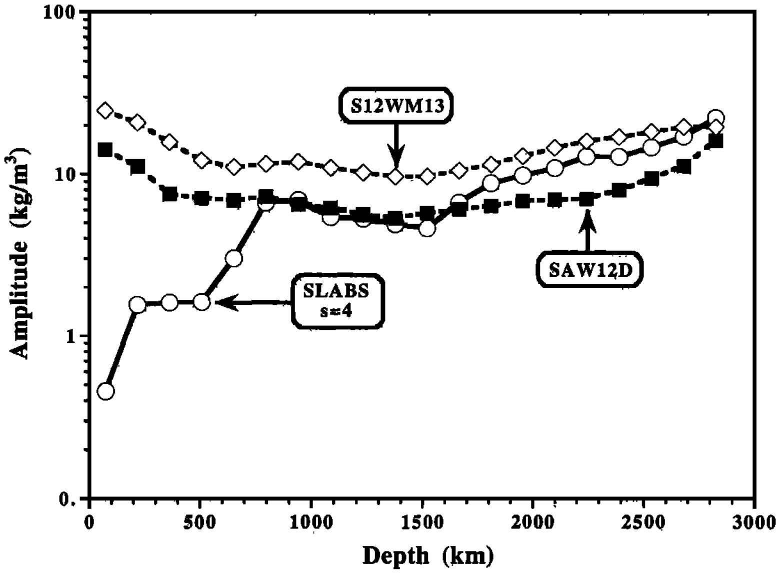

Figure 9. Spectral amplitude as a function of depth for slabs (open circles and solid lines), SAW12D (solid squares and dashed line), and S12WM13 (open rhombohedra and dashed line).

structure in the "best fit to geoid" column of Table 3 as our preferred model for all subsequent calculations.

With the best fit viscosity structure shown in Table 3, a slowing factor $s = 4$, and our mantle density heterogeneity field we obtain an excellent geoid model that yields an overall correlation with the observed nonhydrostatic geoid of 0.92 and a total variance reduction of 86%, larger than that for any previously published model of the geoid, including those based on seismic tomography, which typically achieve a variance reduction of the order of 50–60% [*Woodward et al.*, 1993]. The smaller variance reductions for the tomographic models are due mainly to the fact that these models invariably predict a C_{20} (Earth flattening) term of the geoid much smaller than is observed, while the slab model correctly predicts its amplitude. The only instances in which similar variance reductions are obtained using global seismic tomography are models where C_{20} is set to the observed value or the inversion is constrained to give the correct amplitude of the observed term [*Forte et al.*, 1994]. However, we note that the SAW12D model of *Li and Romanowicz* [1996] has a much stronger C_{20} term than previous seismic tomography models and that SAW12D yields only a slightly worse fit to the geoid than does our slab model.

The observed and synthetic geoid, including degrees 2–15, are shown in Plate 4. It is clear just from visual inspection that there is a high correlation between the observed and predicted fields. The agreement is very good out to degree 10 (Figure 11a), and the total amplitude for each degree is well matched, although slightly overpredicted for degrees higher than 3 (Figure 11b).

Our preferred viscosity structure is in full agreement with previous studies [e.g., *Hager et al.*, 1985; *King and Masters*, 1992; *Forte and Mitrovica*, 1996; *Mitrovica and Forte*, 1997]. Our preferred viscosity structure also has dynamical justification [*Davies and Richards*, 1992; *Ricard et al.*, 1993]: a lower mantle with a higher viscosity reduces the magnitude of the mantle return flow induced by plate motions [*Richards*, 1991], as well as the vigor of convective velocities, therefore deflecting little a deep-seated mantle plume. In other words, a mantle with a very viscous lower mantle provides a relatively fixed hotspot reference frame. Furthermore, such a mantle would retain through-going slabs longer and thus explain the agreement between the location of past subduction and lower mantle heterogeneity as observed with tomography and other seismic studies [*Grand*, 1987, 1994; *Richards and Engebretson*, 1992; *Ricard et al.*, 1993].

4.5.3. Dynamic topography. Dynamic topography is defined as the topography maintained by dynamical processes, that is, the elevation of a boundary surface due to the upwellings and downwellings of the flow induced by density anomalies in the mantle. Keeping track of this dynamically generated uplift or subsidence is extremely important when computing geoid anomalies due to internal sources.

The present-day observed pattern of dynamic topography is hard to measure. *Cazenave et al.* [1989] have suggested a pattern that follows that of the geoid, but *Colin and Fleitout* [1990] claim that the amplitude of

TABLE 3. Viscosity Structure Models

Depth, km	*Best Fit to Geoid*	*LVC ~300 km Thick*	*LVC ~70 km Thick*	*Hager and O'Connell [1981]*
0–64	···	···	1×10^{21}	
0–130	1×10^{22}	1×10^{22}	1×10^{22}	···
64–128	···	···	1×10^{19}	
130–200	1×10^{21}	1×10^{19}	1×10^{19}	···
128–410	···	···	1×10^{21}	
200–410	1×10^{21}	1×10^{19}	1×10^{21}	···
410–670	1×10^{21}	1×10^{21}	1×10^{21}	1×10^{21}
670–2890	5×10^{22}	5×10^{22}	5×10^{22}	1×10^{21}

LVC, low-viscosity channel.

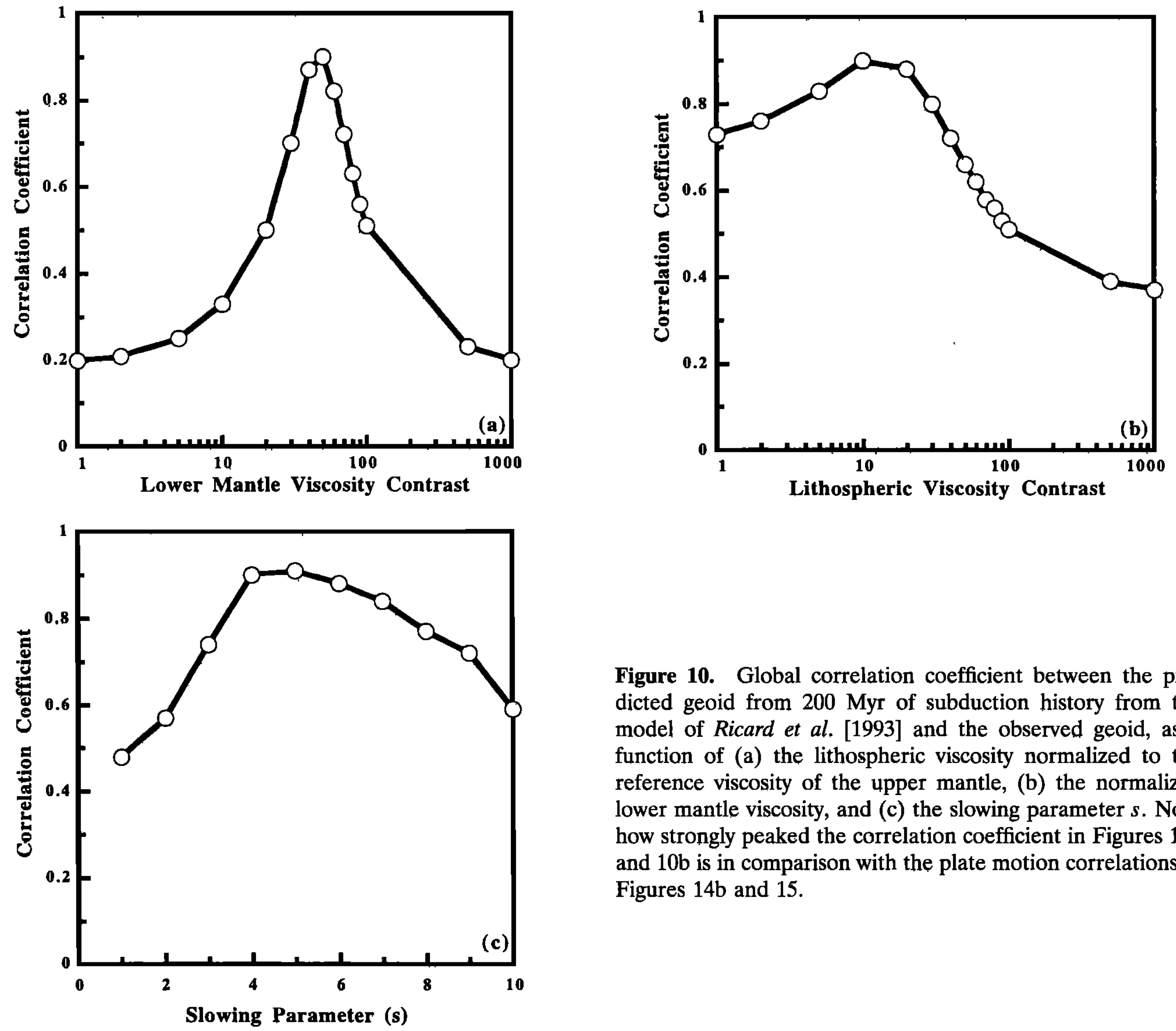

Figure 10. Global correlation coefficient between the predicted geoid from 200 Myr of subduction history from the model of *Ricard et al.* [1993] and the observed geoid, as a function of (a) the lithospheric viscosity normalized to the reference viscosity of the upper mantle, (b) the normalized lower mantle viscosity, and (c) the slowing parameter s. Note how strongly peaked the correlation coefficient in Figures 10a and 10b is in comparison with the plate motion correlations in Figures 14b and 15.

dynamic topography is zero. The difficulty lies in that to compute all the dynamic topography, we must know the density structure of the crust and lithosphere accurately [*LeStunff and Ricard*, 1995].

Here, we restrict ourselves to calculating the dynamic topography induced by the slabs alone, and we do not consider near surface contributions. *Ricard et al.* [1993] have shown that the pattern of dynamic topography deduced from our slab model follows the subduction zones (new and old) around the Pacific. This pattern (Plate 5a) is easily calculated from our model. The dynamic topography is calculated by dividing the radial stresses from the flow model by the gravitational acceleration and a density contrast of 2500 kg m^{-3}, which is appropriate for the water-ocean floor interface. The amplitudes predicted by our model are rather large, as for models based on seismic tomography [*Forte et al.*, 1993b]. Several recent efforts have suggested that the amplitude of total dynamic topography can be reduced by a factor of 2–3 by either allowing part of the topography to develop at 670 km [*Thoraval et al.*, 1995] or taking into account thermodynamic effects of the phase change [*Christensen*, 1998; *LeStunff and Ricard*, 1997].

An intriguing result from our model is the prediction of dynamic uplift of continents due to the cessation of subduction. In our model, when subduction stops and the old slabs sink into the mantle, the overlying plate rebounds and uplifts, in the same way as the mechanism proposed by *Mitrovica et al.* [1989] for producing tilting of continents by changes in subduction geometry. If we look at the dynamic topography predicted by our model at two times in the past, before the disappearance of the Kula plate (56 Ma) and right after (43 Ma) (Plates 5b and 5c), and (perhaps more interestingly) at the cumulative difference in dynamic topography from 43 Ma to the present (Plate 6), we see that by far the largest change has occurred over the North American continent, with uplift centered over what is now Alaska and northeastern Siberia. This uplift is the direct result of the disappearance of the Kula plate at 48 Ma and the cessation of subduction and the subsequent consumption of the Farallon plate under western North America

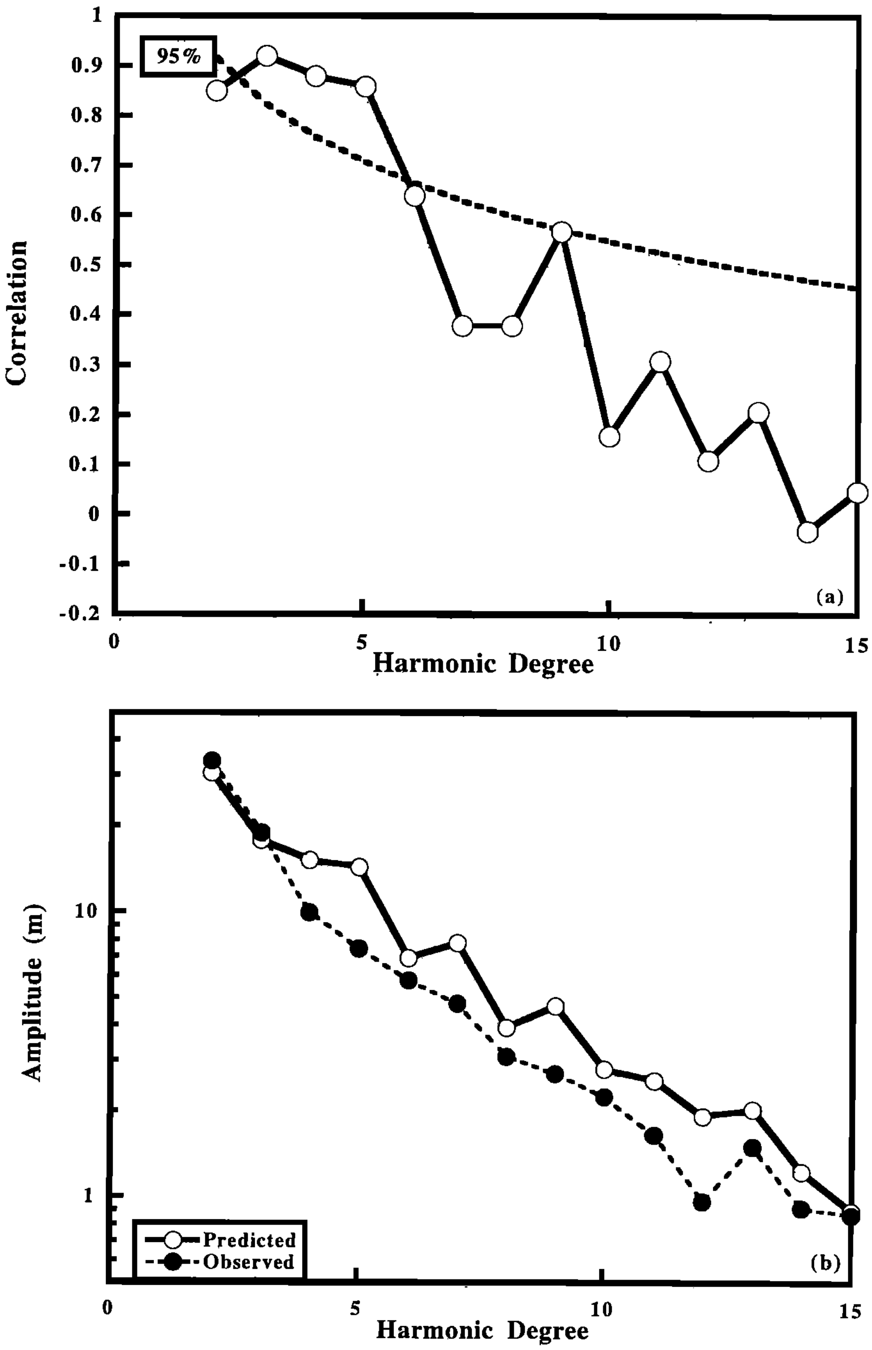

Figure 11. (a) Degree by degree correlation of the predicted and observed geoid along with 95% confidence level. The correlations are high up to degree 9. (b) Amplitude of observed (solid circles and dashed line) and predicted (open circles and solid line) geoid. The amplitudes we predict are consistently higher than the observed, except for the low degrees (2–3).

(which extends the focus of uplift southward). In fact, a map of present-day topography shows that these regions are anomalously elevated given their crustal thickness, consistent with the analysis of *Mitrovica et al.* [1989]. The predicted (modeled) subsidence in the western Pacific (Plate 6) is directly related to the change in convergence between the Eurasian and Pacific plates and the migration of the subduction zone between 25 Ma and the present day.

5. PLATE MOTION MODELS

5.1. Correlations and Uncertainties

We assess the success of our models quantitatively by computing the global correlation coefficients between the predicted and observed Cartesian components of the linear velocities of each plate integrated over the surface area of the plate (linear momenta). The linear momenta are given by

$$v_{ij} = \frac{\iint (\boldsymbol{\omega}_j \times \mathbf{r}_j)_i \, dA}{A_j} \tag{17}$$

where $i = x, y, z$ labels the three Cartesian components of the linear velocity and j is the index of the plate; $\boldsymbol{\omega}_j$ is the Euler rotation vector, $\mathbf{r}_j$ is the position vector for any point on the plate, and A_j is the area of plate j.

We compute both weighted and unweighted linear

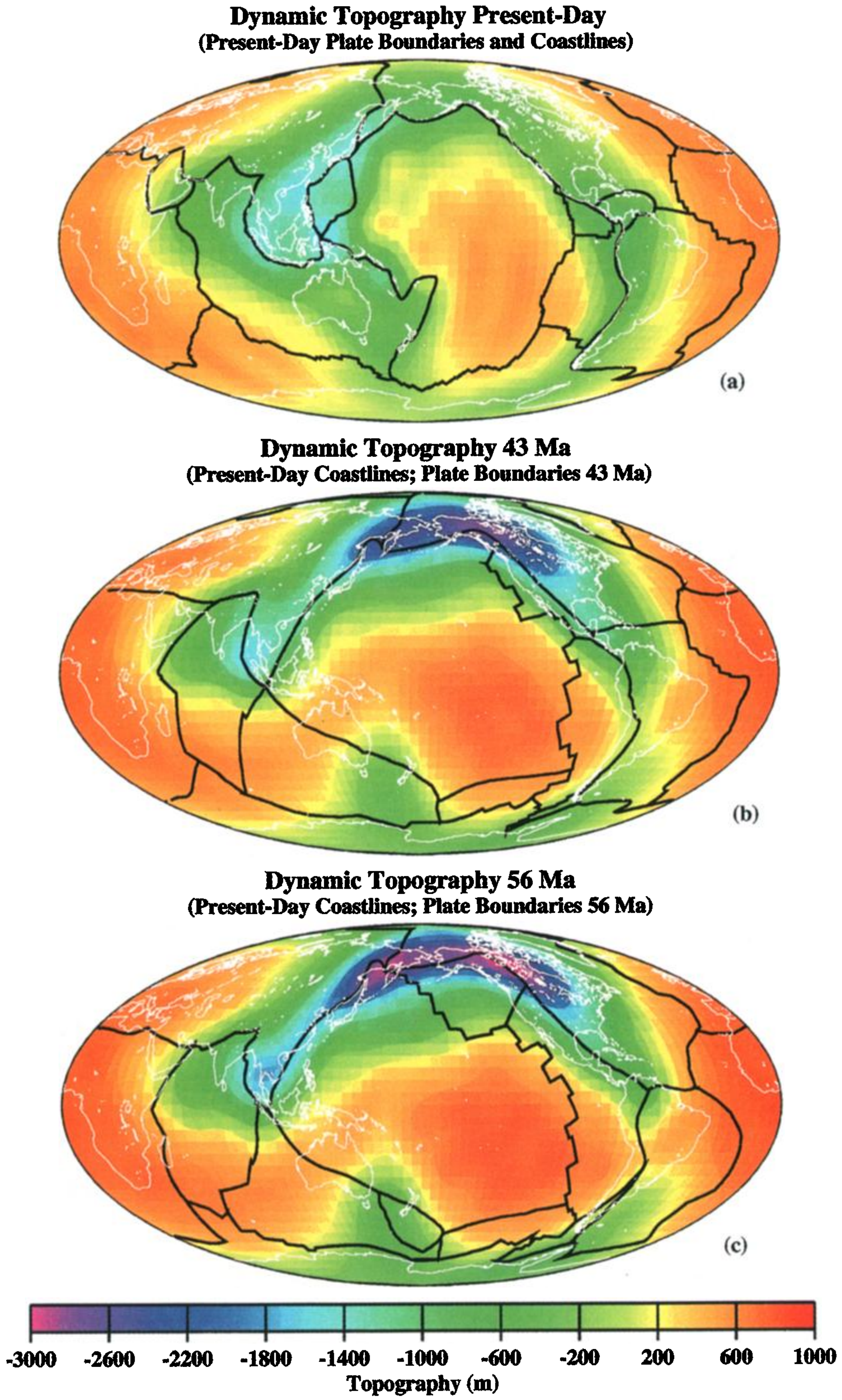

Dynamic Topography Present-Day
(Present-Day Plate Boundaries and Coastlines)

Dynamic Topography 43 Ma
(Present-Day Coastlines; Plate Boundaries 43 Ma)

Dynamic Topography 56 Ma
(Present-Day Coastlines; Plate Boundaries 56 Ma)

Plate 5. (a) Present-day, (b) 43 Ma, and (c) 56 Ma dynamic topography based on our slab model for harmonic degrees 1–15.

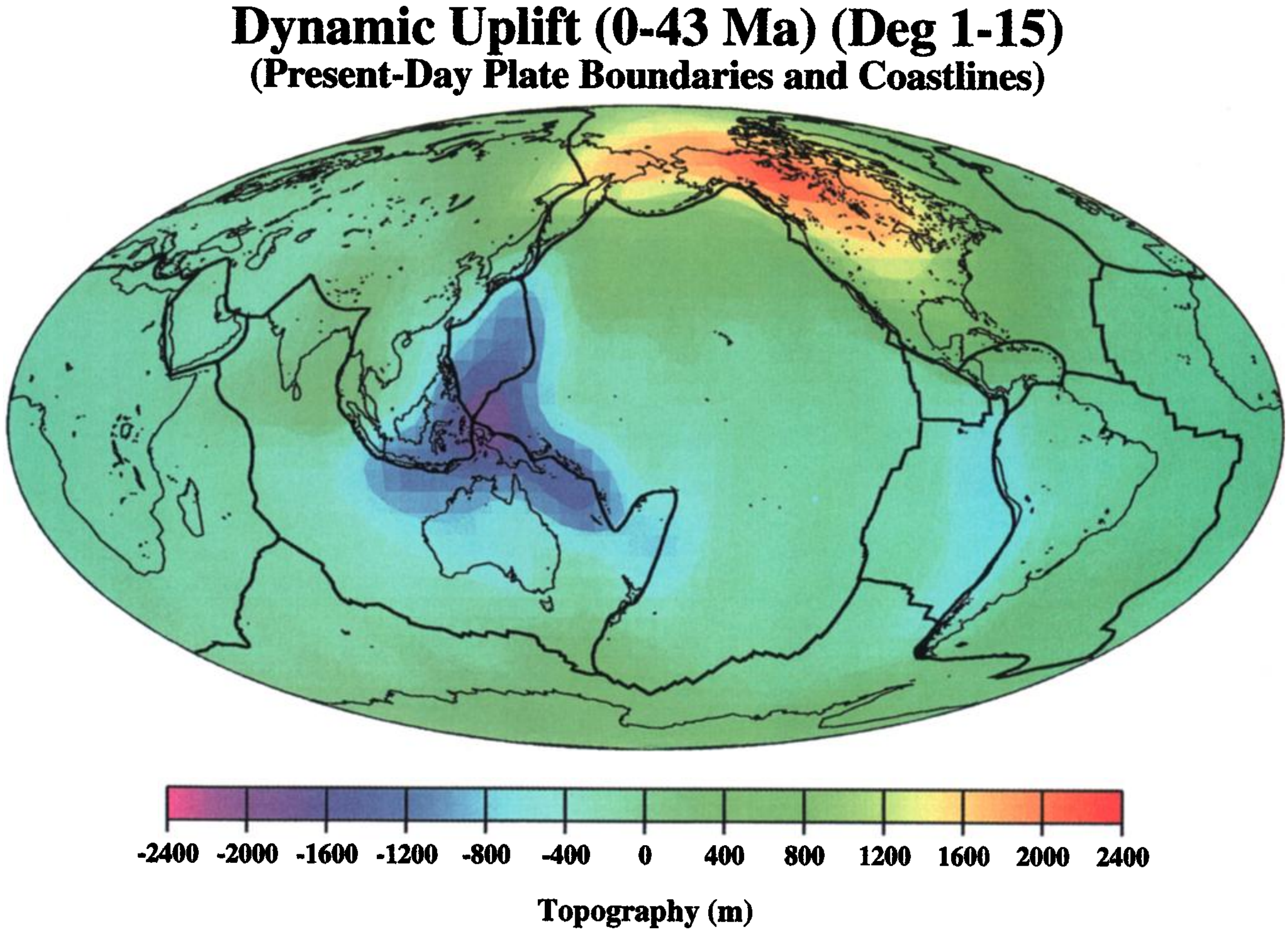

Plate 6. Differential dynamic topography, in meters, for the last 43 Myr.

correlation coefficients (R, R_{un}) between observed and predicted velocity components. For the former we weight the v_{ij} by the fraction of the total surface area of the Earth that each plate occupies. This is equivalent to a point by point correlation of the observed and predicted velocities over the entire surface of the Earth.

For each plate configuration consisting of N plates there are $3N$ degrees of freedom, which correspond to three Cartesian components of the rotation vector of each plate. For $N = 12$ the correlations are significant above the 95% confidence level for any correlation coefficient (R or R_{un}) greater than 0.33. For any variation in the input data and parameter set the significance level (sig) of the difference in the resulting correlation coefficients is given by Fisher's Z transformation, which associates a corresponding Z to each measured R_x [*Press et al.*, 1992] by

$$Z = \frac{1}{2} \ln \left(\frac{1 + R_x}{1 - R_x} \right) \tag{18a}$$

$$\mathrm{sig} = \mathrm{erfc} \left(\Delta Z \, \frac{\sqrt{N - 3}}{2} \right) \tag{18b}$$

where R_x is the weighted or unweighted correlation coefficient and ΔZ is the absolute difference in Fisher's Z for the two R_x. For $N = 12$, ΔZ must be ≥ 0.45 for the correlation coefficients to differ at the 95% confidence level. For a set of input data and parameters yielding a correlation coefficient $R_x = 0.80$ to be significantly better or worse, at the 95% level, than another set, the other set must yield $R_x \geq 0.91$ or $R_x \leq 0.57$, respectively.

We compare our models with the observed components of the plate velocities, which result from subtracting the net rotation of the lithosphere with respect to the mantle from the hotspot reference frame poles of rotation of *Gordon and Jurdy* [1986]. The correlation coefficient measures to what degree plate motions at the end of a plate stage, are consistent with the subducted buoyancy forces introduced prior to the end of that stage.

In recent geodynamic modeling efforts [e.g., *Woodward et al.*, 1993; *Forte et al.*, 1993a; *Ricard and Vigny*, 1989] the total variance reduction between the observed and predicted poloidal and toroidal fields has been used as the measure of the quality of fit. The power spectrum of these fields decays as l^{-2}, so that most of the power is contained in the low degrees (1–4). Given that all models of internal density heterogeneity reproduce the long-wavelength character of the velocity field adequately, it is not surprising to achieve very large variance reductions (for our model, no less than 98–99%). However, these high values are not meaningful in this context,

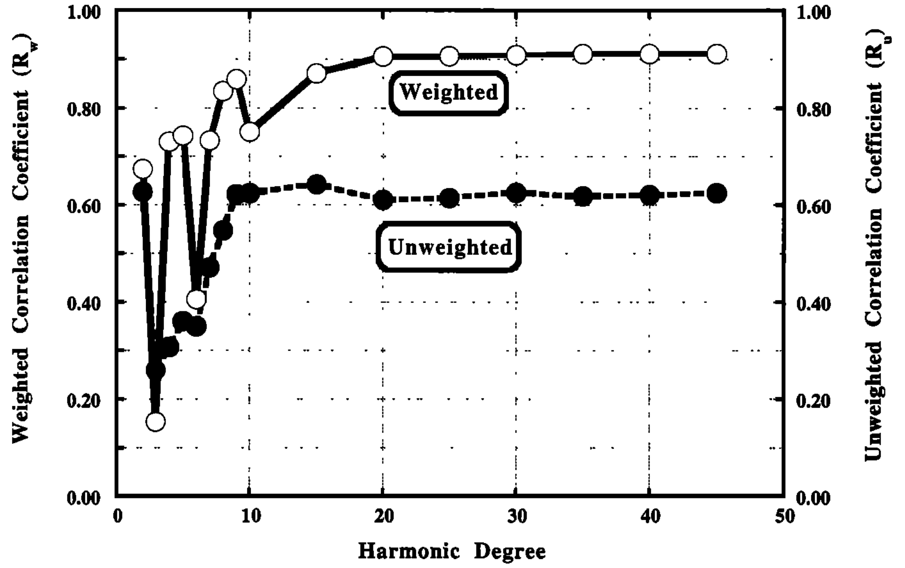

Figure 12. Weighted (open circles and solid line) and unweighted (solid circles and dashed line) global correlation coefficients between observed and predicted linear velocity components as a function of the harmonic degree to which the torque integration is performed. The series is well converged by degree 20 for both weighted and unweighted correlation coefficients.

since the overall quality of the fit should be determined by how well it reproduces the surface velocity field itself. Poor fits to degrees higher than 4 are in the noise using this metric. The only plate with dimension of comparable order is the Pacific plate, whereas the length scale of the smaller plates corresponds to degrees higher than $l = 10$.

Using uncertainties in plate rotation poles and angular velocities, we can derive 1σ bounds on the computed correlation coefficients between observed and predicted plate motions. Assuming normally distributed errors, the chi-square (χ^2) statistic can be related to the correlation coefficient R_x [*Press et al.*, 1992]:

$$\chi^2 = (1 - R_x^2) \sum_i^{3N} \frac{(v_{oi} - \bar{v}_o)^2}{\Delta_i^2} \qquad (19)$$

where v_{oi} are the observed linear velocities, $\bar{v}_o$ is the observed average linear velocity, and the Δ_i^2 are the estimates of the error obtained from propagating the uncertainties in the poles of rotation and angular velocities of the plates compiled by *Lithgow-Bertelloni et al.* [1993]. At the 1σ level, $\Delta\chi^2 = 1$, and the errors in the correlation coefficient are given by

$$dR_x = \left(2R_x \sum_i^{3N} \frac{(v_{oi} - \bar{v}_o)^2}{\Delta_i^2}\right)^{-1} \qquad (20)$$

5.2. Model Resolution

A number of parameters affect, to a larger or lesser extent, the outcome of our calculations: the maximum harmonic degree for the torque integration ($l_{\max}$), the absolute viscosity of the upper mantle (η_0'), the viscosity contrast between the lower and upper mantle (η_{LM}^*), the contrast between the lithospheric and upper mantle viscosities (η_{Lit}^*), and the slowness factor s by which the terminal velocity of the slabs is reduced as slabs enter the lower mantle.

The best fitting parameters are determined by requiring our model to yield the best fit to both the observed geoid and the present-day plate velocities. Although we show in detail the effect of all the parameters on our results, the final calculations presented here have only one free parameter, the absolute viscosity of the upper mantle, upon which the speed of the plates depends. In the following sections we present the effect of varying all of the aforementioned parameters on the correlation between our model and the observed present-day plate velocity field.

5.2.1. Convergence. The convergence of weighted and unweighted correlation coefficients with respect to the maximum number of harmonic degrees $l_{\max}$ is shown in Figure 12. By degree 20 the values are well converged for both the weighted and unweighted correlation coefficients. Most of the information needed to model plate motions is contained in degrees 2–9, which also encompass the primary signature of slabs in geoid modeling [*Hager*, 1984].

Given that for the weighted correlation coefficient the velocity components are weighted by the plate area, the quality of the fit is most sensitive to the largest plates, in this case the Pacific and Eurasian plates. Pacific plate motion can be accurately modeled even truncating the series at degree 4 (its characteristic wavelength). For degrees lower than 10 the **M** matrix is ill conditioned even after the three eigenvalues corresponding to the arbitrary net rotation have been eliminated. Long-wavelength density fields lead to very small torques on many of the smaller plates. The number of these torques that will fall below the numerical precision varies rapidly with degree for $l < 10$ (23 for degree 2), causing the large oscillations shown in Figure 12. On the basis of these

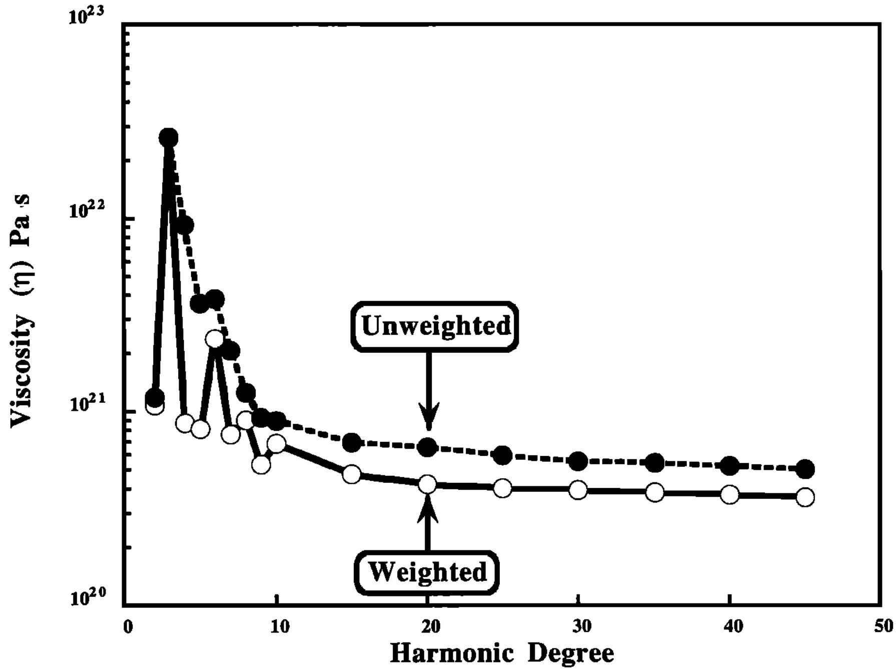

Figure 13. Best fit absolute viscosity as a function of harmonic degree, obtained by minimizing the weighted or unweighted χ^2 statistics. Symbols are the same as in Figure 12. The values are well converged by degree 20.

convergence results, we truncated the torque integration at degree 20 for all models, past and present.

5.2.2. Absolute viscosity. As was stated before, the absolute viscosity does not affect the geoid signal, but it is inversely proportional to the magnitude of the plate rotation vector. Using a starting reference viscosity for the upper mantle of 10^{21} Pa s, we optimize the absolute upper mantle viscosity for all sets of input data and parameters, by minimizing the chi-square statistic between predicted and observed plate velocities.

The reference absolute viscosity η_0 affects only the magnitude of the plate rotation vectors and not their direction; plate velocities scale linearly with η_0^{-1}. The absolute upper mantle viscosity does not affect the value of the correlation coefficient but affects only the slope of the regression line. We can then write the inverse relation between plate velocities and reference absolute viscosity as $v'_{p_i} = a v_{p_i}$, where the v_{p_i} are the predicted velocities optimized with respect to η'_0 and $a = \eta_0/\eta'_0$. To find η'_0, we minimize the chi-square statistic

$$\chi^2 = \sum_i^{3N} \frac{(a v_{p_i} - v_{o_i})^2}{\Delta_i^2} \tag{21}$$

with respect to a. Setting $\partial\chi^2/\partial a = 0$, we obtain

$$\eta'_0 = \eta_0 \frac{v_{p_i}^2}{\sum_i v_{p_i} v_{o_i}}. \tag{22}$$

The second derivative of (22) with respect to a yields the uncertainty in the $\log_e$ of the best fit viscosity $d \ln (\eta'_0) = da/a$ in terms of the errors in the observed plate rotation vectors through

$$\mathrm{VAR}(a) = \frac{\Delta\chi^2}{\sum_i^{3N} (v_{o_i}^2/\Delta_i^2)} \tag{23}$$

where $\Delta\chi^2$ is 1 for 1σ and 4 for 2σ uncertainties.

The convergence of the best fit absolute viscosity with respect to the maximum harmonic degree maintained in the model, $l_{\max}$, keeping the relative viscosity structure determined from the geoid modeling (Table 3, best fit) fixed, is shown in Figure 13. The value of the viscosity obtained with both the weighted and unweighted χ^2 minimizations decreases with harmonic degree and settles down to a value between 4 and 6 × 10^{20} Pa s for degree 20. As the maximum harmonic degree increases, the value of the absolute viscosity continues to decrease as $1/\eta \sim \ln(l)$. This decrease is due to the stress singularity in viscous flow models with infinitely thin rigid shells previously discussed (see section 2.4). Discontinuities in velocity (such as those occurring at plate boundaries) generate singularities in the basal shear stresses. This in turn leads to divergent torques, which increase with increasing harmonic degree. We reference the absolute viscosity and all other quantities in our model to $l = 20$, at which point the effects of the input data and model parameters are exhausted.

5.2.3. Viscosity structure. The viscosity contrasts between the upper and lower mantle and between the lithosphere and upper mantle affect the direction of plate motions and the magnitude of the best fit absolute viscosity. The latter is affected because, for example, a more viscous lower mantle exerts more resistance to plate motions and therefore lowers the value of the predicted plate speeds, which requires a lower absolute

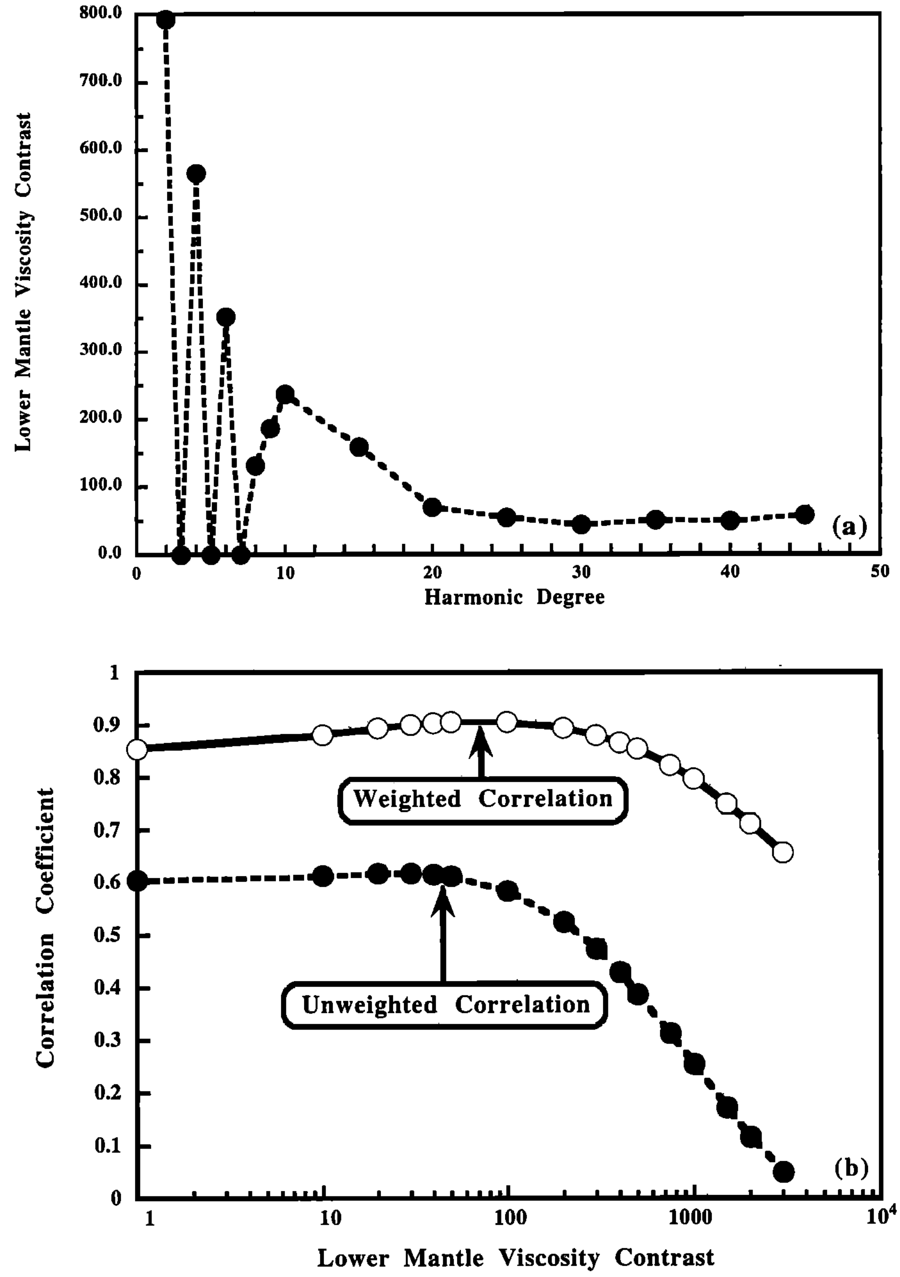

Figure 14. (a) Best fit lower mantle viscosity contrast as a function of harmonic degree. The optimum values were obtained using Brent's method [*Press et al.*, 1992]. A stable value for the viscosity contrast is not reached until degree 20, suggesting that the information contained at this frequency is essential for modeling the viscosity structure of the Earth as well as the plate velocity field. (b) Weighted and unweighted correlation coefficients (symbols are the same as in Figure 12) between observed and predicted plate motions as a function of the normalized lower mantle viscosity. The broader peaks for the weighted values are probably due to the fact that this coefficient responds mostly to the Pacific plate, whose direction of motion (although not its speed) is largely unaffected by a more viscous lower mantle.

viscosity to match the magnitude of the observed velocities. Directions are affected because upper and lower mantle density heterogeneity will, in general, tend to drive plates in different directions. Since the driving forces are mediated by induced flow, a change in the relative viscosity of the two layers will alter both the plate speeds and directions.

The effects that variations in viscosity contrasts have on the quality of the fit are investigated by varying only one parameter at a time. First we look at the effects of the harmonic degree truncation on the best fit viscosity contrast between upper and lower mantle. Then we look at the effects of higher viscosities in the lithosphere and lower mantle on predicted plate velocities.

We find the best fit value for the viscosity contrasts by minimizing the unweighted χ^2 statistic using Brent's method [*Press et al.*, 1992]. Figure 14a shows that the best fit η^*_{LM} converges by degree 20 and varies only by a factor of ~1.5 between degree 20 (~69) and degree 45 (~54), a variation not resolvable in our models. However, it is important to note that before degree 20 the value of the best fit viscosity contrast between the upper and lower mantle is highly variable. This suggests that determinations of the viscosity structure with mantle models that include at most structure of the order of l = 12 are unreliable. In particular, determinations of mantle viscosity with plate motion models derived from low degree ($l \leq 12$) seismic structure are suspect.

Keeping l_{max} and η^*_{Lit} fixed, we look at the variation of the correlation coefficient as a function of η^*_{LM} in Figure 14b. Both the unweighted and weighted correlation coefficients increase slowly with increasing lower mantle

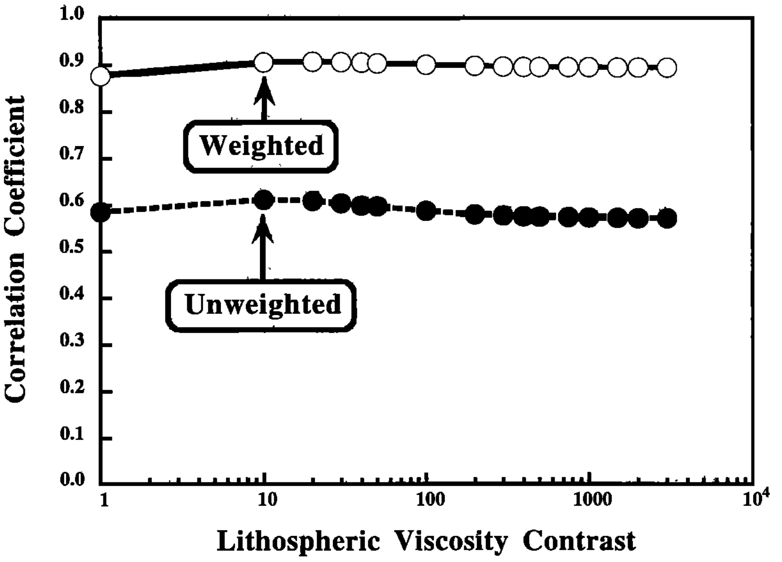

Figure 15. Weighted and unweighted correlation coefficients as a function of the normalized lithospheric viscosity. A stronger lithosphere has little effect on the direction of plate motions but has a strong effect on their speed (Figure 20).

viscosity contrast and then decrease. Both peaks are very broad, spanning ~1–1.5 orders of magnitude in viscosity. The differences among the correlation coefficients in the peak are all well below the 95% confidence level. The best fit is found for values between 40–70, in good agreement with our geoid modeling (Figure 9b). The peak of the weighted correlation coefficient is much broader because the contrast of viscosity between the upper and lower mantle does not significantly affect the velocity of the Pacific plate, which contributes most to the correlation coefficient because of its size. The direction of the Pacific plate is determined by the slabs in the upper mantle; however, its speed, which does not affect the correlation coefficient, is affected to a greater extent by the lower mantle slabs.

Keeping l_{max} and η^*_{LM} fixed, we investigate the effects of lithospheric viscosity on the global correlation between predicted and observed plate velocities and show the results in Figure 15. For both weighted and unweighted values the correlation increases slightly with increasing lithospheric viscosity. However, the effect is negligible, and the differences among correlations coefficient are again well below the 95% confidence level. The peak occurs at a contrast between lithospheric and upper mantle viscosity of 10, again similar to that found in geoid modeling.

Comparing our results in Figures 14 and 15 with Figure 10, it is clear that the mantle viscosity structure determined from the plate motion modeling is consistent with that derived from modeling the present-day

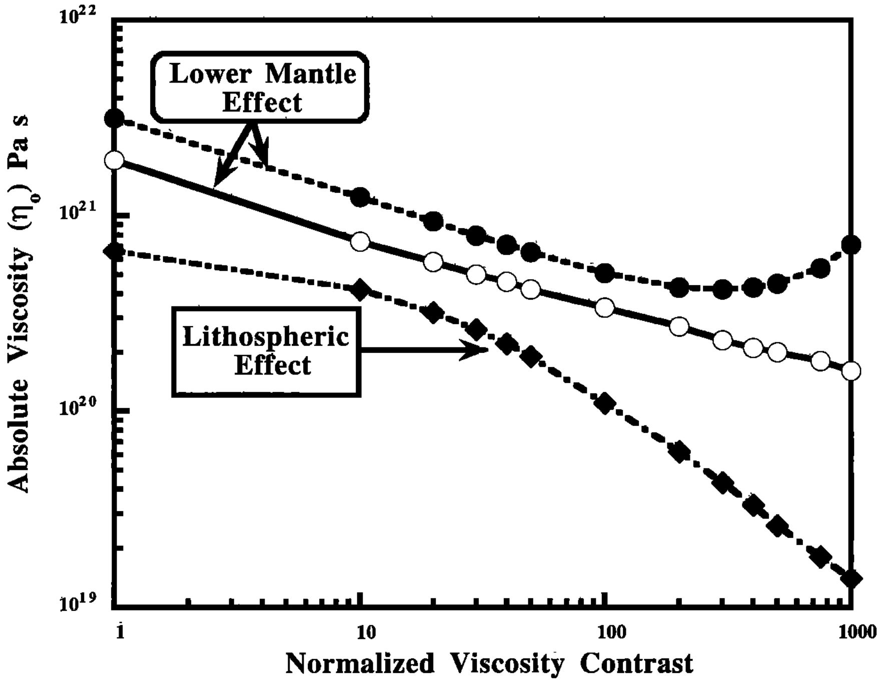

Figure 16. Effects of increasing the lower mantle (weighted, open circles and solid line; unweighted, solid circles and dashed line) and lithospheric viscosities (solid rhombohedra and dotted-dashed line) on the best fit absolute viscosity. Increasing either viscosity contrasts tends to decrease the plate velocities and therefore decrease the valued of the absolute viscosity needed to match observed plate speeds.

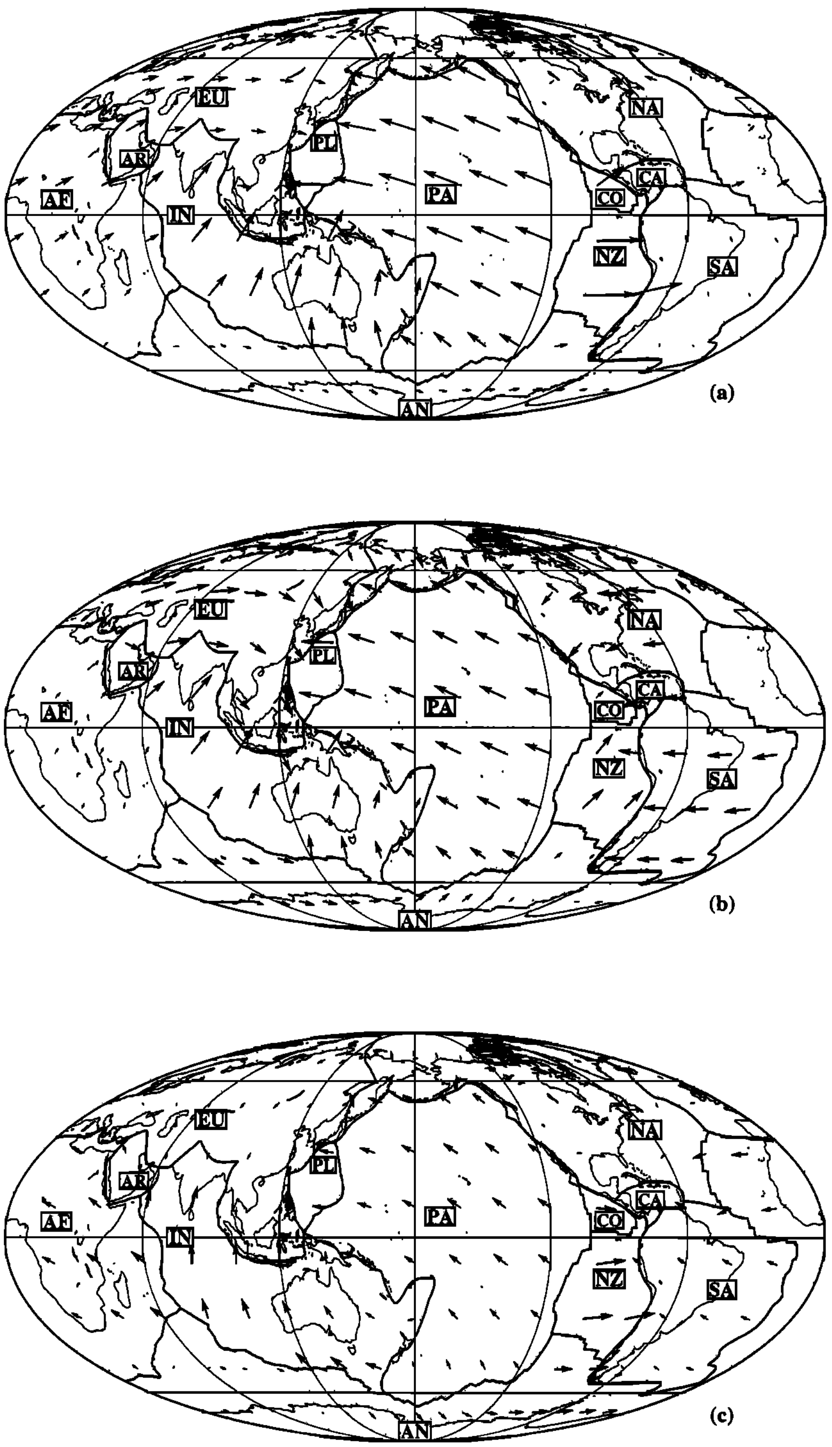

Figure 17. (a) Observed velocities in the no-net-rotation reference frame for 0–10 Ma (explained in the text), (b) predicted velocities using our mantle heterogeneity model based on 200 Myr of subduction and the best fit viscosity structure of Table 3, and (c) predicted velocities using tomographic model SH425.2. Arrows, plate boundaries, continental outlines, and plate codes are as described in Figure 2.

geoid (Table 3, best fit). However, the geoid is a more sensitive measure of viscosity structure than plate velocities and we are thus justified in defining our preferred model of the viscosity structured based only on the fits to the present-day geoid.

The lithospheric viscosity contrast has a strong effect on the best fit absolute viscosity, and using the constraints from postglacial rebound, we can assign an upper bound to the value of this viscosity contrast. Estimates of mantle viscosity from postglacial uplift and far-field relative sea level variations are uncertain but can constrain the absolute lower bound of upper mantle viscosities to 3.7–4.5 × 10^{20} Pa s [*Mitrovica and Peltier*, 1993] for the former and 1–2 × 10^{20} Pa s [*Nakada and Lambeck*, 1987, 1989] for the latter, in the absence of a low-viscosity channel. If a weak asthenosphere is present, the lowest allowed value of the upper mantle viscosity below the low-viscosity channel is ~10^{21} Pa s [*Körnig and Müller*, 1989]. Figure 16 shows that absolute upper mantle viscosities become lower than the best

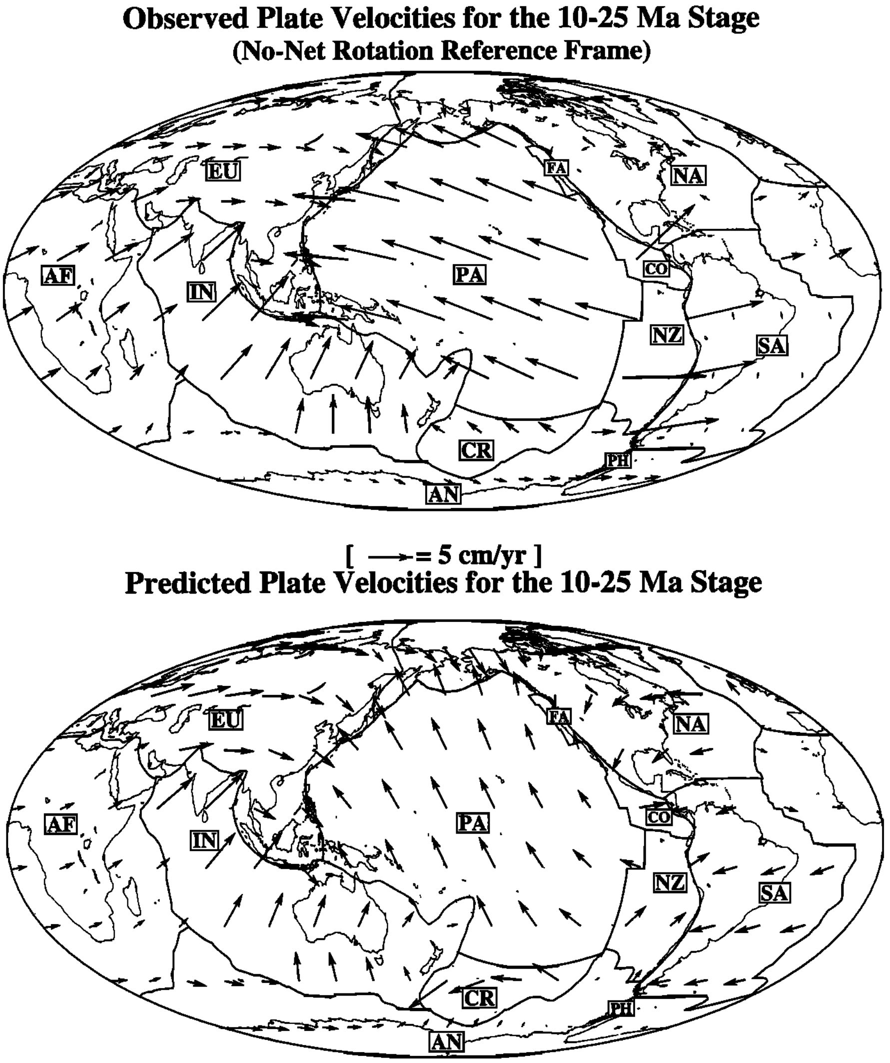
Observed Plate Velocities for the 10-25 Ma Stage
(No-Net Rotation Reference Frame)

[—→= 5 cm/yr]

Predicted Plate Velocities for the 10-25 Ma Stage

Figure 18a. (top) Observed and (bottom) predicted velocity fields in the no-net-rotation reference frame for 10–25 Ma. Arrows, plate boundaries, continental outlines, and plate codes are as described for Figure 2.

estimates cited above (less than 10^{20} Pa s) for $\eta^*_{\mathrm{Lit}} > 100$. A stiffer lithosphere requires larger torques to move the plates and therefore a lower absolute viscosity, i.e., less resistance to flow. In contrast, η^*_{LM} has a comparatively weak effect on the absolute viscosity, which decreases less than an order of magnitude for $1 < \eta^*_{\mathrm{LM}} < 1000$.

5.3. Present-Day Plate Motions

The predicted present-day plate velocities based on the model described above are highly correlated with those observed, as shown by the maps of plate velocities in Figures 17a and 17b. The model yields a best fitting absolute viscosity of $4.5 \pm 1 \times 10^{20}$ Pa s, roughly consistent with the estimates from postglacial rebound, and a total weighted correlation coefficient of 0.91 (the unweighted correlation coefficient is 0.61). The variance reduction is 96% for the horizontal divergence field and 66% for the radial vorticity. These variance reductions are much higher than those obtained by *Woodward et al.* [1993] (or *Forte et al.* [1993a]) using the density field from seismic tomographic model SH8/U4L8 (66% for the horizontal divergence and 20% for the radial vorticity). For comparison we show (Figure 17c) the plate velocities predicted using as the density heterogeneity model that inferred from tomographic model SH425.2 [*Su and Dziewonski*, 1991]. The total weighted correlation for this model using our preferred viscosity structure is 0.64, which is significantly different from our model result at the 95% confidence level. Changing the viscosity structure to yield the best possible fit to the plate velocities improves the correlation coefficient only to ~0.69. It is clear that our mantle heterogeneity model reproduces the plate velocity field much better than seismic tomography. While this does not mean that our model based on subduction history is the final picture of the internal density heterogeneity of the mantle, it does imply that what has been inferred from seismic tomography is probably not a very accurate representation of the mantle density field, since a much simpler model reproduces both the geoid and plate motions much better.

However, our models have shortcomings. For example, medium to large oceanic plates (with the possible exception of the Nazca plate) are well predicted, since

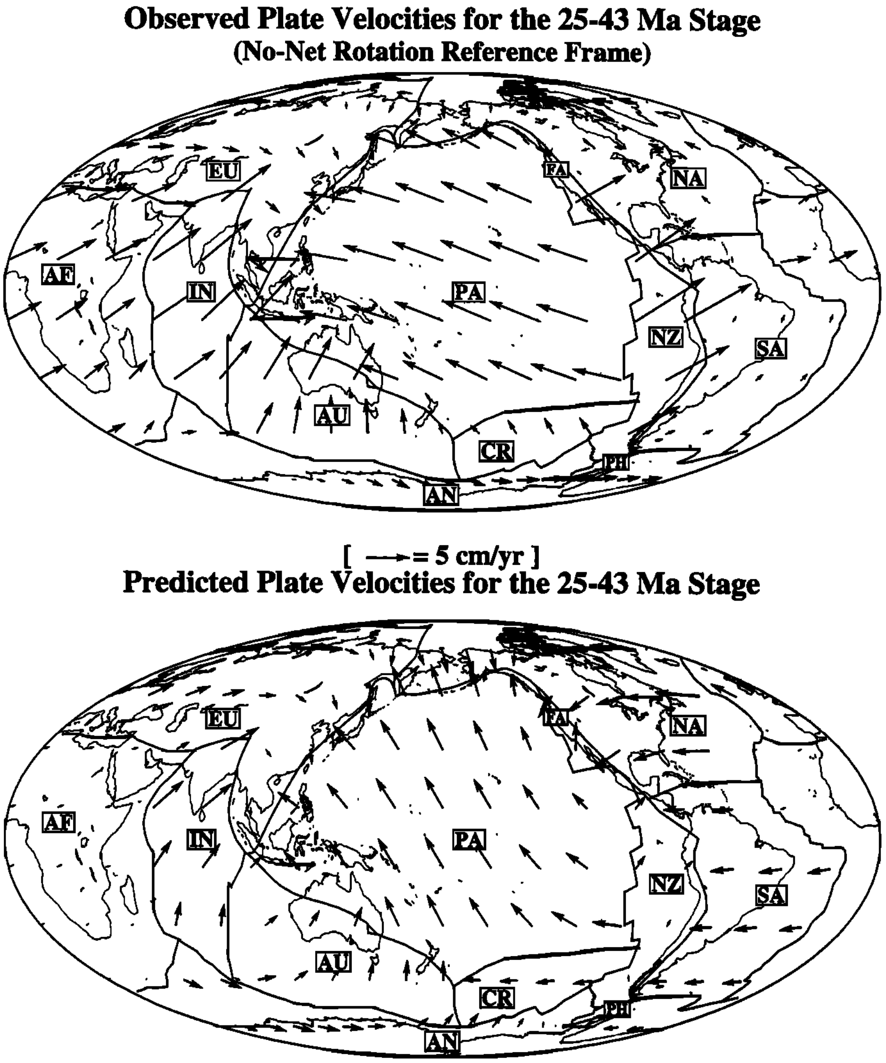

Figure 18b. (top) Observed and (bottom) predicted velocity fields in the no-net-rotation reference frame for 25–43 Ma. Arrows, plate boundaries, continental outlines, and plate codes are as described for Figure 2.

the effects of slab pull and lithospheric thickening are well accounted for, but continental velocities are overpredicted in magnitude (Eurasia, North America, Antarctica) or missed entirely (South America). For the continental plates the uncertainties in the location of old subduction zones and in the plate velocities may be more important. For example, the location of Alpine-Himalayan subduction varies greatly in different plate boundary compilations. Given the enormous amount of subduction at this boundary in the Mesozoic and Cenozoic, one can expect a variation in the location of density anomalies that will drive the African and Eurasian plates. The difficulties in matching the South American and Nazca plates may be also due to unmodeled forces, as was suggested by *Russo and Silver* [1994].

Another source of misfit for continental plates could be the absence of continental roots in our model. Assuming that the high-seismic-velocity anomalies under continents represent keels that "anchor" the plates with large continental areas to the deeper mantle [*Alvarez*, 1982], the presence of roots might reduce continental velocities. The smaller plates such as the Caribbean, Philippine (whose observed motions are highly uncertain), and Arabian plates are also not well predicted.

5.4. Cenozoic Plate Motions

Our model is successful at reproducing the rest of the Cenozoic velocity field. The observed plate velocities in the no-net-rotation reference frame and the predicted plate velocities for all remaining stages are shown in Figure 18. For the past as well as for the present, we again tend to overpredict the velocity of continental plates (Eurasia, North America, and Antarctica), and we completely mispredict the rotation vector of South America. We also fail to predict the large change in motion of the Pacific plate at 43 Ma (Figure 18b), which explains the lower correlation coefficients for the stages immediately postdating the Hawaiian-Emperor bend. We will examine this failure of our model in section 5.7.

The global correlations and corresponding 1σ confidence intervals between observed and predicted plate motions are shown in Figure 19a for our preferred model for all times. The values range between 0.7 and 0.9, well above the 95% significance level (<0.33) for

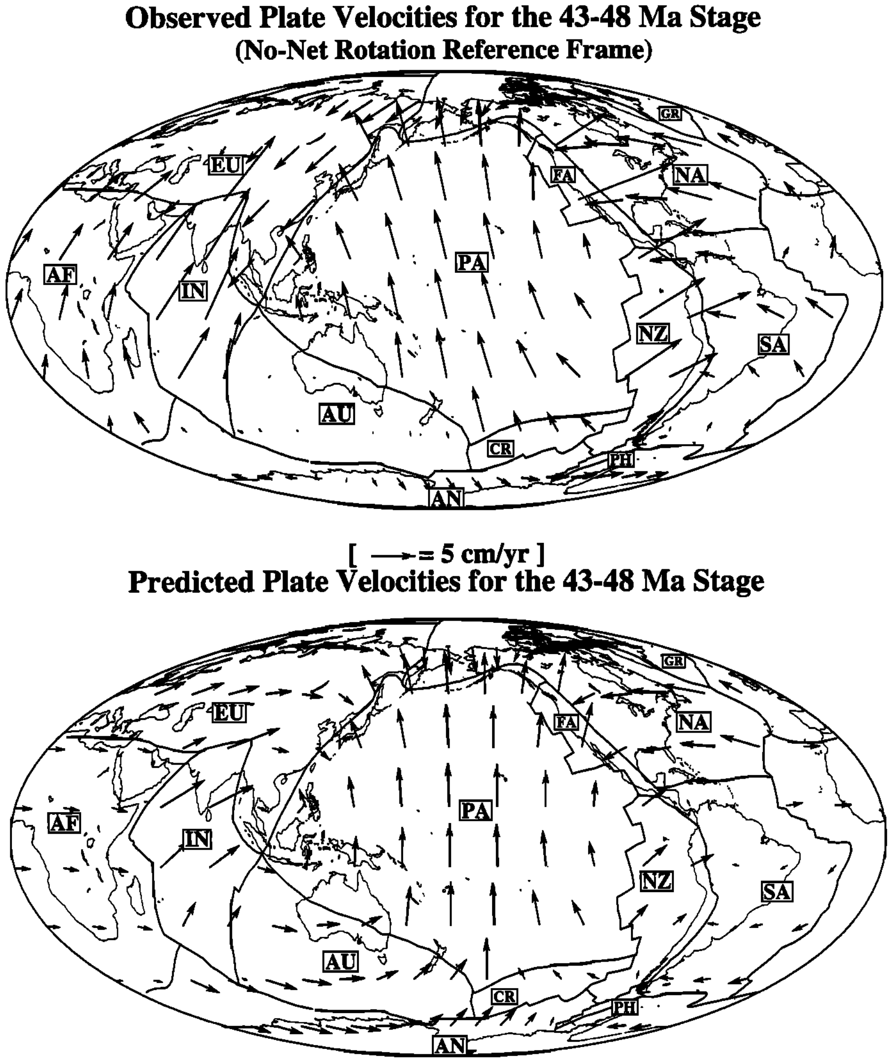

Figure 18c. (top) Observed and (bottom) predicted velocity fields in the no-net-rotation reference frame for 43–48 Ma. Arrows, plate boundaries, continental outlines, and plate codes are as described for Figure 2.

36–39 degrees of freedom (N = 12 or 13). The predicted best fit absolute viscosities as a function of plate motion stage, or time, along with their 2σ envelope are shown in Figure 19b for our preferred viscosity structure model (Table 3). The predicted values are consistent throughout the Cenozoic.

5.5. Upper Mantle Driving Forces

Although plate motions may be successfully modeled using the buoyancy forces due to the slabs in the upper mantle, we find lower mantle structure to have an important effect in driving plate motions. We have quantified the effects of lower mantle density anomalies in driving plate motions by separating the driving loads into three components: lithosphere (lithospheric thickening plus ocean-continent density difference), upper mantle, and lower mantle. We can arbitrarily remove one or two of these components to look at their individual effect on the global correlation coefficients and absolute viscosity.

We simulate the effects of plates driven entirely by the subducted slabs in the upper mantle by arbitrarily eliminating all the density heterogeneity below 670 km and keeping our preferred viscosity structure. As in our preferred model, we allow the subduction zones to develop fully in the upper mantle by running our subduction history to the end of each stage. For the present day (Figure 20a) the weighted correlation coefficient ~0.88 is slightly lower than that for our preferred model, but not significantly different at the 95% confidence level. As can be seen in Figure 20a (present-day velocities), the fit to many of the plates is considerably worse than that produced when we included the lower mantle slabs (e.g., African and Nazca plates). For the past the results are similar to those of our preferred model, as is shown by the predicted velocities for the stage 56–64 Ma (Figure 20b). Global correlation coefficients (Figure 21a) are similar to those for our preferred model throughout the Cenozoic for the upper mantle models with the noted exception of better fits for the stages immediately post-dating 43 Ma, because in this case we reproduce adequately the change in motion of the Pacific plate at 43 Ma. However, this is not a successful prediction but another example of the importance of slab pull. We discuss the meaning of this result and what constitutes a

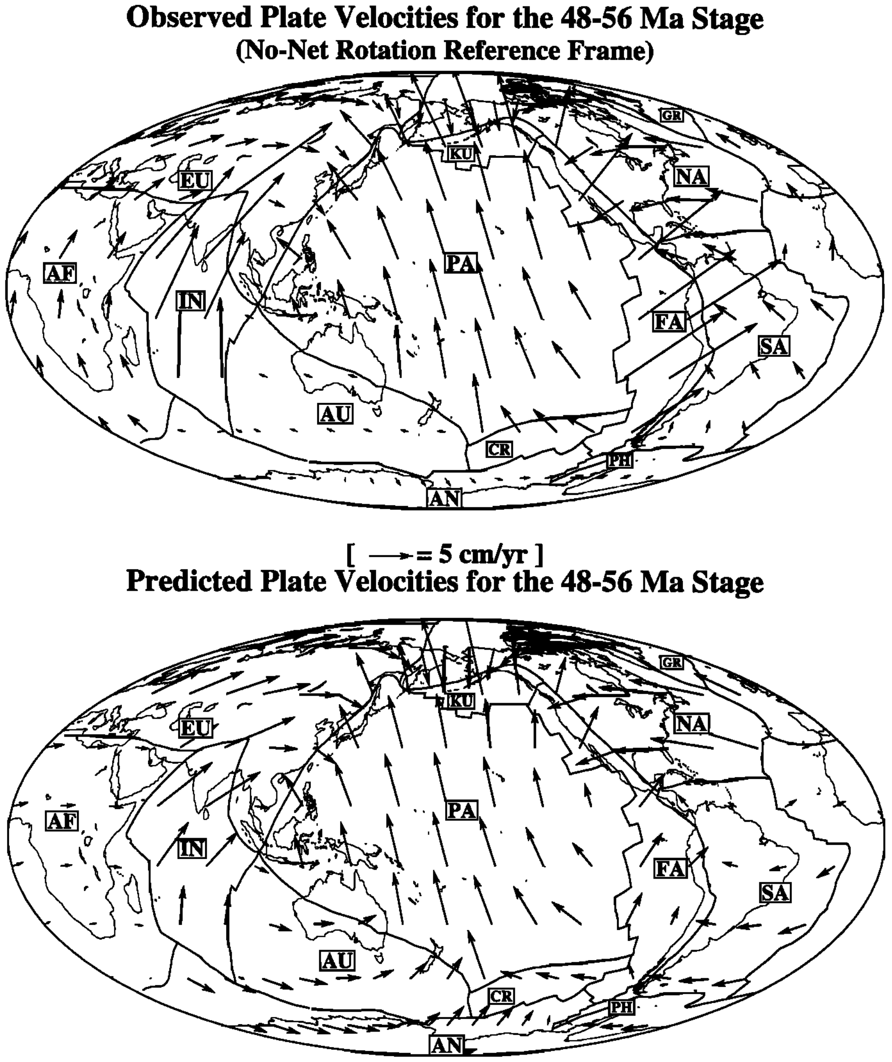

Observed Plate Velocities for the 48-56 Ma Stage
(No-Net Rotation Reference Frame)

Predicted Plate Velocities for the 48-56 Ma Stage

Figure 18d. (top) Observed and (bottom) predicted velocity fields in the no-net-rotation reference frame for 48–56 Ma. Arrows, plate boundaries, continental outlines, and plate codes are as described for Figure 2.

successful prediction in section 5.7. The absence of the lower mantle slabs decreases the best fit absolute viscosity, as is shown in Figure 21b. In a 180-Myr subduction history model that allows for slab penetration, most of the slabs are in fact in the lower mantle. The decreased magnitude of the driving forces requires a lower absolute viscosity to match the present-day plate speeds.

Similar effects on the predicted plate velocities are produced by decreasing the slowing factor *s* from 4 to 2. For the present-day velocities, such a reduction results in a correlation coefficient of 0.89 and better fits to the 10–25 and 25–43 Ma stages. A smaller *s* causes more slabs to reach the core-mantle boundary and become dynamically inert, producing a much smaller density anomaly in the lower mantle than for $s = 4$.

5.6. Driving Force Contributions

Using different distributions of mantle density heterogeneity affects the direction and magnitude of the predicted plate velocities and absolute viscosities. However, the changes are not always statistically significant (Figure 22). The only models that do not provide an acceptable fit to the present-day plate velocities are those in which the only driving loads are lithospheric thickening alone or both lithospheric thickening and the ocean-continent density difference, which yield weighted correlation coefficients of ~0.54 (0.19 unweighted) and ~0.10 (−0.42 unweighted), respectively. These values are outside the 95% confidence envelopes defining the values that are significantly different from those in our preferred model.

Throughout the Cenozoic only those models that include both upper and lower mantle slabs predict absolute viscosities consistent with the estimates of postglacial rebound previously cited. Driving the plates with lithospheric thickening alone requires a viscosity of 3×10^{19} Pa s (Figures 23a and 23b). This suggests that plates are driven mostly by slab pull and that the presence of slabs in the lower mantle is essential for achieving models of plate-driving forces consistent with other geophysical observables. We examine the balance of plate-driving forces in greater detail in the following section.

For many years a central issue in geodynamics and plate tectonics has been the relative magnitudes of the

Observed Plate Velocities for the 56-64 Ma Stage
(No-Net Rotation Reference Frame)

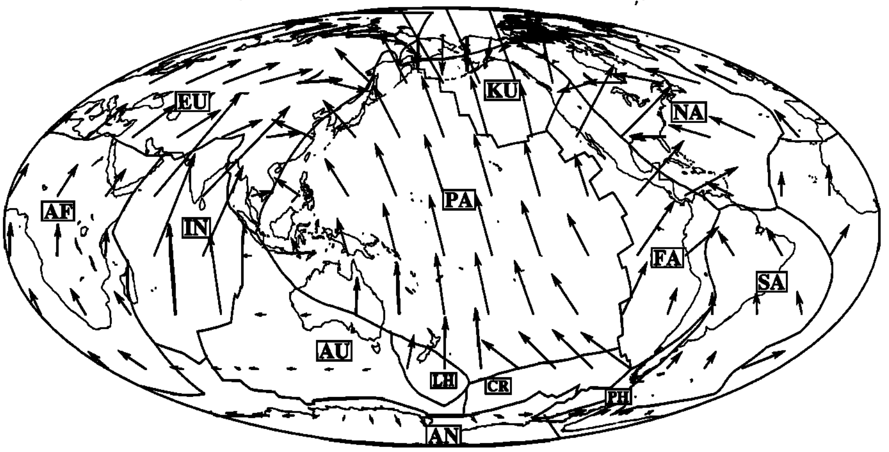

[→ = 5 cm/yr]

Predicted Plate Velocities for the 56-64 Ma Stage

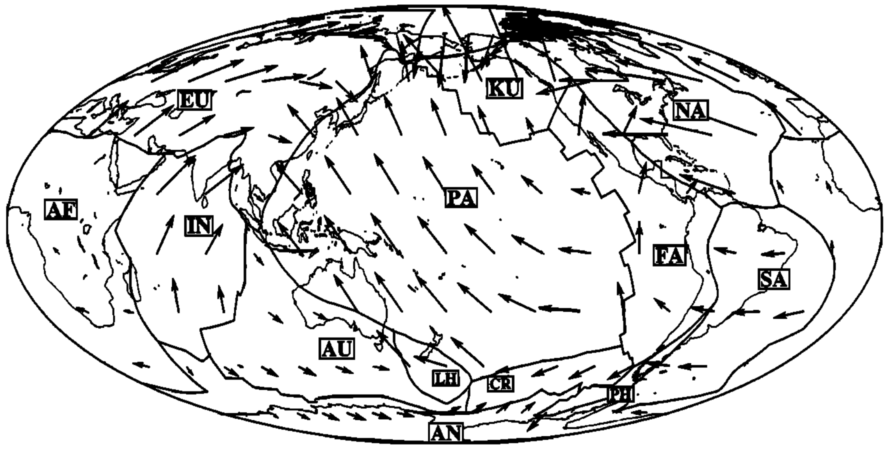

Figure 18e. (top) Observed and (bottom) predicted velocity fields in the no-net-rotation reference frame for 56–64 Ma. Arrows, plate boundaries, continental outlines, and plate codes are as described for Figure 2.

major plate-driving forces, primarily slab pull and ridge push (thermal thickening of the lithosphere). Following *Forsyth and Uyeda* [1975] and *Hager and O'Connell* [1981], their relative magnitudes have been taken to be in the vicinity of a 1:1 ratio. We have investigated this question by separating the effects of each load; i.e., the ocean-continent difference, lithospheric thickening, the upper mantle, and the lower mantle are allowed to drive the plates separately. For each load we calculate the average magnitude of the torques acting on a plate normalized to the same upper mantle viscosity, 10^{21} Pa s. The lower mantle slabs contribute approximately an order of magnitude more torque than the lithosphere and almost a factor of 2 more than upper mantle slabs. The average contribution of the continent-ocean density difference is larger than that for lithospheric thickening, a point we will address in more detail below.

The percent contribution of each load as a function of time is shown in Figure 24. The total contribution of slab pull (upper mantle plus lower mantle slabs) is in excess of 90% for all times, and that from lithospheric effects is of the order of <10%. The large value of our slab contribution is due in large part to the lower mantle slabs in our density heterogeneity model. The slight decrease in the contribution of the forces due to lithospheric thickening prior to the present stage is partially an artifact of the paucity of isochrons as we go back in time. The lack of information for older times tends to lower the estimated age for the oceanic lithosphere, and therefore the thickness and density contrast across an oceanic plate.

To address the difference between the slab pull to ridge push ratio obtained in our model and those proposed before, we look at how "inviscid" a low viscosity channel must be to allow partial or total decoupling of the lithospheric plates from their slabs. To obtain a lithospheric thickening contribution to plate driving forces equal in magnitude to that of upper mantle slabs requires more than 4 orders of magnitude viscosity contrast between the upper mantle and the low-viscosity channel, as shown in Figure 25. This result holds true whether the low-viscosity channel is ~100 or ~300 km in thickness. For lithospheric thickening to contribute 50% of driving forces (not counting the effects of lower man-

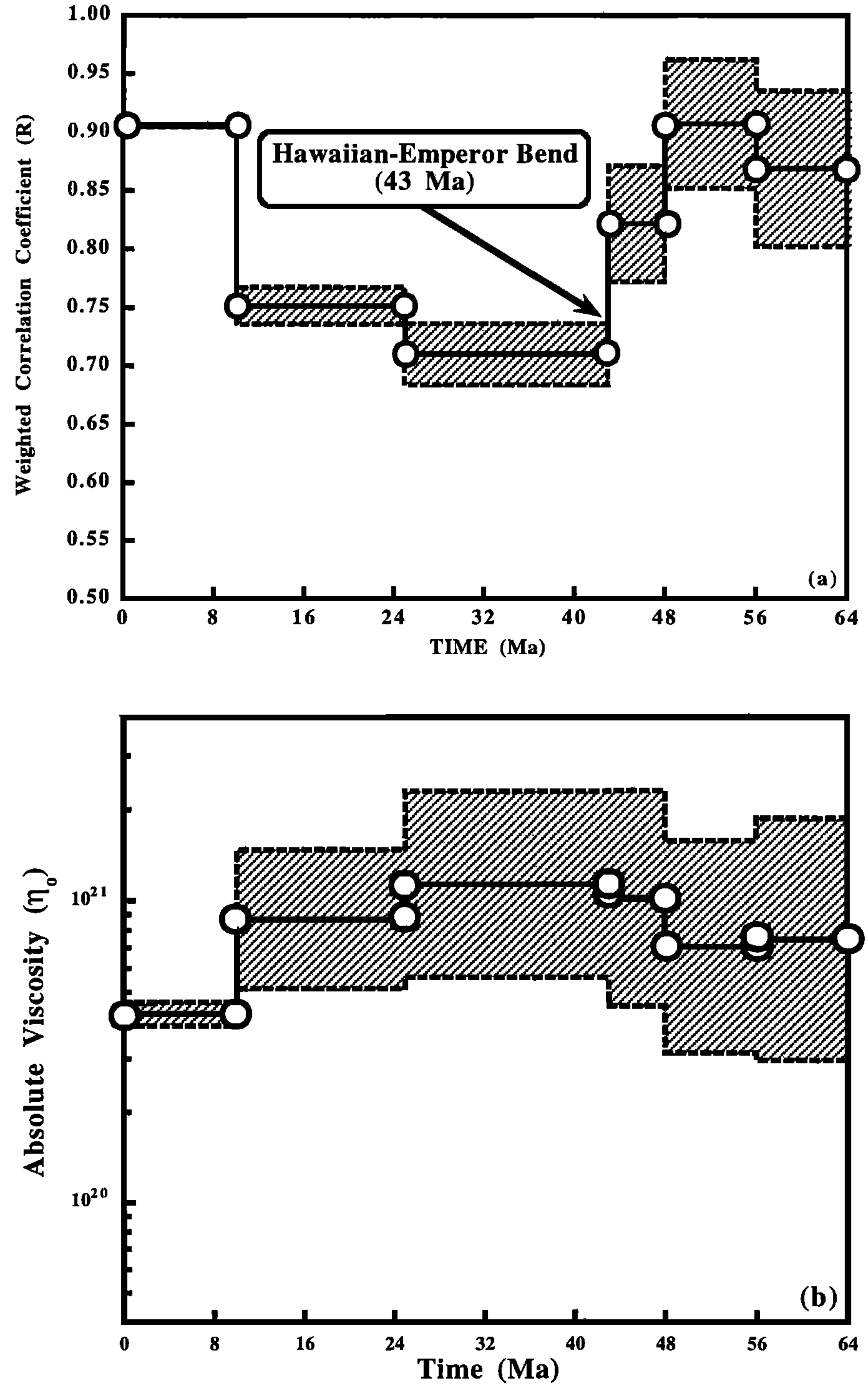

Figure 19. (a) Weighted correlation coefficients (open circles and solid line) between the observed and predicted components of plate velocities and associated confidence intervals. The circles mark the beginning and end of each stage. The predicted velocities are in the no-net-torque reference frame. For the observed velocities we use the poles of rotation of *Gordon and Jurdy* [1986], subtracting the value of the net rotation of the lithosphere with respect to the mantle. The light hatched areas around the solid lines represent the 1σ confidence interval. The temporal location of the bend in the Hawaiian-Emperor chain is indicated by the bold arrow. The 95% significance (R at which correlation becomes significant for 36 independent components) is 0.33, below the lower limit of the scale of the figure. (b) Absolute viscosity (open circles and solid line) as a function of time for our preferred model, along with the 2σ uncertainty region (hatched area) due to the errors on the observed poles of rotation.

tle slabs) the viscosity of the low viscosity channel must be lower than 10^{17} Pa s and the upper mantle viscosity must be lower than 10^{20} Pa s. Given the estimates from postglacial rebound on the viscosity of the upper mantle in the presence of a weak asthenosphere, these values are unacceptably low. Although the values of the viscosity of a suboceanic asthenosphere are not well constrained by postglacial rebound studies, it seems unlikely that the viscosity in this region is more than 2–3 orders of magnitude less than the rest of the upper mantle (that is, of the order of 10^{19} Pa s). This suggests that complete decoupling or even partial decoupling of slabs from the lithospheric plates does not occur. Not only will the slabs continue to exert their tractions, although diminished, but decoupling them leads to poor agreement with plate motion and other geophysical data, such as the geoid.

Thus we conclude that the main driving force for all plates is due to subducted slabs, which contribute more than 90% of the total. If we include only the upper mantle slabs, then the total torque contribution from lithospheric thickening is ~12–15% for our preferred viscosity structure [*Lithgow-Bertelloni and Richards*,

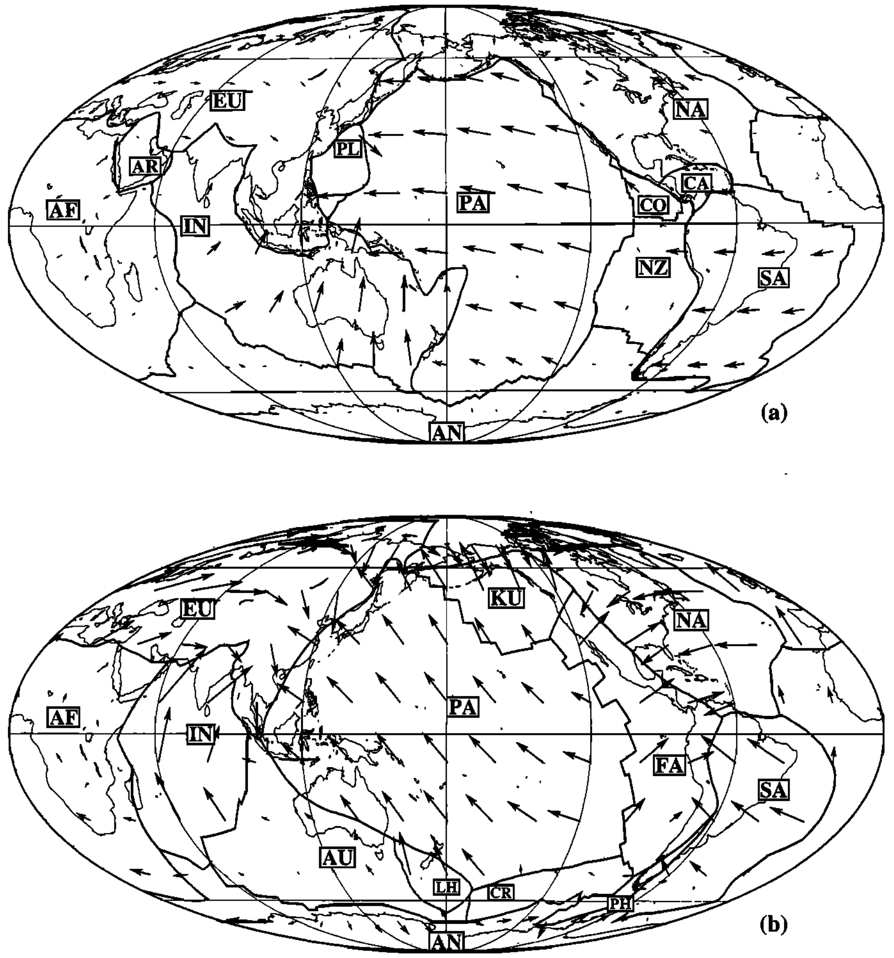

Figure 20. Predicted Cenozoic velocity field obtained by arbitrarily eliminating lower mantle structure from our density model: (a) present day and (b) 56–64 Ma. Arrows, plate boundaries, continental outlines, and plate codes are as described for Figure 2.

1995]. Using the viscosity structure of *Hager and O'Connell* [1981] (Table 3) changes the relative contribution to ~70% for the upper mantle slabs and ~30% for lithospheric thickening, in agreement with their results. Including the lower mantle slabs yields a total contribution in excess of 95% for the slab component. (The Hager and O'Connell viscosity structure, however, produces very poor fits to the observed geoid for our density field.)

5.7. Plate Motion Changes: The Hawaiian-Emperor Bend

The drastic change in motion of the Pacific plate at 43 Ma is now a somewhat contested observation, according to recent reconstructions of the Pacific plate with respect to the Hawaiian-Emperor chain (C. Raymond and J. Stock, personal communication, 1995). Although a change in direction of the plume has been proposed [*Norton*, 1995], *Richards and Griffiths* [1988] and *Griffiths and Richards* [1989] showed this to be highly unlikely for a plume with the strength of the Hawaiian plume.

If in fact the cause of the bend in the Hawaiian-Emperor chain is a change in motion of the Pacific plate, our model fails to reproduce it. As we noted previously, the correlation coefficients between observed and predicted plate velocities for our preferred model are very high, ranging between 0.7 and 0.9. This is not surprising for a model based on subduction history and lithospheric thickening, since plates tend to go toward their subduction zones [*Forsyth and Uyeda*, 1975; *Gordon et al.*, 1978; *Hager and O'Connell*, 1981]. Interestingly, however, the correlation coefficients are significantly lower for the stages immediately postdating the Hawaiian-Emperor Bend, namely 25–43 and 10–25 Ma. The degradation of the fit for these two stages is a consequence of our inability to reproduce the change from northward to westward motion of the Pacific plate, shown by the comparison of the maps of observed and predicted plate velocities for the 25–43 Ma stage in Figures 26a and 26b.

Arbitrarily eliminating lower mantle density heterogeneity results in higher correlation coefficients for these two stages (Figure 21a), as we are able to better reproduce the bend in the Hawaiian-Emperor chain. However, we must emphasize that this does not represent a successful prediction by our model of the plate change but rather is just another illustration of the fact that plates are driven by slab pull. A successful prediction would be that of a model, which reproduces the Hawaiian-Emperor bend with the density distribution at the beginning of the stage (in this case at 43 Ma), that is, a model where the slabs are not already prescribed to go in the "correct" direction. In fact, we fail to predict the

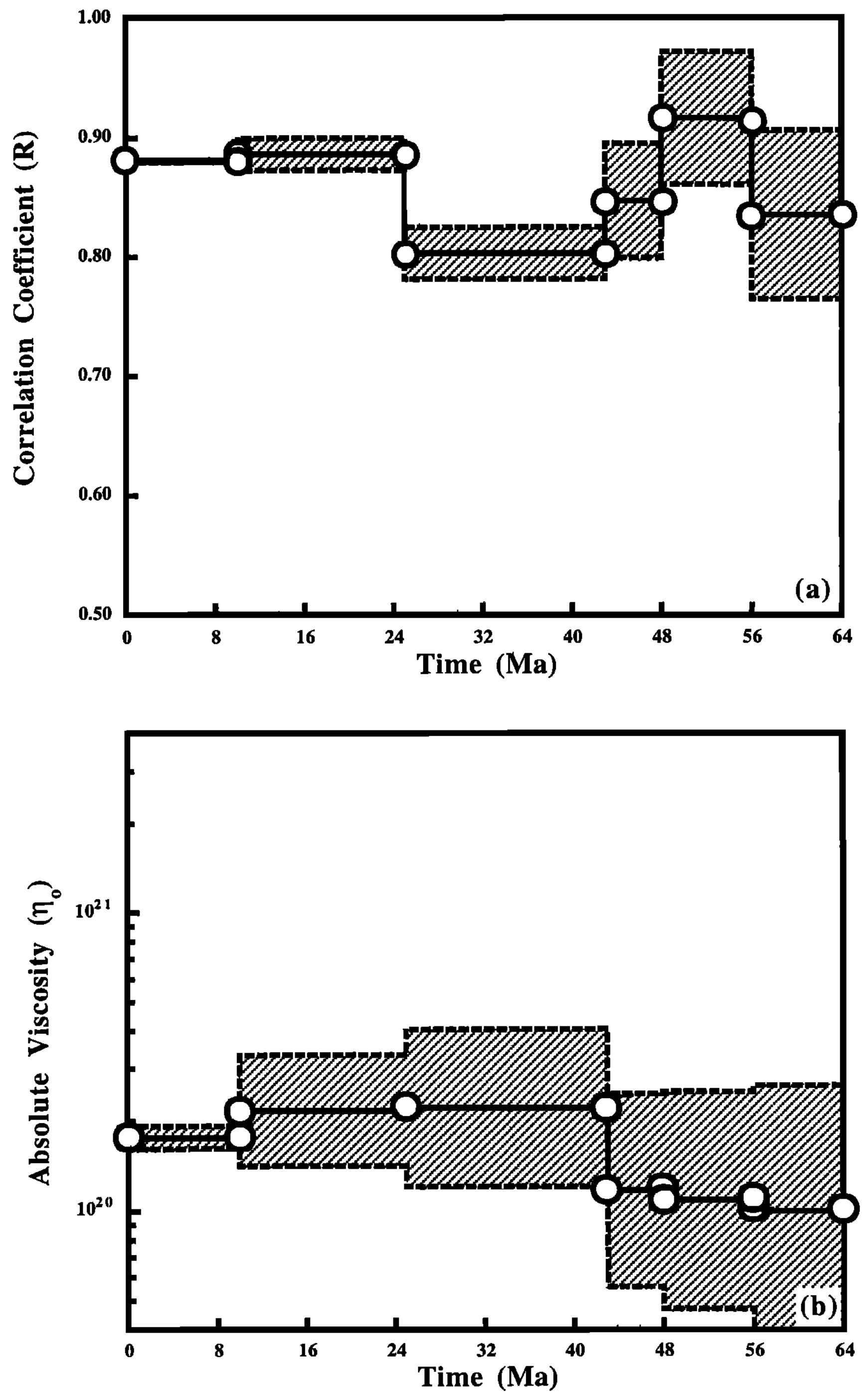

Figure 21. (a) Global correlation coefficient as a function of time for the model in which we arbitrarily remove the lower mantle density anomalies. Note, however, that the correlation is markedly higher for 25–43 Ma than for our preferred model, because in this case we reproduce the westward motion of the Pacific plate. (b) Predicted best fit absolute viscosity as a function of time for the model in which we arbitrarily remove the lower mantle density anomalies. The effective absolute viscosity of the upper mantle is greatly reduced owing to the absence of lower mantle slabs.

largest changes in plate motions throughout the Cenozoic. This is not an unexpected result in models (ours and all previous work) based on continuously evolving buoyancy fields, which cannot change as suddenly and abruptly as the changes observed in the geologic record.

What then is missing from our models? To suggest possible solutions to this paradox, we investigate in detail the cause of the Hawaiian-Emperor bend, the most striking Cenozoic plate motion rearrangement. Specifically, we test the hypothesis that the collision of India with Asia caused the westward jerk of the Pacific plate 43 million years ago.

5.7.1. The India-Asia collision hypothesis. Much has been made of the coincidence in time of the collision between India and Eurasia and the Hawaiian-Emperor bend. This is a leading hypothesis for the cause of the change in the motion of the Pacific plate at 43 Ma [*Patriat and Achache*, 1984]. We test this model by combining the Indian and Eurasian plates into one and effectively allowing infinite compressional stresses to develop along the India-Eurasia plate margin (see also *Richards and Lithgow-Bertelloni* [1996]). The observed and predicted plate motions for the 43–48 Ma stage were shown in Figure 18c and those for the 25–43 Ma

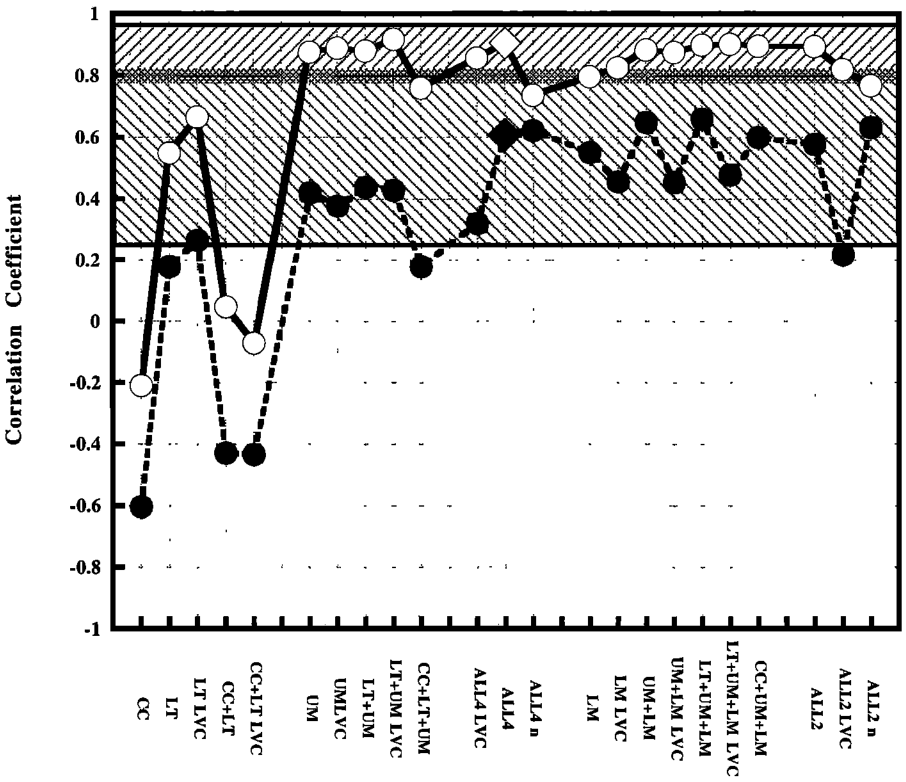

Figure 22. Weighted (open circles and solid line) and unweighted (solid circles and dashed line) correlation coefficients between predicted and observed velocity components, for different loads and viscosity structures (Table 3). The hatched lines (slanted upward to the right for the weighted (0.78–0.96) and to the left for the unweighted (0.25–0.82)) outline the 95% confidence region (the overlap is cross-hatched), outside which the values are statistically different from those of our preferred model ALL4 (shown by solid (unweighted) and open (weighted) rhombohedra). Models labeled ALL are driven by the contributions of both upper mantle (UM) and lower mantle (LM) slabs, oceanic lithospheric thickening (LT), and the ocean-continent density difference (CC). LVC indicates the presence of a low-viscosity channel that extends to 410-km depth. The numbers 2 and 4 refer to the slowing factor *s* used to reduce the velocity of the slabs in the lower mantle. The lowercase letter n indicates a model where the density contrast of the slab at the time of subduction is independent of its age.

stage in Figure 18b. The velocities at 43–48 Ma, especially the northerly direction of the Pacific plate, are well predicted while the westward motion of the Pacific plate at 25–43 Ma is not.

Figure 26 shows the effect for the 43–48 Ma stage of locking India to Asia (Figure 26a) and India to Asia and Australia (Figure 26b), simulating the maximum effective force that the collision could exert on all other plates and the effect of the suture of Australia to India at 43 Ma. There is no appreciable effect on the motion of the Pacific plate, and basically no convergence arises between the Pacific and Australian boundaries, contrary to the suggestion of *Patriat and Achache* [1984]. Similar experiments for the 25–43 Ma stage yield similar negative results [*Richards and Lithgow-Bertelloni*, 1996].

These models show that the collision of India with Asia is not a likely cause for the global rearrangement of plate motions at 43 Ma. This conclusion is independent of whole mantle versus upper (layered) mantle flow alone or the details of the model of mantle buoyancy forces used, since the main effect of the collision is to reduce the effective traction of the previously subducted lithosphere (beneath the present-day Himalayas) on the overriding plates.

5.7.2. Other Possible Causes. Neither the distribution of buoyancy forces arising from subduction and lithospheric thickening nor the buoyancy introduced by major mantle plume events are likely to change within the time scale of plate motion rearrangements. In general, abrupt changes in the internal dynamics of the mantle are not likely. The only sort of "abrupt" internal effect that has been recognized are the so-called avalanches found in recent mantle convection modeling [*Machetel and Weber*, 1991; *Solheim and Peltier*, 1992; *Tackley et al.*, 1993; *Honda et al.*, 1993]. As a result of the endothermic phase transition at 670 km, cold downwellings may pile up on top of the discontinuity and then get flushed episodically into the lower mantle. The effect of such avalanches on the surface velocity field is in fact very large; however, it is unlikely that it will cause abrupt changes in plate motions. These numerical models so far are not accurate reproductions of Earth's conditions: they suffer from lack of plates and inappropriate Rayleigh number for the Earth. Even considering the models at face value, the most important condition of plate rearrangements is not met: the timescale for the initiation of such events is of the order of 10 Myr, much longer than the few million years or less that it takes for a complete plate rearrangement to occur. More recently, *Tackley et al.* [1994] and *Bunge et al.* [1996, 1997] have shown that the avalanches are largely an artifact of 2-D geometry in previous phase change models and that 3-D models show only very subdued time variations in convective flow due to an endothermic phase change.

The only obvious remaining cause for abrupt plate motion changes is a change in plate boundary forces. At

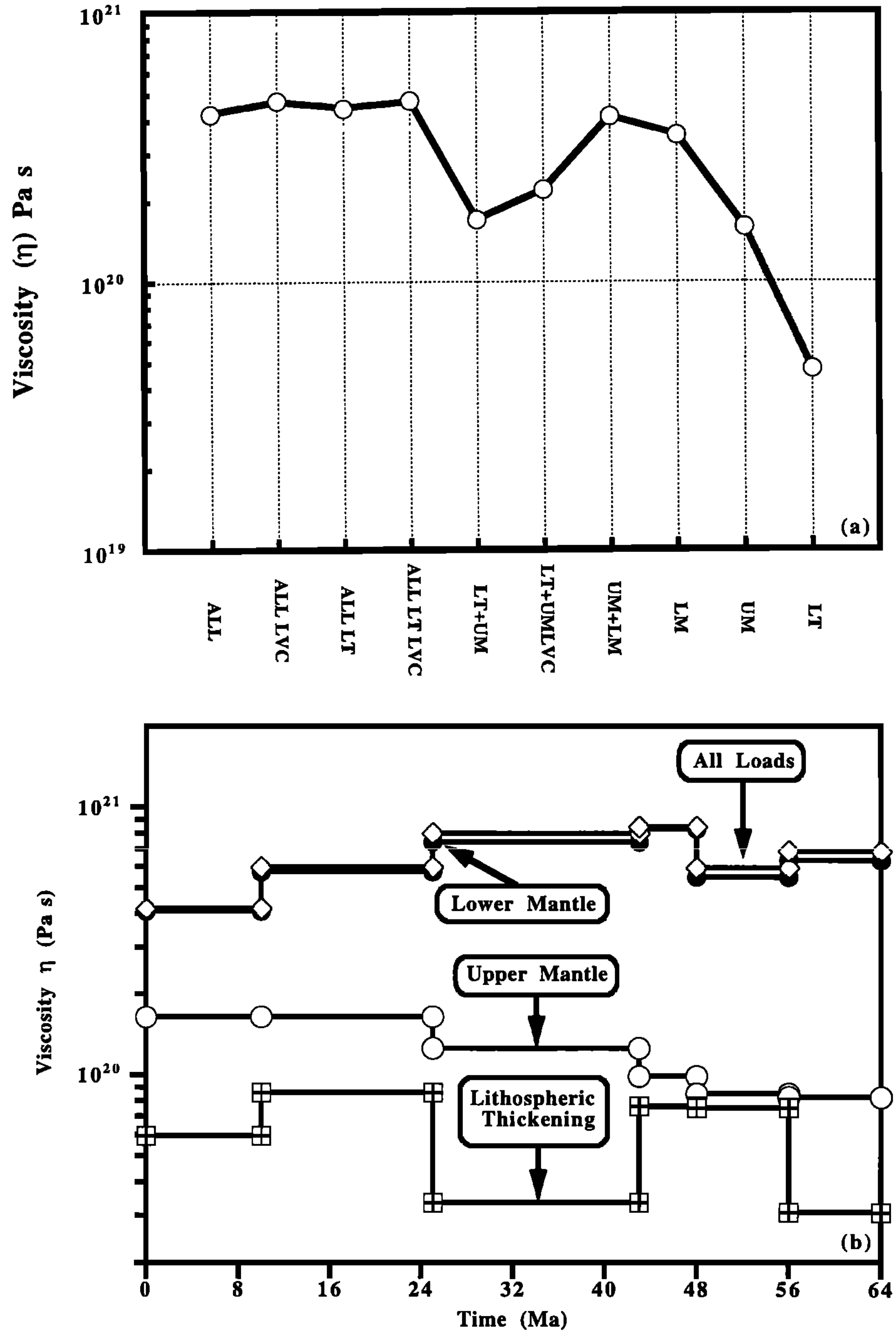

Figure 23. (a) Best fit absolute viscosity as a function of the loads used to drive the flow and the viscosity structure (i.e., whether or not there is a low-viscosity channel). Codes are the same as in Figure 22. The lower mantle slabs are essential for achieving values of the absolute viscosity in agreement with estimates from postglacial rebound. (b) Predicted best fit absolute viscosities as a function of time and type of load. The slabs in the lower mantle determine the magnitude of the absolute viscosity for all times.

43 Ma the only major plate boundary to change drastically as the result of the change in motion of the Pacific plate is the Pacific-Australian boundary. The Pacific plate evolved in the Mesozoic and in the early Cenozoic from a triple junction system among the Kula, Phoenix, and Farallon plates. The boundary between the Pacific and Australian plates was likely a set of ridges and transforms up until ~43 Ma [*Hilde et al.*, 1977]. The Pacific plate moved northward along this system until 43 Ma. With the change in motion of the Pacific plate, subduction was initiated [*Hilde et al.*, 1977; *Gordon et al.*, 1978; *Patriat and Achache*, 1984] along this boundary, perhaps with transform faults providing preexisting zones of weakness.

In our model, where all the driving forces are poloidal in nature and no special role is assigned to transform faults, we tend to underpredict the global toroidal to poloidal ratio for all times, as is shown in Figure 27. Our predictions fall outside the error bounds of the observed plate motions, and for all stages we consistently underestimate the magnitude of the toroidal field. It is interesting that the lowest predicted values correspond to the two stages that follow the initiation of the San Andreas transform system at ~30 Ma. This suggests perhaps a

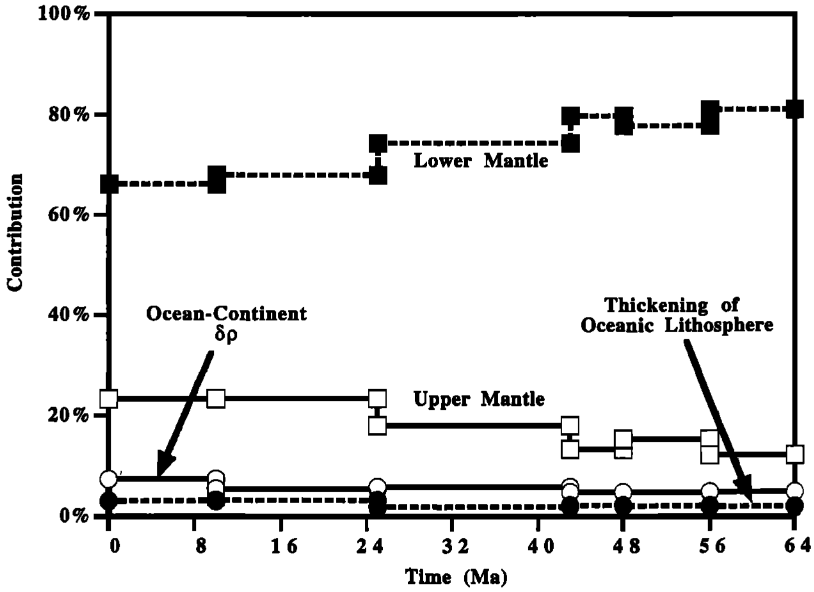

Figure 24. Percent contribution to the driving torques of lower mantle, upper mantle and lithospheric thickening loads as a function of time. The slight decrease of the lithospheric contribution as a function of time is an artifact of artificially younger lithospheric ages for the past, due to the paucity of isochron data in the older ocean basins as we go back in time.

crucial role for transforms faults in plate rearrangements and perhaps plate motions in general. We speculate that the bend in the Hawaiian-Emperor bend at 43 Ma is caused by the sudden change of the Pacific-Australian margin from transform to subduction along preexisting transforms faults [*Richards and Lithgow-Bertelloni*, 1996].

6. SUMMARY

In this paper we have presented a comprehensive account of one approach to modeling the plate-mantle system, including the philosophy of our approach, the methodology and data necessary for constructing a density heterogeneity model of the Earth's interior and

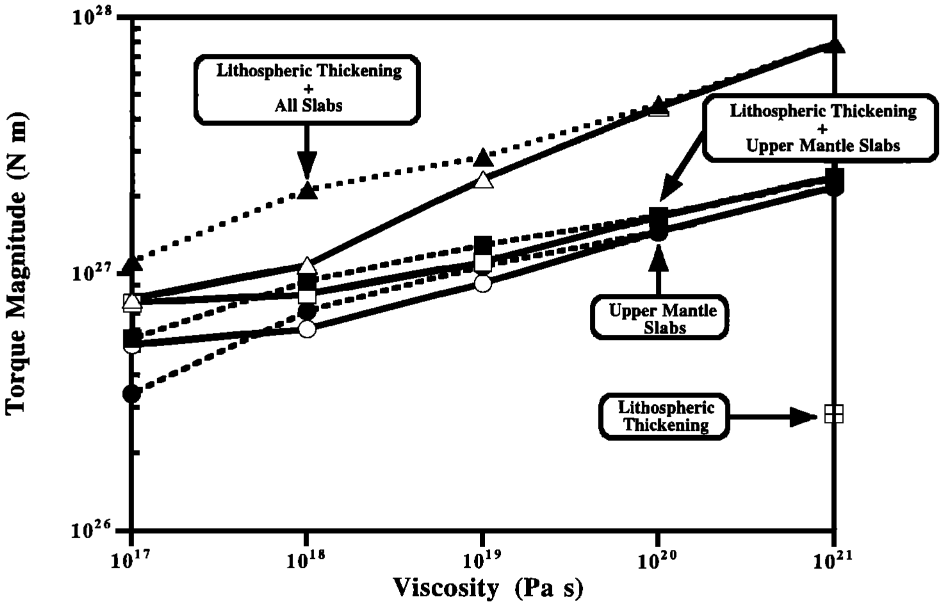

Figure 25. Effects of an increasingly less viscous low viscosity channel on the magnitude of the torques exerted by all the slabs plus lithospheric thickening (triangles), upper mantle slabs plus lithospheric thickening (squares), and upper mantle slabs alone (circles). The magnitude of the torque exerted by lithospheric thickening alone is shown for reference. The solid lines and open symbols are the results for a low-viscosity channel that extends from the bottom of the lithosphere to 410 km in depth (280 km thick), and the dashed lines and solid symbols are for one that extends only to 200 km in depth (~70–100 km thick). It is virtually impossible to decouple the slabs from the lithospheric plates or to drive them with lithospheric thickening alone or even with a lithospheric contribution equal to that of upper mantle slabs.

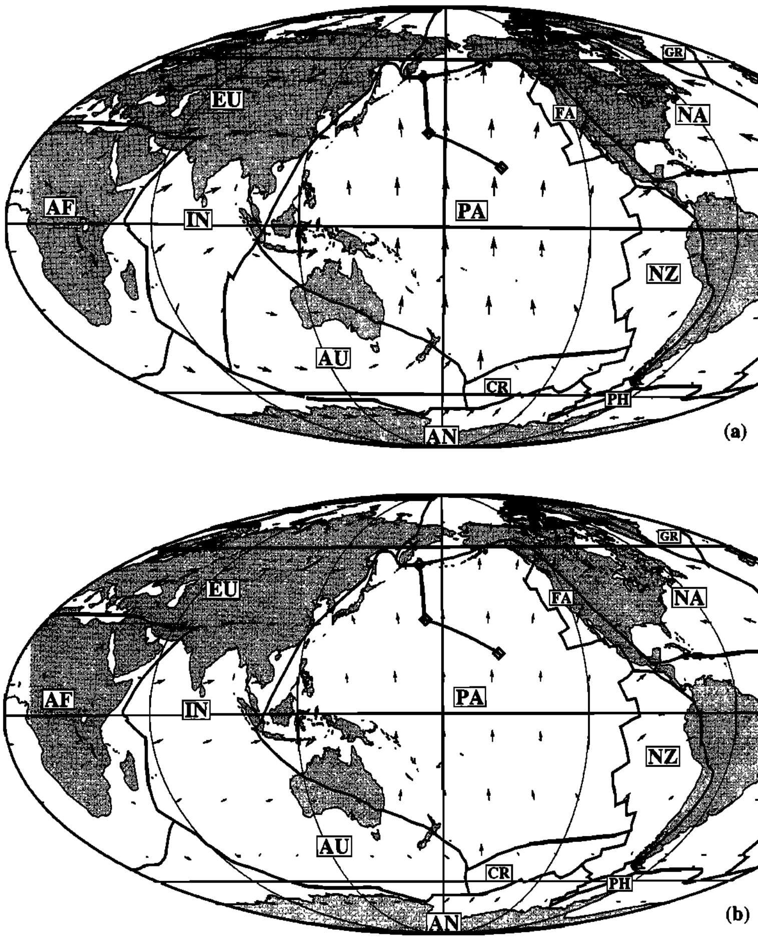

Figure 26. Predicted plate velocities for the 48–43 Ma stage for our preferred model but with (a) India locked to Asia as one plate and (b) India and Australia as one plate locked to Asia. Arrows, plate boundaries, continental outlines and plate codes are as described for Figure 2a.

calculating present and past plate-driving forces, an analysis of the fit between our model and different geophysical observables (seismic tomography, the geoid, dynamic topography, and plate motions), a sensitivity analysis of our model parameters, and a discussion of the failures and limitations of our approach. The approach we advocate is based on the guiding principle, developed in several published works [e.g., *Gurnis*, 1990; *Lithgow-Bertelloni et al.*, 1993; *Ricard et al.*, 1993], that in order to understand the dynamics of the Earth and, in particular, the connection between mantle convection and its main surface expression, plate tectonics, we must use as constraints the wealth of data contained in the plate tectonic record. Inferences concerning what forces drive plates should not be based only on the present-day state of the Earth, but instead should also include information contained in the plate tectonic record of mantle convection. Moreover, models should produce testable hypotheses regarding distinct events in the geologic record, such as continental flooding, deep basin formation, or continental uplift [e.g., *Gurnis*, 1993; *Mitrovica et al.*, 1989], and true polar wander [*Richards et al.*, 1996].

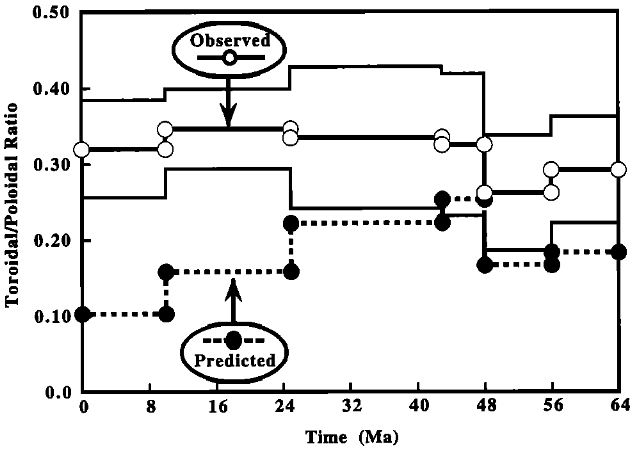

Figure 27. Observed (open circles and solid line) and predicted (solid circles and dashed line) toroidal to poloidal ratios as a function of time. The solid lines above and below the observed ratios are the 2σ confidence contours derived from the uncertainties in the poles of rotation of each plate. The predicted values are consistently underestimated. The largest underestimates for the two most recent stages suggest that we do not predict well the toroidal field associated with the initiation of the San Andreas transform system.

6.1. Kinematic Results

We have described in detail the compilation of the stage reconstructions, including plate geometries, poles of rotations, and related estimated uncertainties throughout the Cenozoic and late Mesozoic. Beyond the proper assembly of tectonic information, particular attention must be paid to the limitations of the data sets, especially as we try to push further back in time, and to the inconsistencies that arise in using reconstructions from different sources. For the scope of our study, uncertainties of the order of ~1000–2000 km in plate boundary location are not resolvable and do not affect our main conclusions. Similarly, the generous error bounds estimated for the poles of rotation allow us to identify robust conclusions from both our kinematic and dynamic analyses.

Our kinematic analysis of the last 120 Myr of plate motions shows that the observed toroidal and poloidal energy partitioning differs strongly from the equipartitioning expected for random and uncorrelated plate motions. For the present day the toroidal power is approximately one-third that of the poloidal component of the velocities. The overall ratio of toroidal to poloidal velocities shows discernible changes at 48 Ma and possibly 84 Ma. The changes in this ratio, a function of both the plate geometry and the degree of correlation among plate motions, are not the result of differences in the plate configuration for different times. These changes reflect a large increase in the poloidal component of the velocity field prior to 48 Ma, during which time the toroidal field (excluding the net rotation term) remained relatively constant. This increase in the poloidal power coincides with the well-known increase in spreading and subduction rates between 90 and 100 Ma. It is tempting to attribute this change in plate motion partitioning to a possibly larger role for mantle plumes in driving plate motions during 90–120 Ma, since plumes might be less efficient in driving toroidal plate motions than sheetlike, subducted slabs. However, this speculation remains to be tested via physical modeling.

6.2. Plate Tectonics and Mantle Heterogeneity

From the simple assumption that subducted slabs are the main source of thermal buoyancy in the mantle, we have constructed a model for the density heterogeneity of the interior. Such a model is constructed by using the easily estimated temperature contrasts associated with aging lithosphere. We find the pattern of subduction to be stable at long wavelengths over the time range considered (100–200 Myr), so that the large scale lateral density structure of the Earth is essentially the same over the entire Cenozoic. This is not unexpected, as the subduction zones over this time period have not changed substantially aside from some notable exceptions, such as the virtual disappearance of subduction at the India-Eurasia margin and the shift from northward to westward subduction in the Pacific basin. This stability might account for the small excursion in true polar wander over the Cenozoic [*Richards et al.*, 1997].

Our model for the history of subduction explains much of the midmantle seismic velocity heterogeneity seen in global tomographic models, if we retard the sinking velocity of slabs by about a factor of 4 as they enter the lower mantle. The agreement between our model and tomographic maps of the Earth's interior is good except at the top and bottom thermochemical boundary layers: the lithosphere and the core-mantle boundary. This correspondence leads us to suggest that the fate of slabs determines most of the lateral density heterogeneity in the mantle interior. The agreement between our subduction history and seismic models will increase when both the dip angle of the slab at the time of subduction and the induced return flow are taken into account. The fact that our slab model, which contains strong short-wavelength structure, agrees at long wavelength with seismic tomography also suggests that current global seismic models image a low-pass-filtered version of the existing anomalies.

The geoid calculated from the slab model is in remarkable agreement with observations, with a variance reduction upward of 80% both at long and medium wavelengths (up to degree 15). The best fit to the observed geoid is obtained for a mantle with a viscosity contrast between 40 and 50 across the 670-km discontinuity. This is a strong constraint on the radial viscosity structure of the mantle, but resolution of finer features, such as viscosity layering in the transition zone, is not possible. Combined with the general fit to the global tomography, this excellent agreement between the observed and predicted geoid suggests again that our model may be a good approximation to the thermal state of the deep mantle. It is also noteworthy that the factor of 4 by which slabs are slowed as they sink in the lower mantle, which maximizes the fit to seismic heterogeneity, is entirely consistent with the lower-upper mantle viscosity contrast that gives a best fit to the geoid.

The predicted dynamic topography at the surface due to viscous flow induced by sinking slabs is of considerable magnitude, as is the case with dynamic topography models derived from seismic tomography. These amplitudes might be overpredicted, but comparisons between the predicted topography and present-day estimates are difficult because the latter remain controversial. Despite these large amplitudes, the features that arise in looking at the evolution of dynamic topography in the Cenozoic appear to be consistent with some important features of the geological record of continental elevation changes. We predict a large uplift centered on the northwestern North American continent and eastern Siberia, as a consequence of the complete subduction of the Kula and Farallon plates after 48 Ma. Present-day elevation in these areas is higher than that expected for their average crustal thickness [*Mitrovica et al.*, 1989].

6.3. Plate Motions and Mantle Dynamics

We have modeled global plate motions through time, following a straightforward dynamic model. This model is based upon an analytical formulation of 3-D spherical flow in the mantle, induced by a prescribed density field, with plates, introduced by *Hager and O'Connell* [1979, 1981]. Our model assumes that the mantle is an incompressible Newtonian fluid of uniform composition and radially varying viscosity. We have, for the sake of simplicity, assumed whole mantle convection by letting subducted slabs penetrate the 670-km discontinuity in our flow model, allowing complete mass flux between the upper and lower mantle.

The buoyancy forces due to subducted slabs and lithospheric thickening and the continent-ocean density difference in our density heterogeneity model provide not only a good model for present-day plate motions, but also very good agreement with the observed surface motions for the entire Cenozoic. This agreement, however, is not surprising, since our model indicates to what degree plate motions are consistent with the subducted buoyancy introduced prior to a given stage.

Convergence tests with respect to all model parameters show that for a spherical harmonic degree 20 expansion, the effect of the stress singularity at plate boundaries is not severe. The absolute viscosity changes by less than 15%, and the torque magnitudes change by less than 20%, between degrees 20 and 45. In fact, we obtain reasonable estimates for both the absolute viscosity of the upper mantle and the relative viscosities of upper and lower mantle.

The preferred viscosity structure found to best fit the plate motions is completely consistent with that derived from geoid modeling. However, this should not be overemphasized, as plate motions are not very sensitive to contrasts in viscosity. Using plate motions alone, it would be impossible to resolve the viscosity structure of the mantle. Plate motions are, however, sensitive to the absolute viscosity of the mantle, to which they are inversely proportional. The best fit values required to match the plate speeds ($4–5 \times 10^{20}$ Pa s) are in good agreement with the estimates from postglacial rebound studies.

Our results indicate that the contribution to the driving forces of subducted slabs is in excess of 90%, with lithospheric contributions of the order of 10%. This result holds true even in the presence of a low-viscosity channel of varying thickness (~70–300 km) or in the absence of lower mantle slabs in the density heterogeneity model. It is impossible to achieve a 1 to 1 ratio between lithospheric thickening forces (ridge push) and the forces due to subducted slabs (slab pull) without requiring a low-viscosity channel to be many orders of magnitude less viscous than the upper mantle. This is in gross violation of postglacial rebound modeling results, even given the large uncertainties in these estimates. In the context of a whole mantle convection model, lower mantle slabs play a significant role in driving plate motions.

The success of our model for present and past plate motions is challenged by the model's inherent inability to predict rapid changes in plate motions a priori. This is not surprising for a model in which driving forces are based on a continuously evolving density field that does not change significantly on the timescale of plate rearrangements. Other forces at plate boundaries may be responsible for plate changes. We have shown that for one specific plate rearrangement, marked by the bend in the Hawaiian-Emperor chain at 43 Ma, forces arising from the collision of two plates (India and Eurasia) likely have no effect on the motion of the Pacific plate. Therefore the question remains, What is the cause of rapid changes in plate motions?

We have considered the possible role of transform faults in guiding plate motions and enabling sudden plate changes, although a physical model must await further work. As an indication of their importance, we showed that for all stages in the Cenozoic we considerably underpredict the magnitude of the toroidal power and therefore the toroidal to poloidal ratio of plate velocities. This failure does not severely hamper our ability to predict plate motions consistent with observations for most of the Cenozoic, except for those stages that exhibit large changes in plate motions.

7. FUTURE WORK

In this rather exhaustive treatment of the plate motion problem, we have probably pushed our straightforward, analytical approach and our simplifying assumptions about as far as can be justified (or perhaps farther!). However, our results clearly indicate where progress may be made on a number of fronts, some of which are less obvious than others. Perhaps the greatest need of all is continuing attention to organizing and improving plate motion reconstructions for use in geodynamics. Also, the record of plate motions as it stands certainly begs for more realistic treatment of plate boundary fault mechanics. More obvious pathways to improvement include developing large-scale numerical flow models constrained by plate motions, better calibration of such models with seismic heterogeneity images, and more complete use of the geological record of plate dynamics, i.e., intraplate stresses and dynamic topography.

7.1. Plate Motion Reconstructions

A significant advance will be made possible by simply compiling self-consistent databases of all the necessary information required to conduct geodynamical modeling in the fashion illustrated by our work. Major improvements in plate reconstructions should be possible.

1. First and foremost, global plate reconstructions, i.e., complete plate boundaries, for stages could be made

at much finer resolution (shorter time intervals). While ideally the goal would be to extend the type of information we have compiled beyond 200 Ma, the lack of information in ocean basins makes this task next to impossible. However, by identifying crucial times in Earth history, coincident with changes in the nature of plate activity, in the recent past and refining reconstructions around those periods, we could gain important geodynamic insight into the cause and mechanism of plate changes.

2. Rotation poles in an absolute reference frame could be tabulated along with error estimates for all times and all major plates.
3. Uncertainties in the positions of plate boundaries could be estimated. A vast improvement would come from alternative reconstructions for the same stage and identification of controversial or problematic plate boundaries.
4. A digital database could be compiled of oceanic ages for the oceanic floor and the positions of continental margins for all stages.
5. Subducted plates could be recreated according to plate tectonic rules (i.e., "virtual" plates) in order to facilitate numerical convection models constrained by plate motions.

7.2. Physical Treatment of Plate Boundaries

Major progress can be made by incorporating better physical models of plate boundary behavior into dynamic models. Although generating plates from "first principles" remains a worthy goal in geodynamics [e.g., *Bercovici*, 1993], simply allowing for fault-like behavior at plate boundaries provides an important empirical modeling tool. Plate boundary faults should include frictional resistance and "motion guide" effects, and it is probably possible to model such behavior in both analytical and numerical models using iterative procedures. An advance along these lines was recently introduced in 2-D numerical modeling by *Zhong and Gurnis* [1995], who showed how to use a "slippery node" finite element technique to incorporate an advectable thrust fault into subduction zone models. In 3-D models we suggest that the most necessary advance will be incorporation of similar Lagrangian-type constraints on transform fault behavior. Time-dependent numerical models should also be developed that allow for continuous creation and destruction of plates at subduction zones and ridges. All of these goals seem straightforward within the context of available 3-D finite element convection models [*Bunge and Baumgardner*, 1995].

7.3. Numerical Convection Models and Mantle Heterogeneity

The so-called slab model that we have introduced involves crude assumptions regarding advection of thermal anomalies, and an obvious improvement is to substitute a high-resolution numerical flow code for the simple kinematic constraints we have imposed on subducted slab trajectories. Such models can, of course, incorporate sophisticated effects, such as phase changes, variable viscosity, or even chemical layering. Some preliminary efforts in this direction have already been made [*Zhang and Christensen*, 1993], and we are in the process of implementing high-resolution convection calculations constrained by the history of global plate motions [*Bunge and Richards*, 1996]. Perhaps the most immediate utility of such an approach will be in further reconciling seismic images of mantle heterogeneity with heterogeneities predicted by global plate motion models, especially at the regional scale [e.g., *van der Hilst et al.*, 1991; *Grand*, 1994]. In fact, it is certainly not too ambitious to suggest a combined seismic-geodynamic reference Earth model derived from such an approach [*Navrotsky et al.*, 1995; *Ricard et al.*, 1996].

7.4. Geologic Constraints

Our results show the power of using one type of geological information, namely, the record of plate motions, to constrain mantle dynamics. However, we hope that the true payoff of continued efforts will lie in further understanding the geologic record. Two particularly important geologic constraints are stress and strain in the crust and dynamic topography, especially as reflected in regional and global sea level fluctuations. The tectonic stress field is the agent which preserves in the crust a memory of past dynamic processes. The present state of stress of the plates and its recent evolution has a bearing on diverse geological phenomena including the distribution of earthquakes, mountain building events, the existence of large extensional regions, and sedimentary basin formation, but the record of intraplate stresses may also hold the key to explaining the causes of changes in plate motions. Improved modeling of intraplate stresses requires resolution of technical problems associated with modeling plate boundaries, especially the "stress singularity" problem attendant to fluid dynamic models of plate tectonics. The latter problem should be solvable via implementation of a simple yield-stress criterion along plate boundaries.

Perhaps the most uncertain area for future work involves dynamic topography. Observational constraints are difficult to synthesize from stratigraphic data, and there remains the overall problem that whole-mantle convection models predict dynamic topography amplitudes that are generally too large by more than a factor of 2. However, detailed regional and some global models for subduction related vertical motions appear largely successful [e.g., *Mitrovica et al.*, 1989; *Gurnis*, 1993], and the role of mantle layering in controlling dynamic topography has hardly been explored.

We wish to emphasize that all of the directions for future work we have outlined are within the reach of current theoretical, computational, and observational resources in geology and geophysics, and we therefore expect exciting advances in the near future toward understanding the relations among global plate motions, mantle dynamics, and the geological record.

ACKNOWLEDGMENTS. We thank Paul Meijer and Jerry Mitrovica for their thoughtful reviews, which greatly improved the manuscript. We also thank K. Furlong for his comments and assistance. This work was partly supported by a NSF postdoctoral fellowship to C. Lithgow-Bertelloni.

Kevin Furlong was the Editor responsible for this paper. He thanks Jerry Mitrorica and Paul Meijer for technical reviews, and Tom Torgersen for the cross-disciplinary review.

REFERENCES

Alvarez, W., Geological evidence for the geographical pattern of mantle return flow and the driving mechanism of plate tectonics, *J. Geophys. Res.*, *87*, 6697–6710, 1982.

Baumgardner, J. R., Three-dimensional treatment of convective flow in the Earth's mantle, *J. Stat. Phys.*, *39*, 501–511, 1985.

Bercovici, D., A simple model of plate generation from mantle flow, *Geophys. J. Int.*, *114*, 635–650, 1993.

Bercovici, D., G. Schubert, and G. A. Glatzmaier, Three-dimensional convection of an infinite-Prandtl-number compressible fluid in a basally heated spherical shell, *J. Fluid Mech.*, *239*, 683–719, 1992.

Bina, C. R., and P. G. Silver, Constraints on lower mantle composition and temperature from density and bulk sound velocity profiles, *Geophys. Res. Lett.*, *17*, 1153–1156, 1990.

Bukowinski, M. S. T., and G. H. Wolf, Thermodynamically consistent decompression: Implications for lower mantle composition, *J. Geophys. Res.*, *95*, 12,583–12,593, 1990.

Bunge, H. P., and J. R. Baumgardner, Mantle convection modeling on parallel virtual machines, *Comput. Phys.*, *9*, 207–215, 1995.

Bunge, H. P., and M. A. Richards, The origin of long-wavelength structure in mantle convection: Effects of plate motions and viscosity stratification, *Geophys. Res. Lett.*, *23*, 2987–2990, 1996.

Bunge, H. P., M. A. Richards, and J. R. Baumgardner, The effect of depth-dependent viscosity on the planform of mantle convection, *Nature*, *379*, 436–438, 1996.

Bunge, H. P., M. A. Richards, and J. R. Baumgardner, A sensitivity study of 3-D spherical mantle convection at 10^8 Rayleigh number: Effects of depth-dependent viscosity, heating mode, and an endothermic phase change, *J. Geophys. Res.*, *102*, 11,991–12,007, 1997.

Čadek, O., and Y. Ricard, Toroidal poloidal energy partitioning and global lithospheric rotation during Cenozoic time, *Earth Planet. Sci. Lett.*, *103*, 621–634, 1992.

Cazenave, A., A. Souriau, and K. Dominh, Global coupling of Earth surface topography with hotspots, geoid and mantle heterogeneities, *Nature*, *340*, 54–57, 1989.

Chandrasekhar, S., *Hydromagnetic and Hydrodynamic Stability*, 652 pp., Dover, Mineola, New York, 1961.

Chang, T., J. Stock, and P. Molnar, The rotation group in plate tectonics and the representation of uncertainties of plate reconstructions, *Geophys. J. Int.*, *101*, 649–661, 1990.

Chapple, W. M., and T. E. Tullis, Evaluation of the forces that drive the plates, *J. Geophys. Res.*, *82*, 1967–1984, 1977.

Christensen, U. R., Dynamic phase boundary topography by latent heat effects, *Earth Planet. Sci. Lett.*, in press, 1998.

Colin, P., and L. Fleitout, Topography of the ocean floor: Thermal evolution of the lithosphere and interaction of mantle heterogeneities with the lithosphere, *Geophys. Res. Lett.*, *17*, 1961–1964, 1990.

Creager, K. C., and T. H. Jordan, Slab penetration into the lower mantle beneath the Marianas and other island arcs of the northwest Pacific, *J. Geophys. Res.*, *90*, 10,292–10,300, 1985.

Davies, G. F., Ocean bathymetry and mantle convection, I, Large scale flow and hotspots, *J. Geophys. Res.*, *93*, 10,467–10,480, 1988.

Davies, G. F., and M. A. Richards, Mantle convection, *J. Geol.*, *49*, 459–486, 1992.

De Mets, C., R. G. Gordon, D. F. Argus, and S. Stein, Current plate motions, *Geophys. J. Int.*, *101*, 425–478, 1990.

Deparis, V., H. Legros, and Y. Ricard, Mass anomalies due to subducted slabs and simulations of plate motion since 200 my, *Phys. Earth Planet. Inter.*, *89*, 271–280, 1995.

Engebretson, D. C., A. Cox, and R. G. Gordon, Relative motions between oceanic and continental plates in the Pacific basin, *Spec. Pap., Geol. Soc. Am.*, *206*, 1985.

Engebretson, D. C., K. P. Kelly, H. J. Cashman, and M. A. Richards, 180 million years of subduction, *GSA Today*, *2*, 93–95, 1992.

Forsyth, D. W., and S. Uyeda, On the relative importance of driving forces of plate motions, *Geophys. J. R. Astron. Soc.*, *43*, 163–200, 1975.

Forte, A. M., and J. X. Mitrovica, New inferences of mantle viscosity from joint inversion of long-wavelength mantle convection and post-glacial rebound data, *Geophys. Res. Lett.*, *23*, 1147–1150, 1996.

Forte, A. M., and W. R. Peltier, Plate tectonics and aspherical Earth structure: The importance of poloidal-toroidal coupling, *J. Geophys. Res.*, *92,* 3645–3679, 1987.

Forte, A. M., and W. R. Peltier, The kinematics and dynamics of poloidal-toroidal coupling in mantle flow: The importance of surface plates and lateral viscosity variations, *Adv. Geophys.*, *36*, 1–116, 1994.

Forte, A. M., A. M. Dziewonski, and R. L. Woodward, Aspherical structure of the mantle, tectonic plate motions, nonhydrostatic geoid, and topography of the core-mantle boundary, in *Dynamics of the Earth's Deep Interior and Earth Rotation, Geophys. Monogr. Ser.*, vol. 72, edited by J. L. Le Mouël, D. E. Smylie, and T. Herring, pp. 135–166, AGU, Washington, D. C., 1993a.

Forte, A. M., W. R. Peltier, A. M. Dziewonski, and R. L. Woodward, Dynamic surface topography—A new interpretation based upon mantle flow models derived from seismic tomography, *Geophys. Res. Lett.*, *20*, 225–228, 1993b.

Forte, A. M., R. L. Woodward, and A. M. Dziewonski, Joint inversions of seismic and geodynamic data for models of three-dimensional mantle heterogeneity, *J. Geophys. Res.*, *99*, 21,857–21,877, 1994.

Frank, F. C., Plate tectonics, The analogy with glacial flow, and isostasy, in *Flow and Fracture of Rocks, Geophys. Monogr. Series*, vol. 16, edited by H. C. Heard et al., pp. 285–292, AGU, Washington, D. C., 1972.

Gable, C. W., R. J. O'Connell, and B. J. Travis, Convection in three dimensions with surface plates: Generation of toroidal flow, *J. Geophys. Res.*, *96*, 8391–8405, 1991.

Gordon, R. G., and D. M. Jurdy, Cenozoic global plate motions, *J. Geophys. Res.*, *91*, 12,389–12,406, 1986.

Gordon, R. G., A. Cox, and C. E. Harter, Absolute motion of an individual plate estimated from its ridge and trench boundaries, *Nature*, *274*, 752–755, 1978.

Grand, S. P., Tomographic inversion for shear velocity beneath the North American plate, *J. Geophys. Res.*, *92*, 14,065–14,090, 1987.

Grand, S. P., Mantle shear velocity structure beneath the Americas and surrounding oceans, *J. Geophys. Res.*, *99*, 11,591–11,621, 1994.

Grand, S. P., R. D. van der Hilst, and S. Widiyantoro, Global seismic tomography: A snapshot of convection in the Earth, *GSA Today*, *7*, 1–7, 1997.

Griffiths, R. W., and M. A. Richards, The adjustments of mantle plumes to changes in plate motion, *Geophys. Res. Lett.*, *16*, 437–440, 1989.

Gripp, A. E., and R. G. Gordon, Current plate velocities relative to the hotspots incorporating the NUVEL-1 global plate motion model, *Geophys. Res. Lett.*, *17*, 1109–1112, 1990.

Gurnis, M., Ridge spreading, subduction, and sea level fluctuations, *Science*, *250*, 970–972, 1990.

Gurnis, M., Phanerozoic marine inundation of continents driven by dynamic topography above subducting slabs, *Nature*, *364*, 589–593, 1993.

Gurnis, M., and G. F. Davies, Numerical models of high Rayleigh number convection in a medium with depth-dependent viscosity, *Geophys. J. R. Astron. Soc.*, *85*, 523–541, 1986.

Hager, B. H., Subducted slabs and the geoid: Constraints on mantle rheology and flow, *J. Geophys. Res.*, *89*, 6003–6015, 1984.

Hager, B. H., and R. J. O'Connell, Subduction zone dip angles and flow driven by plate motions, *Tectonophysics*, *50*, 111–133, 1978.

Hager, B. H., and R. J. O'Connell, Kinematic models of large-scale flow in the Earth's mantle, *J. Geophys. Res.*, *84*, 1031–1048, 1979.

Hager, B. H., and R. J. O'Connell, A simple global model of plate dynamics and mantle convection, *J. Geophys. Res.*, *86*, 4843–4867, 1981.

Hager, B. H., R. W. Clayton, M. A. Richards, A. M. Dziewonski, and R. P. Comer, Lower mantle heterogeneity, dynamic topography, and the geoid, *Nature*, *313*, 541–545, 1985.

Harland, W. B., A. V. Cox, P. G. Llewellyn, C. A. G. Pickton, A. G. Smith, and R. Walters, *A Geologic Time Scale*, *Cambridge Earth Sci. Ser.*, edited by A. H. Cook et al., 130 pp., Cambridge Univ. Press, New York, 1982.

Haskell, N. A., The motion of a viscous fluid under a surface load, I, *Physics*, *6*, 265–269, 1935.

Hilde, T. W. C., S. Uyeda, and L. Kroenke, Evolution of the western Pacific and its margin, *Tectonophysics*, *38*, 145–165, 1977.

Honda, S., S. Balachandar, D. A. Yuen, and D. Reuteler, 3-dimensional instabilities of mantle convection with multiple phase transitions, *Science*, *259*, 1308–1311, 1993.

Jeanloz, R., and E. Knittle, Density and composition of the lower mantle, *Philos. Trans. R. Soc. London, Ser. A*, *328*, 377–389, 1985.

Jordan, T. H., The continental tectosphere, *Rev. Geophys.*, *13*, 1–12, 1975.

Jurdy, D. M., and M. Stefanick, Errors in plate rotations as described by covariance matrices and their combination in reconstructions, *J. Geophys. Res.*, *92*, 6310–6318, 1987.

Jurdy, D. M., and M. Stefanick, Plate-driving forces over the Cenozoic Era, *J. Geophys. Res.*, *93*, 11,833–11,844, 1988.

Jurdy, D. M., and M. Stefanick, The forces driving the plates: Constraints from kinematics and stress observations, *Philos. Trans. R. Soc. London, Ser. A*, *337*, 127–139, 1991.

Karato, S., and P. Wu, Rheology of the upper mantle: A synthesis, *Science*, *260*, 771–778, 1993.

Kaula, W. M., Product-sum conversion of spherical harmonics with application to thermal convection, *J. Geophys. Res.*, *80*, 225–231, 1975.

Kaula, W. M., Material properties for mantle convection consistent with observed surface fields, *J. Geophys. Res.*, *85*, 7031–7044, 1980.

King, S. D., and G. Masters, An inversion for radial viscosity structure using seismic tomography, *Geophys. Res. Lett.*, *19*, 1551–1554, 1992.

Körnig, M., and G. Müller, Rheological models and interpretation of post-glacial uplift, *Geophys. J. Int.*, *98*, 243–253, 1989.

Larson, R. L., Latest pulse of Earth: Evidence for a mid-Cretaceous superplume, *Geology*, *19*, 547–550, 1991.

Larson, R. L., and C. G. Chase, Late Mesozoic evolution of the western Pacific Ocean, *Geol. Soc. Am. Bull.*, *83*, 3627–3644, 1972.

Larson, R. L., and W. C. Pitman, World-wide correlation of Mesozoic magnetic anomalies and its implications, *Geol. Soc. Am. Bull.*, *83*, 3645–3662, 1972.

LeStunff, Y., and Y. Ricard, Topography and geoid due to lithospheric mass anomalies, *Geophys. J. Int.*, *122*, 982–990, 1995.

LeStunff, Y., and Y. Ricard, Partial advection of equidensity surfaces: A solution for the dynamic topography problem?, *J. Geophys. Res.*, *102*, 24,655–24,667, 1997.

Li, X., and B. Romanowicz, Global mantle shear-velocity model developed using nonlinear asymptotic coupling theory, *J. Geophys. Res.*, *101*, 22,245–22,272, 1996.

Lister, C. R. B., Gravitational drive on oceanic plates caused by thermal contraction, *Nature*, *257*, 663–665, 1975.

Lithgow-Bertelloni, C., and M. A. Richards, Cenozoic plate driving forces, *Geophys. Res. Lett.*, *22*, 1317–1320, 1995.

Lithgow-Bertelloni, C., M. A. Richards, Y. Ricard, R. J. O'Connell, and D. C. Engebretson, Toroidal-poloidal partitioning of plate motion since 120 Ma, *Geophys. Res. Lett.*, *20*, 357–378, 1993.

Lliboutry, L., The driving mechanism, its source of energy, and its evolution studied with a three-layer model, *J. Geophys. Res.*, *77*, 3759–3770, 1972.

Machetel, P., and P. Weber, Intermittent layered convection in a model mantle with an endothermic phase change at 670 km, *Nature*, *350*, 55–57, 1991.

McKenzie, D. P., A. B. Watts, B. Parsons, and M. Roufosse, Planform of mantle convection beneath the Pacific Ocean, *Nature*, *288*, 442–446, 1980.

Minster, J. B., and T. H. Jordan, Present-day plate motions, *J. Geophys. Res.*, *83*, 5331–5354, 1978.

Mitrovica, J. X., *Haskell* [1935] revisited, *J. Geophys. Res.*, *101*, 555–569, 1996.

Mitrovica, J. X., and A. M. Forte, Radial profile of mantle viscosity: Results from the joint inversion of convection and postglacial rebound observables, *J. Geophys. Res.*, *102*, 2751–2769, 1997.

Mitrovica, J. X., and W. R. Peltier, Constraints on mantle viscosity from relative sea level variations in Hudson Bay, *Geophys. Res. Lett.*, *19*, 1185–1188, 1992.

Mitrovica, J. X., and W. R. Peltier, The inference of mantle viscosity from an inversion of the Fennoscandian relaxation spectrum, *Geophys. J. Int.*, *114*, 45–62, 1993.

Mitrovica, J. X., and W. R. Peltier, Constraints on mantle viscosity based upon the inversion of post-glacial uplift data from the Hudson Bay region, *Geophys. J. Int.*, *122*, 353–377, 1995.

Mitrovica, J. X., C. Beaumont, and G. T. Jarvis, Tilting of continental interiors by the dynamical effects of subduction, *Tectonics*, *8*, 1079–1094, 1989.

Molnar, P., and J. M. Stock, Relative motions of hotspots in the Pacific, Atlantic and Indian Oceans since Late Cretaceous time, *Nature*, *327*, 587–591, 1987.

Morgan, W. J., Hotspot tracks and the opening of the Atlantic and Indian Oceans, in *The Sea*, vol. 7, edited by C. Emiliani, pp. 443–487, Wiley-Interscience, New York, 1981.

Müller, R. D., W. R. Roest, J. Y. Royer, L. M. Gahagan, and J. G. Sclater, A digital map of the ocean floor, *SIO Ref. Ser. 93-30*, Scripps Inst. of Oceanogr., La Jolla, Calif., 1994.

Nakada, M., and K. Lambeck, Glacial rebound and relative sea-level variations: A new appraisal, *Geophys. J. Int.*, *90*, 171–224, 1987.

Nakada, M., and K. Lambeck, Late Pleistocene and Holocene sea-level change in the Australian region and mantle rheology, *Geophys. J. Int.*, *96*, 497–517, 1989.

Navrotsky, A., B. Romanowicz, M. Richards, and D. Weidner, Creating the next generation of reference Earth models, *Eos Trans. AGU*, *76*, 121–122, 1995.

Norton, I. O., Plate motions in the North Pacific: The 43 Ma non-event, *Tectonics*, *14*, 1080–1094, 1995.

O'Connell, R. J., and B. H. Hager, On the thermal state of the Earth, in *Physics of the Earth's Interior*, edited by A. Dziewonski and E. Boschi, pp. 270–317, North Holland, New York, 1980.

O'Connell, R. J., C. W. Gable, and B. H. Hager, Toroidal-poloidal partitioning of lithospheric plate motions, in *Glacial Isostasy, Sea Level and Mantle Rheology*, edited by R. Sabadini and K. Lambeck, pp. 535–551, Kluwer Acad., Norwell, Mass., 1991.

Olson, P., and D. Bercovici, On the equipartition of kinetic energy in plate tectonics, *Geophys. Res. Lett.*, *18*, 1751–1754, 1991.

Patriat, P., and J. Achache, India-Eurasia collision chronology has implications for crustal shortening and driving mechanism of plates, *Nature*, *311*, 615–621, 1984.

Phipps-Morgan, J., and W. H. F. Smith, Flattening of the sea-floor depth-age curve as a response to asthenospheric flow, *Nature*, *359*, 524–527, 1992.

Press, W. H., S. A. Teukolsky, W. T. Vetterling, and B. P. Flannery, *Numerical Recipes*, 2nd edition, Cambridge Univ. Press, New York, 1992.

Ricard, Y., and C. Vigny, Mantle dynamics with induced plate tectonics, *J. Geophys. Res.*, *94*, 17,543–17,560, 1989.

Ricard, Y., L. Fleitout, and C. Froidevaux, Geoid heights and lithospheric stresses for a dynamic Earth, *Ann. Geophys.*, *2*, 267–286, 1984.

Ricard, Y., C. Froidevaux, and L. Fleitout, Global plate motions and the geoid: A physical model, *Geophys. J. Int.*, *93*, 477–484, 1988.

Ricard, Y., C. Doglioni, and R. Sabadini, Differential rotation between lithosphere and mantle: A consequence of lateral mantle viscosity variations, *J. Geophys. Res.*, *96*, 8407–8416, 1991.

Ricard, Y., M. Richards, C. Lithgow-Bertelloni, and Y. Le Stunff, A geodynamical model of mantle density heterogeneity, *J. Geophys. Res.*, *98*, 21,895–21,909, 1993.

Ricard, Y., H. C. Nataf, and J. P. Montagner, The three-dimensional seismological model a priori constrained: confrontation with seismic data, *J. Geophys. Res.*, *101*, 8457–8472, 1996.

Richards, M. A., Hotspots and the case for a high-viscosity lower mantle, in *Glacial Isostasy, Sea Level and Mantle Rheology*, edited by R. Sabadini and K. Lambeck, pp. 571–588, Kluwer Acad., Norwell, Mass., 1991.

Richards, M. A., and D. C. Engebretson, Large-scale mantle convection and the history of subduction, *Nature*, *355*, 437–440, 1992.

Richards, M. A., and R. W. Griffiths, Deflection of plumes by mantle shear flow: Experimental results and a simple theory, *Geophys. J. Int.*, *94*, 367–376, 1988.

Richards, M. A., and B. H. Hager, Geoid anomalies in a dynamic Earth, *J. Geophys. Res.*, *89*, 5987–6002, 1984.

Richards, M. A., and C. Lithgow-Bertelloni, Plate motion changes, the Hawaiian-Emperor bend, and the apparent success of dynamical models, *Earth Planet. Sci. Lett.*, *137*, 19–27, 1996.

Richards, M. A., D. L. Jones, R. A. Duncan, and D. J. DePaolo, A mantle plume initiation model for the Wrangellia flood basalt and other oceanic plateaus, *Science*, *254*, 263–267, 1991.

Richards, M. A., Y. Ricard, C. Lithgow-Bertelloni, G. Spada, and R. Sabadini, Subduction and the long-term stability of Earth's rotation axis, *Science*, *275*, 372–375, 1997.

Richardson, R. M., Ridge forces, absolute plate motions, and the intraplate stress field, *J. Geophys. Res.*, *97*, 11,739–11,748, 1992.

Richardson, R. M., S. C. Solomon, and N. H. Sleep, Tectonic stress in the plates, *Rev. Geophys.*, *17*, 981–1019, 1979.

Royer, J.-Y., R. D. Müller, L. M. Gahagan, L. A. Lawver, C. L. Mayes, D. Nürnberg, and J. G. Sclater, A global isochron chart, *Tech. Rep. 117*, 38 pp., Inst. for Geophys., Univ. of Tex., Austin, 1992.

Russo, R. M., and P. G. Silver, Trench-parallel flow beneath the Nazca plate from seismic anisotropy, *Science*, *263*, 1105–1111, 1994.

Sclater, J. G., B. Parsons, and C. Jaupart, Oceans and continents: Similarities and differences in the mechanisms of heat loss, *J. Geophys. Res.*, *86*, 11,535–11,552, 1981.

Scotese, C. R., Atlas of Phanerozoic plate tectonic reconstructions, *Tech. Rep. 10-90-1*, Paleomap Proj., Dep. of Geol., Univ. of Tex. at Arlington, 1990.

Sleep, N. H., Hotspots and mantle plumes: Some phenomenology, *J. Geophys. Res.*, *95*, 6715–6730, 1990.

Smith, A. G., A. M. Hurley, and J. C. Briden, *Phanerozoic Paleocontinental World Maps*, 102 pp., Cambridge Univ. Press, New York, 1981.

Solheim, L. P., and W. R. Peltier, Mantle phase transitions and layered chaotic convection, *Geophys. Res. Lett.*, *19*, 321–324, 1992.

Solomon, S. C., and N. H. Sleep, Some simple physical models for absolute plate motions, *J. Geophys. Res.*, *79*, 2557–2567, 1974.

Solomon, S. C., N. H. Sleep, and R. M. Richardson, On the forces driving plate tectonics: Inference from absolute plate velocities and intraplate stress, *Geophys. J. R. Astron. Soc.*, *42*, 769–801, 1975.

Stixrude, L., R. J. Hemley, Y. Fei, and H. K. Mao, Thermoelasticity of silicate perovskite and magnesiowüstite and stratification of the Earth's lower mantle, *Science*, *257*, 1099–1101, 1992.

Su, W.-J., and A. M. Dziewonski, Predominance of long wavelength heterogeneity in the mantle, *Nature*, *352*, 121–126, 1991.

Su, W.-J., R. L. Woodward, and A. M. Dziewonski, Degree 12 model of shear velocity heterogeneity in the mantle, *J. Geophys. Res.*, *99*, 6945–6980, 1994.

Tackley, P. J., D. J. Stevenson, G. A. Glatzmaier, and G. Schubert, Effects of an endothermic phase transition at 670 km depth in a spherical model of convection in the Earth's mantle, *Nature*, *361*, 699–704, 1993.

Tackley, P. J., D. J. Stevenson, G. A. Glatzmaier, and G. Schubert, Effects of multiple phase transitions in a three-dimensional spherical model of convection in Earth's mantle, *J. Geophys. Res.*, *99*, 15,877–15,901, 1994.

Takeuchi, H., and Y. Hasegawa, Viscosity distribution within the Earth, *Geophys. J. R. Astron. Soc.*, *9*, 503–508, 1965.

Thoraval, C., P. Machetel, and A. Cazenave, Locally layered convection inferred from dynamic models of the Earth's mantle, *Nature*, *375*, 777–780, 1995.

Turcotte, D. L., and E. R. Oxburgh, Finite amplitude convection cells and continental drift, *J. Fluid Mech.*, *28*, 29–42, 1967.

Tushingham, A. M., and W. R. Peltier, Validation of the ICE-3G model of Würm-Wisconsin deglaciation using a global database of relative sea level histories, *J. Geophys. Res.*, *97*, 3285–3304, 1992.

van der Hilst, R., R. Engdahl, W. Spakman, and G. Nolet, Tomographic imaging of subducted lithosphere below northwest Pacific island arcs, *Nature*, *353*, 37–43, 1991.

van der Hilst, R., S. Widiyantoro, and R. Engdahl, Evidence for deep mantle circulation from global tomography, *Nature*, *386*, 578–584, 1997.

Vigny, C., Y. Ricard, and C. Froidevaux, The driving mechanism of plate tectonics, *Tectonophysics*, *187*, 345-360, 1991.

Ward, S. N., Pacific–North America plate motions: new results from very long baseline interferometry, *J. Geophys. Res.*, *95*, 21,965–21,981, 1990.

Woodward, R. L., A. M. Forte, W. J. Su, and A. M. Dziewonski, Constraints on the large-scale structure of the Earth's mantle, in *Evolution of the Earth and Planets*, *Geophys. Monogr. Ser.*, vol. 74, edited by E. Takahashi, R. Jeanloz, and D. Rubie, pp. 89–109, AGU, Washington, D. C., 1993.

Zhang, S., and U. R. Christensen, Geoid anomalies from Cenozoic subduction in semi-dynamical flow models including a phase boundary, *Geophys. Res. Lett.*, *20*, 2383–2386, 1993.

Zhong, S. J., and M. Gurnis, Mantle convection with plates and mobile, faulted plate margins, *Science*, *267*, 838–843, 1995.

C. Lithgow-Bertelloni, Department of Geological Sciences, University of Michigan, 2534 C. C. Little Building, 425 East University Avenue, Ann Arbor, MI 48209-1063. (e-mail: crlb@umich.edu)

M. A. Richards, Department of Geology and Geophysics, University of California, Berkeley, CA 94720.